論文 / 著書情報
Article / Book Information

題目(和文)	
Title(English)	Search for long-lived gluinos using high-track-multiplicity displaced vertices with the ATLAS detector at $\sqrt{s}$ = 13 TeV
著者(和文)	本橋和貴
Author(English)	Kazuki Motohashi
出典(和文)	学位:博士(理学), 学位授与機関:東京工業大学, 報告番号:甲第10583号, 授与年月日:2017年6月30日, 学位の種別:課程博士, 審査員:陣内 修,柴田 利明,河合 誠之,中村 隆司,久世 正弘
Citation(English)	Degree:Doctor (Science), Conferring organization: Tokyo Institute of Technology, Report number:甲第10583号, Conferred date:2017/6/30, Degree Type:Course doctor, Examiner:Osamu Jinnouchi,Toshi-aki Shibata,Nobuyuki Kawai,Takashi Nakamura,Masahiro Kuze
学位種別(和文)	博士論文
Type(English)	Doctoral Thesis

Ph.D Thesis

Search for long-lived gluinos using high-track-multiplicity displaced vertices with the ATLAS detector at $\sqrt{s} = 13$ TeV

Kazuki Motohashi

Tokyo Institute of Technology,
Department of Physics

Abstract

Many extensions of the Standard Model of particle physics predict the existence of heavy and long-lived particles. A Split-SUSY model often predicts long-lived supersymmetry (SUSY) particles which decay inside the inner tracking volume of the ATLAS detector and they can be reconstructed as displaced vertices (DVs). A Split-SUSY model is one of phenomenologically motivated SUSY models that is consistent with the squark masses of $\mathcal{O}(10 - 1000)$ TeV implied by the observed Higgs mass of 125 GeV. It would also explain the relic density of dark matter when gaugino co-annihilation mechanism is realised. The decay point of the long-lived particle is reconstructed by finding the crossing point of the tracks of charged particles. The charged particles with a large impact parameter cannot be reconstructed efficiently with the ATLAS standard tracking strategy, therefore a special "large radius tracking" criteria were adopted after the chain of standard tracking. The large radius tracking criteria use detector hits which were left after the standard tracking and the requirements on impact parameters and the number of hits of the tracks are relaxed.

A search for direct production of long-lived gluino pairs which transform into R-hadrons in final states with massive DVs with high track-multiplicity and missing transverse momentum has been performed using proton-proton collision data from the 2016 data taking period corresponding to an integrated luminosity of 32.7 fb^{-1} recorded at $\sqrt{s} = 13$ TeV by the ATLAS detector. In order to cover a wide range of parameter space of a Split-SUSY model, a generic DV+$E_{\mathrm{T}}^{\mathrm{miss}}$ channel is investigated in this dissertation. One of the powerful features of the search for new physics via massive and high-track-multiplicity DVs is the extremely low level of background. No SM particles result in the signature and only experimentally induced backgrounds become important. DVs arising from hadronic interaction with detector materials are significantly reduced using a three-dimensional detector material map created with a data-driven method. The number of DVs which were accidentally merged with a neighbour DV and fall into the signal region was found to be negligible. The number of DVs randomly crossed by track is estimated using templates of DV mass distributions constructed by adding a track to a seed vertex and re-calculating its invariant mass.

Not only explicit improvements such as the increase of the LHC beam energy and installation of a new layer of pixel detector into the ATLAS detector but also several improvements and re-optimisations have been made over the analysis of the LHC Run-1. A newly developed event filter purely based on $E_{\mathrm{T}}^{\mathrm{miss}}$ significantly improved the signal acceptances for scenarios with small mass difference between the gluino and neutralino. The filter requirement to find jets which are not associated with tracks from the primary vertex was replaced with a simple calorimeter-based $E_{\mathrm{T}}^{\mathrm{miss}}$ cut. In addition, a method to estimate remaining DVs which were not vetoed by the material map has been developed and criteria for validation of the background estimation methods have been improved to accommodate the R-hadron specific signatures. Two different validation regions were constructed by inverting the material veto requirement, or setting an upper limit on the $E_{\mathrm{T}}^{\mathrm{miss}}$ and the smallest difference of azimuthal angle between selected jets and $E_{\mathrm{T}}^{\mathrm{miss}}$.

No displaced vertices are observed in the signal region, and exclusion limits at 95% confidence level are set for a range of production cross-sections and long-lived-particle lifetimes in a Split-SUSY model, where gluino decays to a pair of quarks and the lightest

neutralino. The excluded limits are set for an interval of proper decay length $c\tau$ = 1–10000 mm. The exclusion limit on gluino mass was set up to 2400 GeV. There is a significant gain compared to the limit in the previous results up to $\sim$ 1600 GeV. In addition, a wide range of parameter space with small mass difference between gluino and neutralino has been excluded up to $\sim$ 1600 GeV. This small mass-splitting scenario had not been investigated in the previous results.

Acknowledgement

At the end of my odyssey as a doctoral course student for three years, I would like to thank many people without whom this dissertation would not have been finished. Since it is hard to mention all the people in a few paragraphs, I would like to thank some of them explicitly here.

First of all, I wish to thank my supervisor, Associate Professor Osamu Jinnouchi, who has been unprecedentedly helpful and gone the extra mile to support me. He did not force me to work following his strategy at all but he allowed me to pursue my own interests. A door of his office is always opened for seamless discussion with students, and his advises and suggestions with prudence paved the vague way in front of me all the time. His brilliance is beyond description and it should be one of the best decisions in my entire life to choose this lab when I was an undergraduate. Connecting the dots looking backwards, the goodness of fit seems to be perfect.

I would like to thank all the members in the displaced vertex search group in the ATLAS SUSY group. Especially, convener of the analysis group, Dr. Jordi Duarte-Campderros, has displayed his exceptional leadership at all times. I also have to mention the fact that he is excellent as not only a physicist but also a programmer. I have learned a lot of things from his beautiful, concise and well-readable analysis codes. Assistant Professor Hidetoshi Otono kindly invited me to this very interesting analysis topic. He had been eager to discuss the analysis with me as a sort of a local supervisor at CERN. Dr. Nora Emilia Pettersson, who was one of the main analysers of Run-1 analysis on the displaced vertex search and was a member of Jinounchi lab before, provided me much of advices and benevolently took her much time for discussion. Dr. Christian Ohm had devoted to construct infrastructure of the analysis as well as guided us along a right way to convergence of analysis. It might not be too much to say that I could not even look at the data properly without his huge effort. Professor Abner Soffer is a man of great insight. His suggestions always make sense and essential for our group. Dr. Lawrence Lee Jr found several flaws in our analysis. He then immediately suggested solutions and fixed them. The analysis results could not have been published without his excellent works. I would like to thank the other members, Dr. Michael Flowerdew, Dominik Krauss, Jennifer Kathryn Roloff as well.

My sub-supervisor, Professor Masahiro Kuze, has constantly provided me profound knowledge regarding a wide range of physics as well as techno pop. If I had got less opportunities to chat with him, my devotion to a social networking service would have diverged to infinity.

I would like to thank extraordinary staffs, Dr. Ryo Nagai, Dr. Minoru Hirose, Dr. Hideyuki Oide and Assistant Professer Hideki Okawa for their kind advices on the analysis. Discussions with Daiki Yamaguchi and Kazuki Todome, who are PhD students at Jinnouchi lab were very helpful. I enjoyed chat and tea time with my office mates in the lab, Hiromi Sawai and Shinichi Sato. The other members in the lab, Hitomi Tokutake, Keisuke Koda, Asawatavonvanich Thanawat, Eunchong Kim and Knut Zoch, made my days in the lab well off.

I also would like to thank friends who had lived in a house with me, located in Ferney-Voltaire near from CERN for two years, Dai Kobayashi, Shota Suzuki, Takuto Kunigo and Atsushi Mizukami. I was helped very much by their great skills at cooking. I enjoyed

spending holidays around CERN with my friends, Takuya Nobe, Yoichi Nonomiya, Shion Chen, Shohei Shirabe, Takuya Honda, Shunsuke Honda, Daiki Hayakawa and other nice guys. I would like to give special thanks to Keralino Sandorovich, who has had enormous influence on me.

Finally, the best thanks my dear parents, Tatsuaki and Yoko for their love and support to me, my sister, Megumi, and brother, Yusuke.

This work was supported by JSPS KAKENHI Grant Number JP15J10809. I could have hot meals and live in a warm house preventing bitter winds thanks to JSPS.

Contents

Chapter 1

Introduction

One of the answers to the fundamental questions of physics such as what kind of substances exist in the universe and what kind of principles describe interaction between them is the Standard Model (SM) of particle physics [1–4]. The SM is a powerful theory that describes strong force, weak force, electromagnetic force based on the gauge principle and can describe almost all of currently known quantum phenomena. The A Toroidal LHC ApparatuS (ATLAS) experiment [5], conducted using the Large Hadron Collider (LHC) [6] of the European Nuclear Research Organisation (CERN), achieved a historical success to discover the Higgs boson which were the last undiscovered particles of SM [7, 8]. With that, it can be said that the SM has been completed. However, it is also a fact that phenomena that SM can not explain, such as dark matter suggested by space observation by e.g. Planck satellites [9, 10] and neutrino oscillation [11], exist. Various theories such as supersymmetry have been proposed as Beyond the Standard Model (BSM), and its verification has been challenged in the ATLAS experiment, however, BSM signs have not been obtained yet.

One of the main ATLAS programs is search for the Supersymmetry (SUSY) [12–20]. The minimal realisation of supersymmetric extension of the Standard Model is called Minimal Supersymetric Standard Model (MSSM). The MSSM could shed light on several open questions which cannot be explained by the SM. Figure 1.1 shows the unexplained issues (big questions) and the proposed theoretical models (big ideas). If the lightest neutralino is the lightest SUSY particle (LSP), it is generally stable and its coupling is of weak interaction, and thus it is a promising candidate of dark matter. Introducing the MSSM, the running coupling constants of the strong and electroweak interactions meet accurately at the grand unification energy scale, $\Lambda_{\mathrm{GUT}} \approx 10^{16}$ GeV [22]. *Naturalness* of a theory requires an additional symmetry in order to naturally explain the observed Higgs mass at the electroweak scale regardless of the huge quantum corrections up to the Planck scale. The SUSY relates fermions and bosons so that the corrections are canceled if the SUSY is realised around TeV scale. If the evidence of supersymmetry is confirmed, it is nothing short of revolutionary.

Nevertheless, the observation of the Higgs boson has significantly changed the prospects for naturalness. The observed Higgs mass of about 125 GeV [23] implies that the mass scale of SUSY particles is much higher than the electroweak scale [24]. This is consistent with the lack of evidence of the SUSY so far in some sense. Rather, a relatively high-scale SUSY has several advantages in phenomenological aspects. The flavour changing neutral current processes and the electric dipole moments of the SM particles are suppressed [25, 26], the proton decay rate is reduced [27] and the gravitino problem

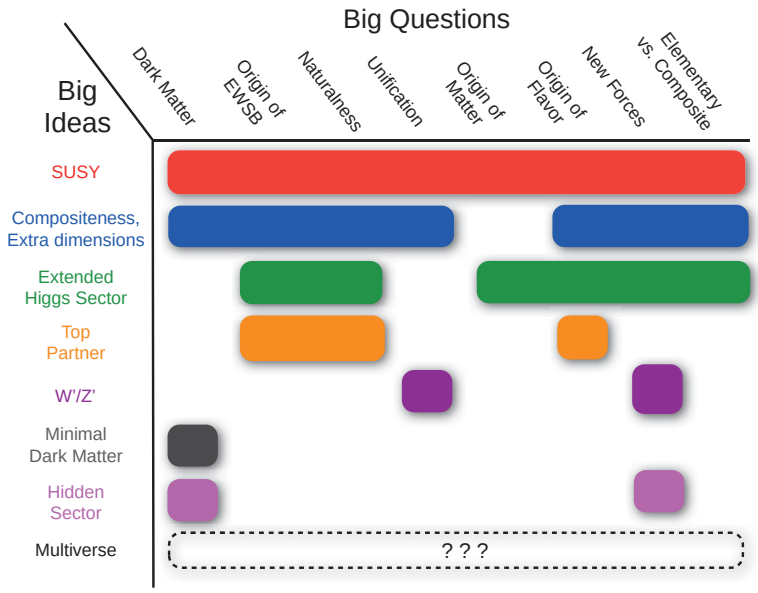

Figure 1.1: Overlap between the questions and ideas discussed in the conference of *Planning the Future of U.S. Particle Physics* (Snowmass 2013) [21].

in cosmology is evaded [28] thanks to the heavy SUSY particles.

A Split-SUSY [24, 29] is one of successful high-scale SUSY models. In Split-SUSY, scalar SUSY particles are heavy at the SUSY breaking scale, while fermions are lighter. Typically the fermion masses are chosen around a TeV scale as expected by the "WIMP miracle" [30] and to realise the gauge coupling unification. Although the mass of scalar SUSY particles had been free parameter before, the 125 GeV Higgs mass has strongly constrained the scalar mass in the range from about 10 TeV to 10^5 TeV [24].

A Split-SUSY model often predicts long-lived gluino, a fermionic superpartner of gluon, which forms R-hadron [31] and decays inside the inner tracking volume of the ATLAS detector and it can be reconstructed as displaced vertices (DVs). A search for direct production of long-lived gluino pairs in final states with massive DVs with high track-multiplicity and missing transverse momentum has been performed using proton-proton collision data from the 2016 data taking period corresponding to an integrated luminosity of 32.7 fb^{-1} recorded at $\sqrt{s} = 13$ TeV by the ATLAS detector at the LHC. Compared to the previous search using the 2012 data at $\sqrt{s} = 8$ TeV [32], the beam energy has been increased by about 60% and it leads to an increase the production cross section of new physics. A newly installed layer of the ATLAS pixel detector has improved the performance of charged particles tracking [33]. Not only the improvement of the apparatuses but also several refinements of the analysis have been performed so that it has gained much higher sensitivity to yet-unexplored signal scenarios.

Outline of the thesis

This thesis begins by considering the motivation for high-scale supersymmetry and to probe it using displaced vertices in Chapter 2. Chapter 3 and 4 introduce the experimental framework: the overview of the ATLAS detector, the object reconstructions and the performances. Chapter 5 is devoted to describe full information of the analysis on

the displaced vertex search with the ATLAS detector using the data taken in 2016. The results are interpreted in supersymmetry and conclusions are given in Chapter 6 and Chapter 7, respectively.

Contributions

Energy frontier experiments have grown in the past several decades and anyone can no longer contribute to every field of the experiment. The LHC-ATLAS experiment is a highly collaborative project in which more than 3,000 researchers have participated. A large number of missions are divided among them. This dissertation also cannot be finished without the many individual works which contribute both directly and indirectly. Major contributions of the author are summarised in the following.

Chapter 3: The ATLAS Experiment

The author contributed to the quality assurance of sensor modules of the new Pixel detector layer (IBL). After installing the IBL into the ATLAS detector, the author was in charge of monitoring data quality (DQ) of the Pixel detector and developing softwares to be used there.

Chapter 4: Object Reconstruction

The author contributed to implementation and validation of secondary vertexing algorithm. Especially, a functionality to merge vertices within a distance of 1 mm and some additional track quality requirements were implemented by the author.

Chapter 5: The Displaced Vertex Analysis

The author has been a main analyser and contributed to essentially every aspect of the displaced vertex analysis toward the Moriond 2017 conference from the beginning to the end of the analysis. The author's analysis results have been approved by the ATLAS collaboration and were shown in public at the international conference. At first, the author estimated the sensitivity of the signal scenarios of interest, produced and validated simulation samples. The author also participated in validation of the large radius tracking and secondary vertexing algorithm using the samples. The author has been responsible for the data-driven background estimation and estimation of the associated uncertainties. The author regularly shared analysis status in the analysis group and got feedback from them.

Chapter 6: Interpretation in Supersymmetry

The author has been responsible for estimation of the signal acceptances and uncertainties except for the tracking-related one. In particular, the author was solely responsible for implementation of a tool for the estimation. The estimated values were used as input for limit setting by collaborators.

Chapter 2

Theoretical Background and Motivation for Displaced Vertex Search

The SUSY is one of the most attractive extensions of the SM. SUSY could shed light on several problems which cannot be explained by the SM. It provides a dark matter candidate, and might be able to play essential role for the unification of the coupling of the fundamental forces. An introduction to the MSSM shall be given in this chapter. A particular attention is paid for consistency with the observed Higgs mass and dark matter relic abundance.

2.1 Introduction to the Standard Model

The SM of particle physics [1–4] is a quantum field theory which explains the interactions between elementary particles with great accuracy. The SM was established in 1970s and is composed of a unified theory of electromagnetic and weak forces, which is called Glashow-Weinberg-Salam theory, and Quantum Chromodynamics (QCD), which describes strong force. These theories are described with renormalisable gauge fields and based on the following symmetry

$$SU(3)_C \otimes SU(2)_L \otimes U(1)_Y \tag{2.1}$$

where C, L and Y are the colour charge, the weak isospin and the hypercharge, respectively. The dynamics of the quantum state and the fundamental fields of the SM can be described by the Lagrangian $\mathcal{L}_{\mathrm{SM}}$:

$$\mathcal{L}_{\mathrm{SM}} = -\frac{1}{4}F_{\mu\nu}F^{\mu\nu} + i\bar{\psi}\not{D}\psi + \psi_i y_{ij}\psi_j\phi + h.c. + |D_\mu\phi|^2 - V(\phi), \tag{2.2}$$

where F and D are the strength tensors of the gauge fields (photon, W, Z, gluon), terms with a ψ include fermions (quarks and leptons), and terms with a ϕ include the Higgs boson. y_{ij} denotes a matrix of Yukawa couplings, and $V(\phi)$ represents the Higgs potential. Each term defines the behaviour of the elementary particles and it can be calculated following the Feynmann rules. The fundamental forces are propagated by exchange of virtual particles (gauge bosons) carrying energies and momenta. The properties of the particles of the SM shall be explained in the next section.

2.1.1 Elementary particles and forces

Elementary particles in the framework of the SM include the fermions (quarks and leptons), which are spin-1/2 particles and generally called "matter particles", as well as the bosons (gauge bosons and the Higgs boson), which are often called "force particles". The spins of gauge bosons are 1, while the Higgs boson is a spin-0 scalar particle. The fermions have two eigenstates of left and right chirarities. The left-handed fermions form $SU(2)_L$ doublets under weak interaction and the right-handed fermions form singlets. The neutrinos are assumed to be massless, so that only left-handed neutrinos are considered. The matter sector of the SM can be summarised as follows.

$$\begin{array}{cccccc} \begin{pmatrix} u_L \\ d_L \end{pmatrix} & \begin{pmatrix} c_L \\ s_L \end{pmatrix} & \begin{pmatrix} t_L \\ b_L \end{pmatrix} & \begin{pmatrix} \nu_{eL} \\ e_L \end{pmatrix} & \begin{pmatrix} \nu_{\mu L} \\ \mu_L \end{pmatrix} & \begin{pmatrix} \nu_{\tau L} \\ \tau_L \end{pmatrix} \\ u_R,\, d_R & c_R,\, s_R & t_R,\, b_R & e_R & \mu_R & \tau_R \end{array}$$

The massless gauge bosons W^i; $i = 1, 2, 3$ and B are the mediators of the electroweak interaction and the gluon g is the carrier of the strong force. Although the gauge symmetry forbids mass terms of any particles, the electroweak gauge bosons acquire masses after spontaneous symmetry breaking of the $SU(2)$ electroweak symmetry. The mass eigenstates ($W^{\pm}$, Z, and γ) are written as:

$$W^{\pm} = \frac{1}{\sqrt{2}}(W^1 \mp W^2) \tag{2.3}$$

$$\begin{pmatrix} Z \\ \gamma \end{pmatrix} = \begin{pmatrix} \cos\theta_W & -\sin\theta_W \\ \sin\theta_W & \cos\theta_W \end{pmatrix} \begin{pmatrix} W^3 \\ B \end{pmatrix}, \tag{2.4}$$

where the Weinberg angle θ_W is defined by:

$$\sin\theta_W = \frac{e}{g_2}, \tag{2.5}$$

where e and g_2 are the electric charge and the $SU(2)$ gauge coupling constant. The masses of quarks and leptons (m_f) are given by:

$$m_f = \frac{v\lambda_f}{\sqrt{2}}, \tag{2.6}$$

where v is the vacuum expectation value of the Higgs field and λ_f is the Yukawa coupling, respectively.

On 4th of July 2012, a new boson with the mass of $\sim$ 126 GeV was observed by ATLAS and CMS Collaborations simultaneously [7, 8]. The property of the boson was measured further and found to be consistent with the Higgs boson in 2013. The observation of the Higgs boson verifies the mechanism that spontaneously breaks the electroweak symmetry and gives masses to particles. The measured value of the Higgs mass is $125.5 \pm 0.2\,(\text{stat.})\,^{+0.5}_{-0.6}\,(\text{syst.})$ GeV [23]. The particles of the SM and their properties are summarised in Fig. 2.1.

2.1.2 Limitations of the Standard Model

The SM has extraordinarily accurate predictive power of phenomena of high energy physics experiments as shown in Fig. 2.2. No significant deviation from theoretical calculation has been observed over a vastly wide range of energy scale. However, the SM

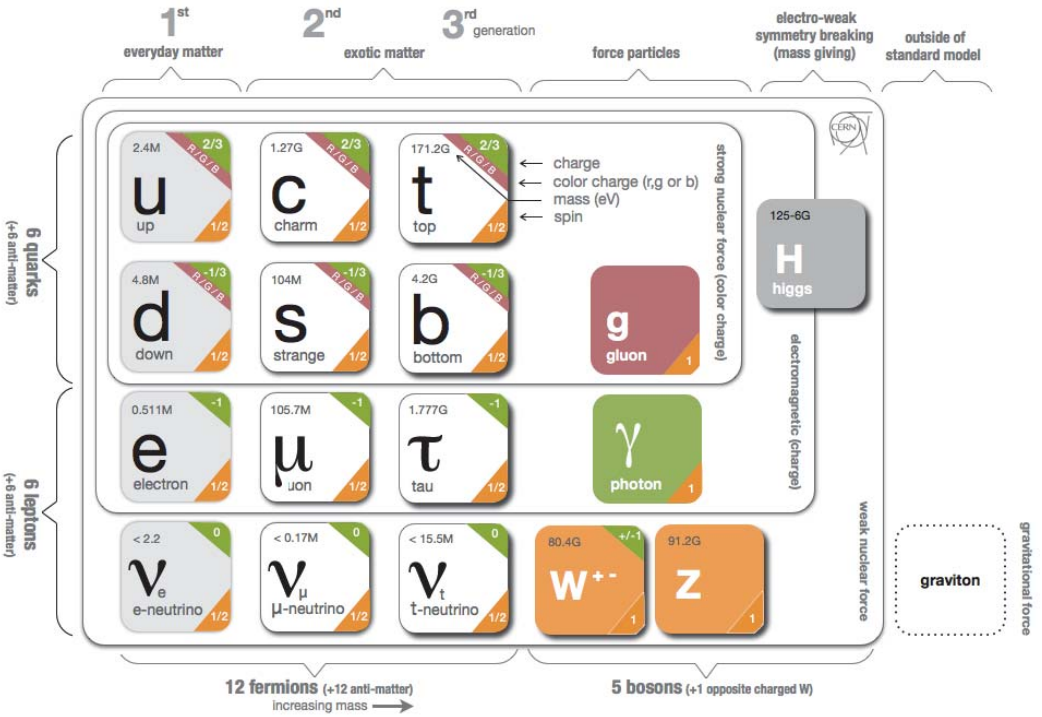

Figure 2.1: An overview of the properties of the particles in the Standard Model [34].

cannot answer a few open questions. For instance, the fourth fundamental force, gravity, is not formulised at all and neutrinos are assumed as massless particles although the neutrino oscillation has been thoroughly confirmed which is a clear evidence of non-zero neutrino mass.

Within the SM, the bare mass parameter of the Higgs is corrected by large quantum loop corrections which are proportional to the cut off scale (Planck scale),

$$\delta m_H^2 \propto \frac{\lambda_f^2 N_c^f}{8\pi^2}\Lambda^2, \tag{2.7}$$

where λ_f and N_c^f are the Yukawa coupling and the number of colours of fermion f. These corrections are about 16 digits larger than the observed mass of the Higgs around the electromagnetic scale. Without any additional mechanisms, it is necessary to cancel out the 16 digits of contributions from the bare mass and the corrections to obtain the observed Higgs mass. This huge magnitude of cancelation is regarded as unnatural and often called *fine-tuning*. It is expected that there is an additional symmetry or mechanism to avoid the fine-tuning from the point of view of *naturalness* of a theory.

The SM contains no candidate particle for dark matter which comprises approximately 27% of the energy of the whole universe. The neutrino is a stable, neutral and weakly interacting particle, however the amount of neutrinos in the universe is not enough to explain the observed relic density of dark matter. Also the nature of dark energy which accounts for approximately 68% of the total energy in observable universe is

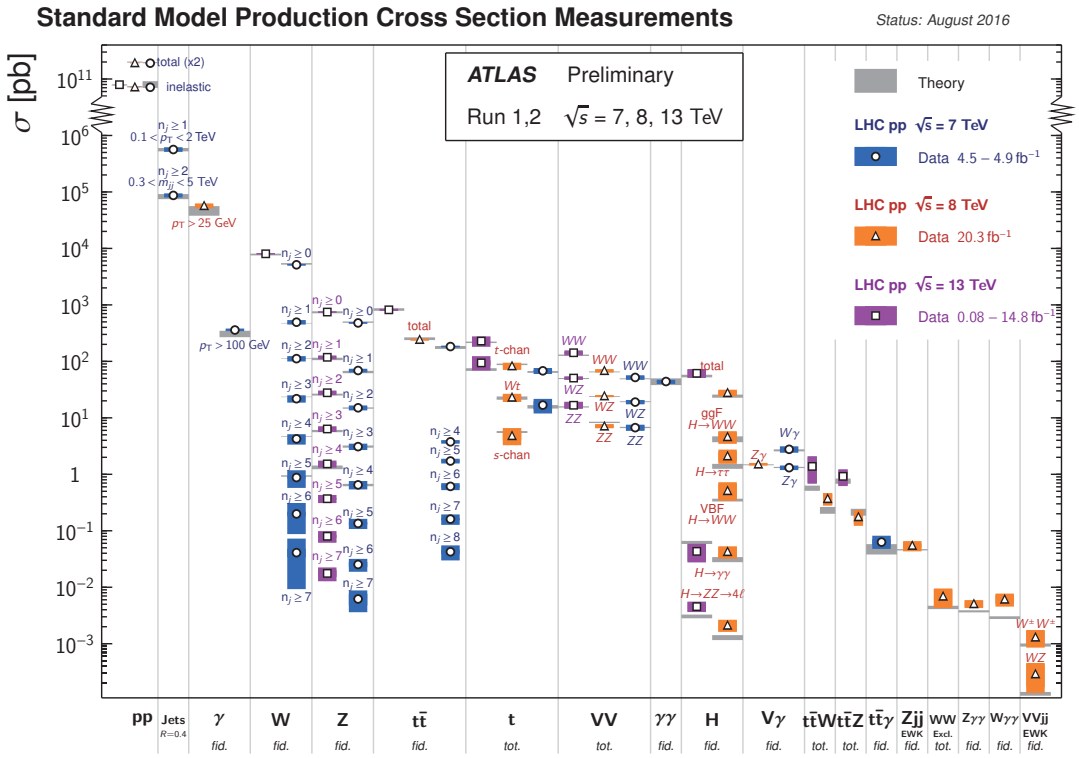

Figure 2.2: Summary of several Standard Model total and fiducial production cross section measurements, corrected for leptonic branching fractions, compared to the corresponding theoretical expectations [35]. All theoretical expectations were calculated at NLO or higher.

entirely unknown in the framework of the SM. As a result, the mass of ordinary baryonic matter contributes only about 5% of the universe.

2.2 Introduction to Supersymmetry (SUSY)

A number of extensions of the SM have been proposed in order to solve these questions. One of the well-motivated solutions is adding extra dimensions to the observed 3+1 space-time dimensions. This makes the effective Planck scale smaller, in a certain model, to an order of scale of extra dimension. As a result, the hierarchy between the electromagnetic scale and the Planck scale would be significantly reduced.

Another attractive theory beyond the SM is SUSY [12–20]. The SUSY is based on a generalisation of space-time transformation which relates fermions and bosons. The operator Q performs this type of transformations with[1]

$$Q\,|\text{Fermion}\rangle = |\text{Boson}\rangle\,, \qquad Q\,|\text{Boson}\rangle = |\text{Fermion}\rangle\,. \tag{2.8}$$

Because the angular momentum must be invariant in both sides of each equation in Eq. (2.8)[2], the Q is a fermionic operator that carries spin angular momentum 1/2. Haag-

[1] This section follows the convention adopted in Ref. [36].
[2] A fermion is a particle with the spin of an odd half integer, while a boson has the integral spin.

Table 2.1: Fields in the MSSM and the $SU(3) \otimes SU(2) \otimes U(1)$ quantum numbers.

Names		SUSY field	SM partner	Quantum numbers		
				$SU(3)$	$SU(2)$	$U(1)$
squarks, quarks	Q	$(\tilde{u}_L,\ \tilde{d}_L)$	$(u_L,\ d_L)$	8	1	$\frac{1}{6}$
($\times$3 families)	$\bar{u}$	$\tilde{u}_R^*$	$u_R^\dagger$	3	1	$-\frac{2}{3}$
	$\bar{d}$	$\tilde{d}_R^*$	$d_R^\dagger$	3	1	$\frac{1}{3}$
sleptons, leptons	L	$(\tilde{\nu},\ \tilde{e}_L)$	$(\nu,\ e_L)$	1	2	$-\frac{1}{2}$
($\times$3 families)	$\bar{e}$	$\tilde{e}_R^*$	$e_R^\dagger$	1	1	1
Higgs, higgsinos	H_u	$(\tilde{H}_u^+,\ \tilde{H}_u^0)$	$(H_u^+,\ H_u^0)$	1	2	$\frac{1}{2}$
	H_d	$(\tilde{H}_d^0,\ \tilde{H}_d^-)$	$(H_d^0,\ H_d^-)$	1	2	$-\frac{1}{2}$
gluino, gluon		$\tilde{g}$	g	8	1	0
winos, W bosons		$\widetilde{W}^\pm\ \widetilde{W}^0$	$W^\pm\ W^0$	1	3	0
bino, B boson		$\tilde{B}^0$	B^0	1	1	0

Lopuszanski-Sohnius theorem [37] highly constrains a form of the supersymmetry algebra which is consistent with the 4-dimensional quantum field theory. The operators Q and its hermitian conjugate, $Q^\dagger$, satisfy the following schematic anti-commutation and commutation relations:

$$\{Q, Q^\dagger\} = P^\mu, \tag{2.9}$$

$$\{Q, Q\} = \{Q^\dagger, Q^\dagger\} = 0, \tag{2.10}$$

$$[P^\mu, Q] = [P^\mu, Q^\dagger] = 0, \tag{2.11}$$

where P^μ is the four-momentum generator of spacetime translations. It can be shown that the Q operator also commutes with $m^2 = P_\mu P^\mu$ using Eq. (2.11), i.e., the supersymmetric transformation does not change the mass of a particle. This can be interpreted that the supersymmetric partner would have the same mass as its counterpart in the SM.

SUSY is an appealing theory that enables the unification of the gauge coupling constants of strong, weak and electromagnetic interactions around a scale of the Grand Unified Theory (GUT) around 10^{15-16} GeV. SUSY is also expected to combine the GUT with the gravity since Einstein's theory of general relativity is automatically derived by imposing SUSY as a local symmetry in supersymmetric quantum field theory.

2.2.1 The Minimal Supersymmetric Standard Model (MSSM)

Although there are varieties of supersymmetric extensions to the SM, the simplest one, MSSM, is used as a representative model throughout this dissertation. A brief overview of the MSSM is given in this section focusing on its phenomenology. More details can be found, for instance, in Reference [36].

The MSSM introduces a super-partner for every particle of the SM with the same quantum numbers and properties but with 1/2 spin difference as listed in Tab. 2.1. In order to be consistent with the fact that the baryon number and lepton number

conservations have been tested precisely, a new symmetry called "R-parity" [38] is added to the MSSM. R-parity, which is assumed to be conserved, is defined as:

$$R = (-1)^{3(B-L)+2S}, \tag{2.12}$$

where B and L are the baryon and lepton numbers, respectively and S is the spin. It is easy to check that all SM particles have R-parity of $+1$, while SUSY particles (sparticles) have R-parity of -1. In consequence of the R-parity conservation:

1. sparticles are produced in pairs,
2. decay products of sparticles include other sparticles,
3. the Lightest SUSY Particle (LSP) is stable.

This third outcome implies that the LSP is a possible candidate of the dark matter of the universe.

There is one complex Higgs doublet in the SM, however a single higgsino (the fermionic superpartner of the Higgs boson) would induce gauge anomaly, which is required to be cancelled by renomalizability of the theory. The gauge anomaly occurs in general if

$$\sum_{\text{fermions}} Y \neq 0, \tag{2.13}$$

where Y is the hypercharge. Therefore, MSSM contains two chiral super-multiplets with two complex Higgs doubles H_u and H_d, which couple with up-type and down-type super-multilets, respectively, and their fermionic super-partners, higgsinos.

2.2.2 Supersymmetry breaking

Since any sparticles have not been observed so far, even if SUSY is realised, it must be a broken symmetry. SUSY breaking terms of the Lagrangian should be *soft* in order to avoid ultraviolet divergences appearing in scalar masses. This means that the effective Lagrangian of the MSSM can be split into two components:

$$\mathcal{L}_{\text{MSSM}} = \mathcal{L}_{\text{SUSY}} + \mathcal{L}_{\text{Soft}}, \tag{2.14}$$

where $\mathcal{L}_{\text{SUSY}}$ contains the interaction terms and preserves supersymmetric invariance, and $\mathcal{L}_{\text{Soft}}$ is the SUSY breaking terms which are composed of only mass terms and coupling parameters with positive mass dimension less than four.

The general form of soft SUSY breaking terms in the Lagrangian $\mathcal{L}_{\text{Soft}}$ can be written as:

$$\begin{aligned}\mathcal{L}_{\text{Soft}} = &-\left(\frac{1}{2}M_a\lambda^a\lambda^a + \frac{1}{3!}\mathcal{A}^{ijk}\phi_i\phi_j\phi_k + \frac{1}{2}\mathcal{B}^{ij}\phi_i\phi_j + \mathcal{C}^i\phi_i\right) + h.c. \\ &- (m^2)^i_j\phi^{j*}\phi_i,\end{aligned} \tag{2.15}$$

where ϕ_i is the scalar component of one of the MSSM superfields, with m being interpreted as its mass, and λ^a the gaugino fields, with M their Majorana mass term. $\mathcal{A}$, $\mathcal{B}$ and $\mathcal{C}$ are the trilinear, bilinear and linear scalar interaction terms. The soft SUSY breaking terms of the MSSM can be specified as:

$$\begin{aligned}\mathcal{L}^{\text{MSSM}}_{\text{Soft}} = &-\frac{1}{2}\left(M_3\tilde{g}\tilde{g} + M_2\tilde{W}\tilde{W} + M_1\tilde{B}\tilde{B} + \text{h.c.}\right) \\ &-\left(\tilde{\bar{u}}\mathcal{A}_{\mathbf{u}}\tilde{Q}H_u - \tilde{\bar{d}}\mathcal{A}_{\mathbf{d}}\tilde{Q}H_d - \tilde{\bar{e}}\mathcal{A}_{\mathbf{e}}\tilde{L}H_d + \text{h.c.}\right) \\ &-\tilde{Q}^\dagger\mathbf{m}^{\mathbf{2}}_{\mathbf{Q}}\tilde{Q} - \tilde{L}^\dagger\mathbf{m}^{\mathbf{2}}_{\mathbf{L}}\tilde{L} - \tilde{\bar{u}}\mathbf{m}^{\mathbf{2}}_{\bar{\mathbf{u}}}\tilde{\bar{u}}^\dagger - \tilde{\bar{d}}\mathbf{m}^{\mathbf{2}}_{\bar{\mathbf{d}}}\tilde{\bar{d}}^\dagger - \tilde{\bar{e}}\mathbf{m}^{\mathbf{2}}_{\bar{\mathbf{e}}}\tilde{\bar{e}}^\dagger \\ &- m^2_{H_u}H^*_uH_u - m^2_{H_d}H^*_dH_d - (\mu H_uH_d + \text{h.c.}),\end{aligned} \tag{2.16}$$

where M_3, M_2, M_1 are the gluino, wino and bino mass terms. Each of $\mathcal{A}_\mathbf{u}$, $\mathcal{A}_\mathbf{d}$, $\mathcal{A}_\mathbf{e}$, is a complex 3×3 matrix in family space, with dimensions of [mass], in one-to-one correspondence with the Yukawa couplings. Each of $\mathbf{m}^\mathbf{2}_\mathbf{Q}$, $\mathbf{m}^\mathbf{2}_\mathbf{\bar{u}}$, $\mathbf{m}^\mathbf{2}_\mathbf{\bar{d}}$, $\mathbf{m}^\mathbf{2}_\mathbf{L}$, $\mathbf{m}^\mathbf{2}_\mathbf{\bar{e}}$ is a squark or slepton mass term described as a 3×3 matrix in family space. m_{H_u}, m_{H_u} and μ are mass terms which contributes to the Higgs potential. Without additional assumptions, the MSSM contains 124 independent parameters which would be determined by experiments. The several parameters which are directly relevant to the following discussions are summarised below:

- M_a $(a = 1, 2, 3)$: the soft SUSY breaking parameters of gaugino masses.
- $\tan\beta$: the ratio of the vacuum expectation values of the two Higgs potentials:

$$\tan\beta = \frac{v_u}{v_d}. \tag{2.17}$$

- $\mathbf{m}^\mathbf{2}_\mathbf{Q}$, $\mathbf{m}^\mathbf{2}_\mathbf{\bar{u}}$, $\mathbf{m}^\mathbf{2}_\mathbf{\bar{d}}$, $\mathbf{m}^\mathbf{2}_\mathbf{L}$, $\mathbf{m}^\mathbf{2}_\mathbf{\bar{e}}$: the squark (and slepton mass) matrices. $\mathbf{m}^\mathbf{2}_\mathbf{Q}$ is for the left handed squarks, ($\mathbf{m}^\mathbf{2}_\mathbf{L}$ is for the left handed sleptons) and $\mathbf{m}^\mathbf{2}_\mathbf{\bar{u}}$ and $\mathbf{m}^\mathbf{2}_\mathbf{\bar{d}}$ are for the right handed ones ($\mathbf{m}^\mathbf{2}_\mathbf{\bar{e}}$ is for sleptons).

The neutral gauginos and higgsinos mix into four mass eigenstates called neutralinos $\tilde{\chi}^0_i$ $(i = 1, 2, 3, 4)$ because their quantum numbers are the same. The indices in i are ordered in mass, i.e., $\tilde{\chi}^0_1$ is the LSP that is assumed to be stable in this dissertation. A 4×4 symmetric complex mass matrix describes the mixing at tree level as:

$$\mathcal{M}_{\tilde{\chi}^0} = \begin{pmatrix} M_1 & 0 & M_W \tan\theta_W \cos\beta & -M_W \tan\beta \sin\beta \\ & M_2 & M_W \cos\beta & M_W \sin\beta \\ & & 0 & -\mu \\ & & & 0 \end{pmatrix}, \tag{2.18}$$

where θ_W is the Weignberg angle.

2.2.3 SUSY after the Higgs Discovery

Although the energy scale of SUSY is sometimes expected to be located around TeV-scale from the view point of *naturalness*, the lack of evidence for SUSY at the LHC and the observed SM-Higgs boson with the mass of about 125 GeV implies that the masses of squarks might be much heavier than the electroweak scale (Fig. 2.3). Split SUSY [24,29], motivated by the phenomenology rather than *naturalness*, is one of the theories which match this situation. Split SUSY assumes the masses of SUSY partners of gauge bosons (gaugino) around $O(1)$ TeV in order to make the LSP a candidate of the dark matter as later shown in Section 2.3 and realise unification of the gauge coupling constants, while those of the other particles are expected to be at a much higher scale. At the expense of *naturalness*, a high SUSY breaking scale could overcome several disadvantages of the phenomenology of the weak-scale SUSY models, such as difficulties to explain the absence of the flavour changing neutral current (FCNC), the electric dipole moments (EDMs) of the SM particles and the small decay rate of the proton.

Within a typical parameter space of Split SUSY, a supersymmetric partner of gluon (gluino) becomes long-lived due to the heavy mass of squarks which is an intermediate state of the decay chain of a gluino. If the mean lifetime of a gluino is longer than the hadronization time scale ($\approx (200\,\mathrm{MeV})^{-1}$), a gluino transforms into a hadronic state,

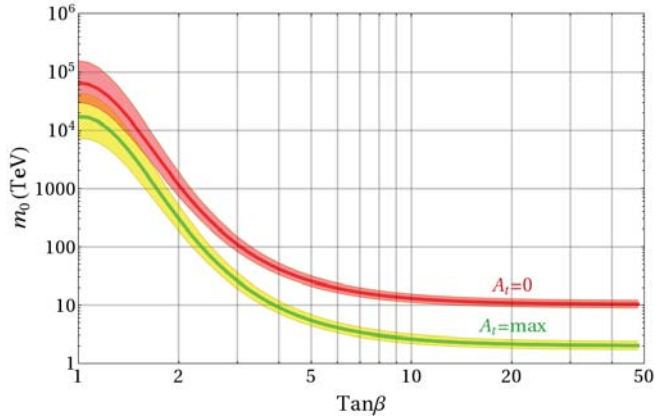

Figure 2.3: The scalar mass scale in Split Supersymmetry as a function of $\tan\beta$ for a Higgs mass fixed at 125.5 GeV for no and maximal stop mixing [24]. The 1σ error bands coming from the top mass measurement (which dominate over other uncertainties) are also shown.

R-hadron [31], as analogous to the ordinary hadrons. If the lifetime of a gluino is an order of ns, it often decays in the volume of the inner tracker of the ATLAS detector and it could be reconstructed as a displaced vertex (DV). Typically, a gluino decays to LSP via a virtual squark with emitting a pair of quark and anti-quark ($\tilde{g} \to \bar{q}\tilde{q} \to \bar{q}q\tilde{\chi}_1^0$). The quarks would make hadronic showers resulting in higher charged-particle multiplicity associated to the DV as the mass difference between gluino and the LSP becomes large. The invariant mass of a DV calculated by the momenta of associated charged particles would be large as well. Searching gluinos with this signature has a huge advantage in terms of signal to background ratio since no SM particle creates such a DV with high charged-particle multiplicity and the large invariant mass. In addition, it is difficult to be covered by the typical strategy of the SUSY search in the ATLAS experiment, which requires the large missing transverse energy and multiple hard objects, such as jets or leptons, pointing to a primary vertex.

2.3 Dark Matter Relic Density

The evidences of dark matter are confirmed by a number of experimental observations, for instance, galactic rotation curves [39], the weak gravitational lensing [40] and the Bullet Cluster [41], that consists of two colliding clusters of galaxies, officially named 1E 0657-558. The Lambda Cold Dark Matter (ΛCDM) model is often referred to as the standard model of Big Bang cosmology, where Λ denotes a cosmological constant related to dark energy and dark matter is assumed as *cold*, i.e., non-relativistic.

In the ΛCDM model, a sizeable amount of dark matter is generally expected to be produced in the very early universe. When the temperature was much higher than m_χ (the mass of dark matter), the cross sections of $\chi\bar{\chi}$ creation and annihilation ($\chi\bar{\chi} \rightleftarrows Y\bar{Y}$, where Y denotes a SM particle) were equally balanced. However, as the temperature of the universe decreases below m_χ, the $\chi\bar{\chi}$ creation process was exponentially suppressed, while the annihilation rate was not changed significantly in thermal equilibrium. A mechanism to restrain the annihilation process is necessary, otherwise dark matter disappeared quickly, and then the dark matter relic density becomes inconsistent to the

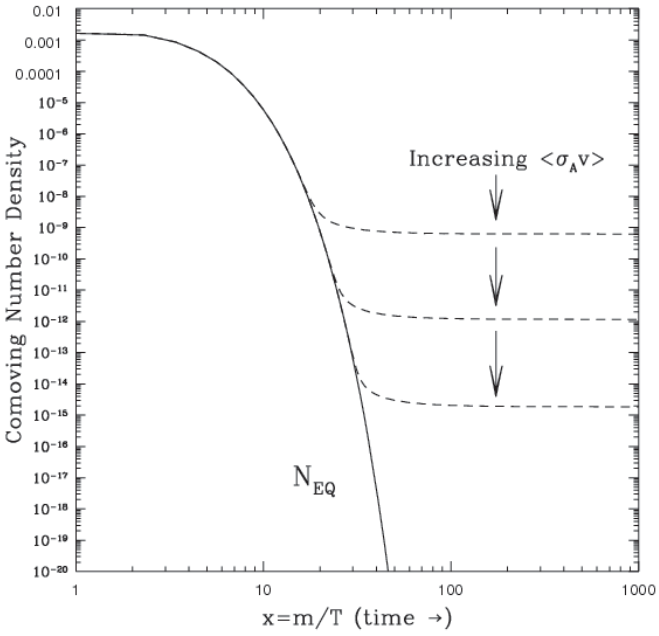

Figure 2.4: A schematic of the comoving number density of a stable species as it evolves through the process of thermal freeze-out [42].

observed value. A possible mechanism is dilution of dark matters due to Hubble expansion. The Boltzmann equation Eq. (2.19) describes the competing effects of Hubble expansion and annihilation:

$$\frac{\mathrm{d}n_\chi}{\mathrm{d}t} + 3Hn_\chi = -\langle\sigma_{\chi\bar{\chi}}v\rangle(n_\chi^2 - n_{\chi,\,\mathrm{eq}}^2), \tag{2.19}$$

where n_χ is the number density of dark matters, H is the Hubble parameter which represents the expansion rate of the universe, $\langle\sigma_{\chi\bar{\chi}}v\rangle$ is the thermally averaged $\chi\bar{\chi}$ annihilation cross section multiplied by their relative velocity, and $n_{\chi,\,\mathrm{eq}}^2$ is the equilibrium value of n_χ at very high temperatures ($T \gg m_\chi$). Fig. 2.4 schematically shows how the number of density of dark matters goes as the temperature of the universe drops. In the limit of $T \ll m_\chi$, the number of density of dark matters reaches a fixed value. This condition is often referred to as thermal freeze-out.

By solving Eq. (2.19) as shown in Reference [30], the resulting relic density of dark matters is given approximately as:

$$\Omega_\chi h^2 \approx \frac{1.04 \times 10^9\,\mathrm{GeV}^{-1}}{M_{\mathrm{Pl}}} \cdot \frac{m_\chi}{T_{\mathrm{FO}}\sqrt{g_*}} \cdot \frac{1}{a + 3bT_{\mathrm{FO}}/m_\chi}, \tag{2.20}$$

where Ω_χ is the present-day density parameter of dark matter, $h \equiv H/100\,\mathrm{km\ s^{-1}\ Mpc^{-1}}$ is the reduced Hubble constant, M_{Pl} is the Planck mass, T_{FO} is the temperature at which freeze-out occurs, g_* is the number of external degrees of freedom, a and b are terms in the non-relativistic expansion, $\langle\sigma_{\chi\bar{\chi}}v\rangle = a + b\langle v^2\rangle + \mathcal{O}(v^4)$. Eq. (2.20) is simplified to Eq. (2.21), which is accurate within an order of magnitude:

$$\Omega_\chi h^2 \approx 0.1 \times \frac{3 \times 10^{-26}\,\mathrm{cm^3 s^{-1}}}{\langle\sigma v\rangle}. \tag{2.21}$$

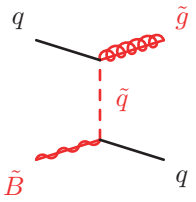

Figure 2.5: Feynman diagram of transition of bino ($\tilde{B}$) into gluino ($\tilde{g}$) via quark scattering.

The measured value of the relic density of cold dark matter by Planck Collaboration [9] using data taken in 2015 is $\Omega_{\mathrm{CDM}}h^2 = 0.1198 \pm 0.0015$ [10]. Given the observed relic density and Eq. (2.21), the product of the annihilation cross section and the relative velocity is required to be an order of $3 \times 10^{-26}\,\mathrm{cm^3 s^{-1}}$. This is similar to the value for a Weakly Interacting Massive Particle (WIMP) with the mass of $\mathcal{O}$(100-1000) GeV [30]. Again, the MSSM predicts a particle with these properties (LSP) by an independent assumption. The coincidence is often referred to as "WIMP miracle".

2.3.1 Gaugino Co-annihilation

If the bosonic SUSY partners are much heavier than the fermionic SUSY partners as expected by Split SUSY model, candidates for dark matter in the Universe are the neutral bino, wino and Higgsino. In case that the supersymmetry is broken by the anomaly mediation mechanism, the neutral wino naturally becomes the LSP. The thermal relic abundance of the wino with the mass of around 3 TeV can explain the observed dark matter density. Higgsino with the mass of around 1 TeV can also explain the observed dark matter density although the cross section of direct production of these particles is quite small so that they are actually far beyond the reach of the LHC.

The last candidate is bino dark matter. It is known that the bino dark matter usually suffers from over-production since the interaction between the bino and the SM particles is suppressed in general. The gaugino co-annihilation mechanism can significantly improves this situation [43, 44]. The co-annihilation between bino and gluino is focused throughout this paper although bino-wino, and bino-wino-gluino co-annihilation are possible as well.

Bino-gluino co-annihilation

In order to be consistent with the observed relic density $\Omega_{\mathrm{DM}}h^2 \simeq 0.12$, the masses of bino and gluino ($M_{\tilde{B}}$ and $M_{\tilde{g}}$, respectively) should be degenerated, i.e., $\Delta M \equiv M_{\tilde{g}} - M_{\tilde{B}} \lesssim 100$ GeV [43]. If the bino-gluino co-annihilation is realised, it is also required that the chemical equilibrium between them, schematically $\tilde{B}\tilde{B} \leftrightarrows \tilde{g}\tilde{g}$, had been maintained during freeze-out epoch in the very early universe, when the temperature was much higher than the dark matter mass. In other words, the transition rate of bino into gluino via quark scattering, $\Gamma(\tilde{B}q \to \tilde{g}q)$ (see Fig. 2.5), should be enough faster than the Hubble expansion rate. This condition gives an upper bound on the mass scale of squarks ($\tilde{m}$) [44]:

$$\tilde{m} \lesssim 250 \times \left(\frac{M_{\tilde{B}}}{1\,\mathrm{TeV}}\right)^{\frac{3}{4}}\ \mathrm{TeV}. \tag{2.22}$$

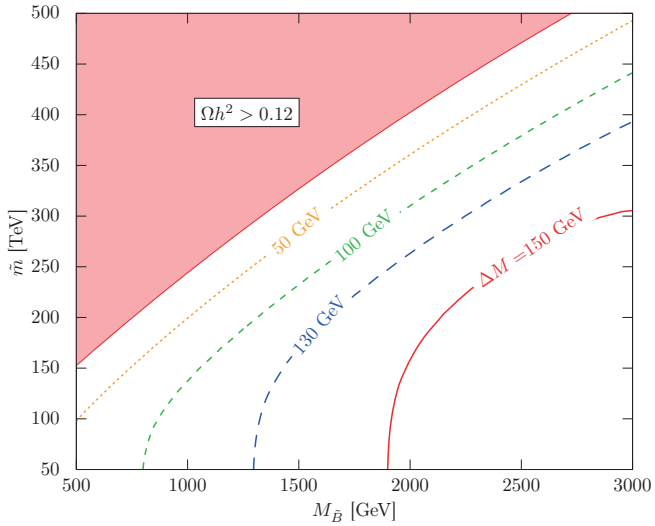

Figure 2.6: Contour for the mass difference ΔM which makes the thermal relic abundance of bino DM equal to the observed DM density $\Omega_{\rm DM}h^2 = 0.12$ [44]. In the red shaded region the bino DM is overproduced due to failure of bino-gluino co-annihilation, numerically given in Eq. (2.22).

The rate of bino-gluino co-annihilation increases as the mass difference between bino and gluino becomes smaller or the mass of squark, which mediates the transition of bino into gluino, becomes lighter. The mass differences ΔM with which the thermal relic abundance of bino explains the observed relic dark matter density $\Omega_{\rm DM}h^2 = 0.12$ are shown in Fig. 2.6. The parameter space forbidden by Eq. (2.22) is indicated as a red shaded region.

In this scenario, the mass of gluino is assumed to be $\mathcal{O}(1)$ TeV, the LHC might produce it. If it is the case, as discussed in Section 2.2.1, gluinos are produced in pair, and then a gluino decays into a quark, an anti-quark and a bino via exchange of virtual squark. The decay length of gluino follows Eq. (2.23) [44]:

$$c\tau_{\tilde{g}} = \mathcal{O}(1) \times \left(\frac{\Delta M}{100\,\text{GeV}}\right)^{-5} \left(\frac{\tilde{m}}{100\,\text{TeV}}\right)^{4} \text{cm}. \tag{2.23}$$

Figure 2.7 shows the relation between the gluino decay length and the mass difference between bino and gluino with the fixed mass of squark ($\tilde{m}$) at 100 GeV. The black solid line represents the parameters that explain the observed dark matter density. It is shown that a gluino typically has a decay length of $c\tau_{\tilde{g}} > \mathcal{O}(1)$ mm in this scenario. Such gluino forms R-hadron and leaves a displaced vertex in a detector as discussed in Section 2.2.3. A displaced vertex originated from a massive coloured particle is often associated with a number of tracks and its invariant mass becomes larger than SM particles. This fact can be used to probe this scenario in the ATLAS experiment. Further details on an analysis on search for massive displaced vertex will be given in Chapter 5.

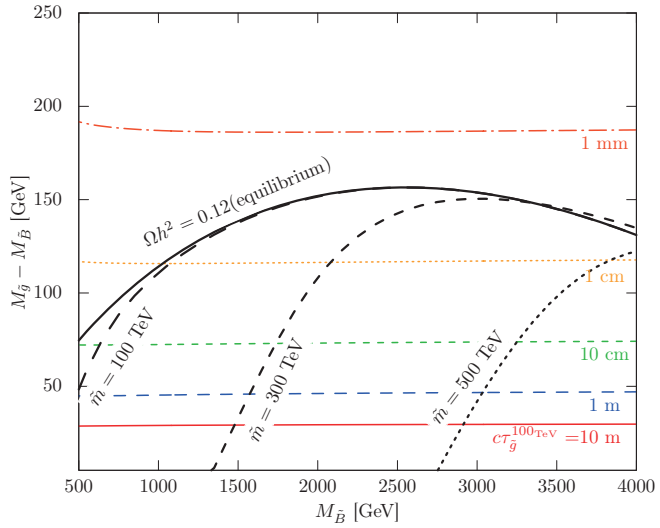

Figure 2.7: Decay length of the gluino $c\tau_{\tilde{g}}^{100\,\mathrm{TeV}}$ with the squark mass $\tilde{m} = 100$ TeV in coloured (almost horizontal) lines [44]. Mass difference ΔM with which the thermal relic of the bino DM agrees to $\Omega_{\mathrm{DM}}h^2 = 0.12$ is also shown in the black solid line for the case in which the bino-gluino chemical equilibrium is assumed to be kept until when freeze-out occurs, while the cases for $\tilde{m} = 100$, 300 and 500 TeV are given in the dashed black lines.

Chapter 3

The LHC and ATLAS Experiment

A brief overview of the LHC and ATLAS experiment is given in this chapter. Comparatively more spaces are devoted for subdetectors deeply related to this analysis. Full detail of the LHC and the ATLAS detector can be found in Ref. [6] and Ref. [5], respectively.

3.1 The Large Hadron Collider

The LHC is a circular particle accelerator located at the Centre for European Nuclear Research (CERN, *Conseil Européen pour la Recherche Nucléaire*) on the border of Switzerland and France. The LHC was constructed in the already existing underground tunnel of the Large Electron Positron (LEP) collider . Taking advantage of its exceptional circumference of about 27 km, the LHC complex has achieved to collide protons and heavy ions with the world largest energy. The LHC has been operational with a centre of mass energy of 7 TeV from 2009 to 2011, 8 TeV in 2012 or 13 TeV since 2015 as a proton-proton collider. Nominal design parameters of the LHC are summarised in Tab. 3.1. In addition, the LHC carries out proton-lead and lead-lead collisions although these interesting contents are not touched further in this dissertation.

Four main independent experiments have taken place at the four points of beam collisions of the LHC. The experiments are known as, A Large Ion Collider Experiment (ALICE), ATLAS, Compact Muon Solenoid (CMS) and Large Hadron Collider beauty (LHCb), which are arranged along the circumference of the LHC as shown in Fig. 3.1. A flow of the beam acceleration begins with the production of protons from a simple bottle of hydrogen gas by applying an electric field over the gas to remove their electrons. The Linear accelerator 2 (Linac 2) with the length of 30 m accelerates the protons

Table 3.1: Nominal design parameters of the LHC as a proton-proton collider [6].

Parameter	**Value**
Ring circumference	26.7 km
Centre of mass beam energy $\sqrt{s}$	14 TeV
Instantaneous luminosity L	$10^{34}\,\mathrm{cm}^{-2}\,\mathrm{s}^{-1}$
Total cross section σ_{tot}	80 mb $(= 8 \times 10^{-26}\,\mathrm{cm}^2)$
The number of protons per bunch	1.15×10^{11}
The number of bunches in ring	2,808
Bunch spacing	25 ns
Average number of interactions per bunch crossing $< \mu >$	~ 23

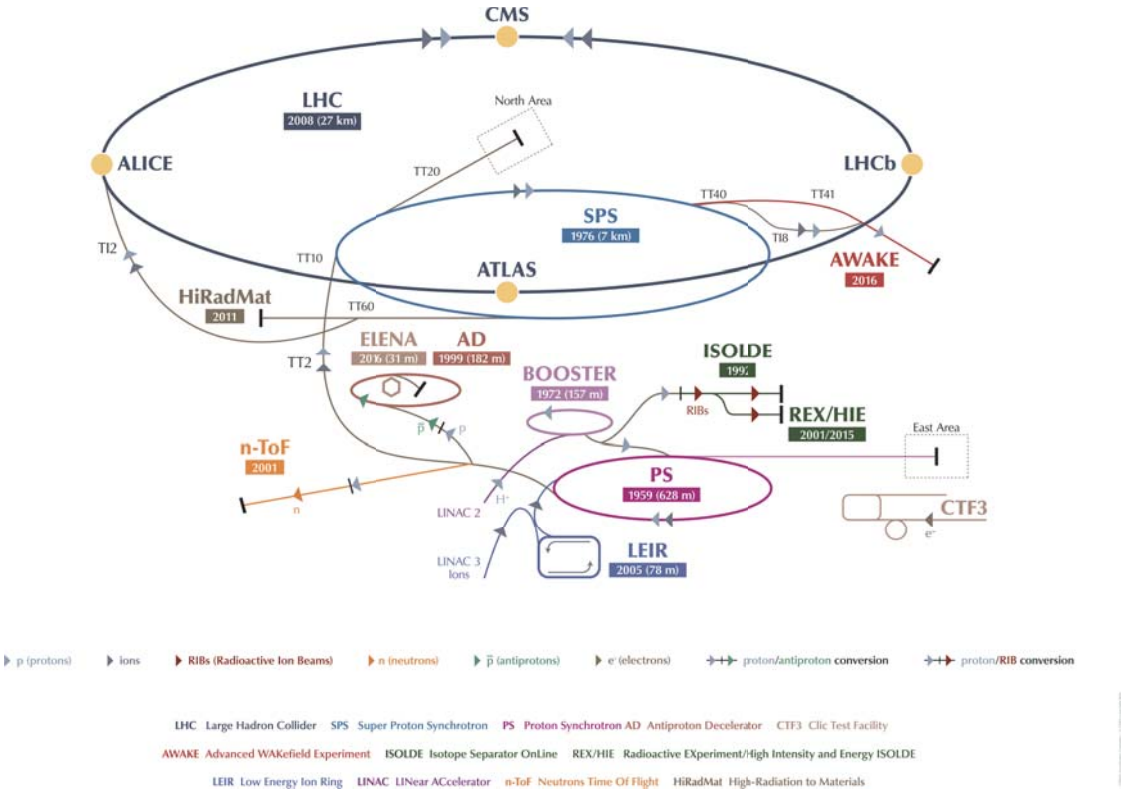

Figure 3.1: The accelerator complex at CERN, showing the flow of beam acceleration from the injectors to the LHC. A subset of the many experiments supported by these accelerators is also shown. [45]

to the energy of 50 MeV. The beam is then injected to 157 m circumference Proton Synchrotron Booster (PSB), which accelerates the protons to 1.4 GeV, and subsequently is driven to 628 m circumference Proton Synchrotron (PS), which increases the beam energy to 25 GeV. The Super Proton Synchrotron (SPS) with the circumference of 6.9 km receives the beam and accelerates it to 450 GeV before providing it for the LHC. The beam is finally injected to the two beam pipes of the 26.7 km circumference LHC, which accelerates the beam energy to 3.5 TeV (in 2010 and 2011), 4 TeV (in 2012), 6.5 TeV (in 2015 and 2016) and higher in the future.

A set of protons revolves clockwise in one of the two beam pipe, while a beam in the other pipe circulates anticlockwise. The proton beams consist of bunches of protons. The bunches are squeezed using quadruple magnets and collide with each other with the crossing angle of 150-200 μrad at the interaction points where the above detectors are located. The time interval between bunches is 25 ns, i.e., the collision frequency is 40 MHz. The occurrence rate of interesting physics events is related to the *luminosity* $\mathcal{L}$ of the beams as well as the cross section of the event σ. The number of events in a unit of time is given as the product of the luminosity and the cross section:

$$\frac{d\mathrm{N}_{\mathrm{events}}}{d\mathrm{t}} = \mathcal{L}\sigma(\sqrt{s}), \tag{3.1}$$

where $\sqrt{s}$ is the collision energy in centre of mass system. The luminosity is described

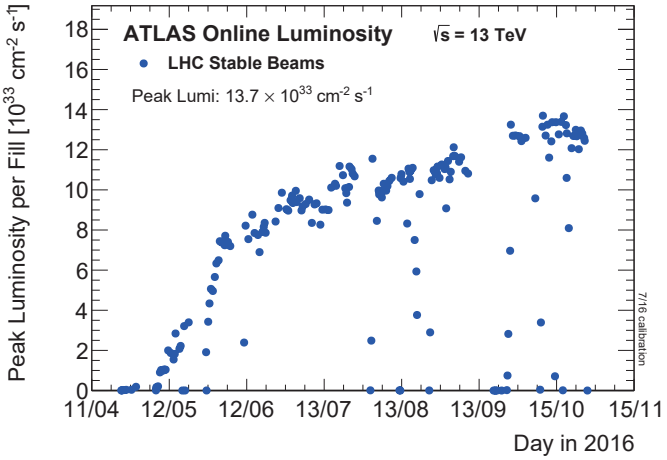

Figure 3.2: The peak instantaneous luminosity delivered to ATLAS during stable beams for pp collisions at 13 TeV centre-of-mass energy is shown for each LHC fill as a function of time in 2016 [47].

with the frequency of collision and variables related to the sizes of the beams:

$$\mathcal{L} \simeq \frac{f_{\text{crossing}} N_{\text{bunch1}} N_{\text{bunch2}}}{4\varepsilon\beta^*}, \tag{3.2}$$

where f_{crossing} is the collision frequency, N_{bunch1} and N_{bunch2} are the numbers of protons in each bunch, ε is the beam emittance and β^* is the beta function at an interaction point which is related to the transverse size of the bunch σ_{ts} as $\beta = \pi\sigma_{\text{ts}}^2/\varepsilon$ [46]. The peak instantaneous luminosity of stable proton beams delivered to the ATLAS detector in 2016 is shown in Fig. 3.2.

Increasing the luminosity links to a rise in the rate of interesting physics as well as creation of pileup[1] collisions within a bunch crossing. The ATLAS detector was designed to record data efficiently in high pileup environment. Parameters on pileup generally used in the ATLAS experiment are the number of reconstructed primary vertices N_{PV} and the average number of interactions per bunch crossing μ. N_{PV} is measured by the ATLAS inner tracker, which can detect charged particles every 25 ns. As for μ, it is calculated from the luminosity and averaged over certain interval of an event block. When μ is fixed, N_{PV} is proportional to an amount of *in-time* pileup, which increases the energy measured by calorimeters in an event. On the other hand, when N_{PV} is fixed, μ is a parameter for *out-of-time* pileup, which decreases observed energy due to negative energy tail in pulse shape of the ATLAS liquid argon calorimeter[2] [5]. The μ measured during the 2016 data taking is shown in Fig. 3.3.

[1] Due to the high luminosity, tens of collisions occur when a pair of proton bunches crosses on average. In this dissertation, a vertex with the largest scalar sum of transverse momenta of associated tracks $\sum |p_{\text{T}}|$ is defined as a *primary vertex* and the rest of collisions (vertices) is called *pileup* events.

[2] The ATLAS liquid argon calorimeter is a sampling calorimeter which uses lead as absorber and liquid argon as active material. More detail of the calorimeter is given in Section 3.2.2.

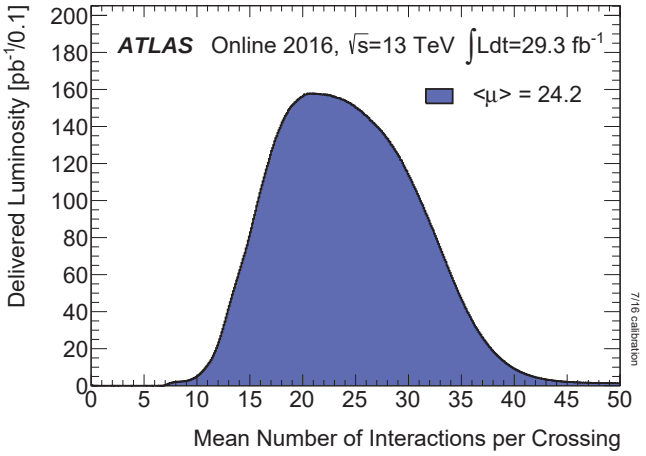

Figure 3.3: The luminosity-weighted distribution of the mean number of interactions per crossing for the 2016 pp collision data recorded [47]. All data delivered to ATLAS during stable beams is shown, and the integrated luminosity and the mean mu value are given in the figure.

3.2 The ATLAS Detector

The ATLAS detector is a large general purpose detector constructed for the measurement of proton-proton collisions and heavy ion-heavy ion collisions in the LHC. A cylindrical coordinate system is commonly used in the ATLAS experiments because of its shape shown in Fig. 3.4. The point of collision of proton bunches is defined as the origin of the coordinate system. A direction parallel to the beams is defined as the z axis, and the plane perpendicular to the beam direction is defined as the x–y plane. The positive direction of the x axis is pointing to the centre of the LHC ring, and the positive direction of the y axis is the ground right above the detector. A positive side of the z axis is called 'side-A', and the negative side is called 'side-C'. The azimuth angle ϕ is the angle measured around the z axis and the polar angle θ is the angle against the z axis. A variable called pseudo-rapidity $\eta = -\ln[\tan(\theta/2)]$ is often used instead of θ [3]. Transverse momentum $p_{\mathrm{T}} \equiv \sqrt{p_x^2 + p_y^2}$, transverse energy $E_{\mathrm{T}} \equiv \sqrt{E_x^2 + E_y^2}$ and missing transverse energy $E_{\mathrm{T}}^{\mathrm{miss}}$ are momentum, energy, and missing energy projected on x–y plane, respectively. Distance between two objects in η–ϕ plane ΔR is defined as $\Delta R \equiv \sqrt{\Delta\eta^2 + \Delta\phi^2}$.

The inner tracking detector (ID) consists of a silicon pixel detector (Pixel), a silicon strip detector (SCT), and a transition radiation detector (TRT). The ID is surrounded by a superconducting solenoid magnet which applies a 2 T magnetic field. A high density sampling electromagnetic (EM) calorimeter is located on the outside. The EM calorimeter uses lead as an absorber and liquid argon (LAr) as active material. The EM calorimeter consists of a barrel region on the centre side ($|\eta| < 1.475$), the outer wheel of the end cap region ($1.375 < |\eta| < 2.5$), the inner wheel of the end cap region ($2.5 < |\eta| < 3.2$). The region ($|\eta| < 2.5$) of the EM calorimeter where the ID exists inside is divided into three layers in the radial direction. The first layer is finely segmented in the direction of η, and possible to distinguish single photon shower from two photon

[3] Rapidity $y = 1/2 \ln[(E + p_z)/(E - p_z)]$ is sometimes used for a heavy object, such as a jet, instead of η

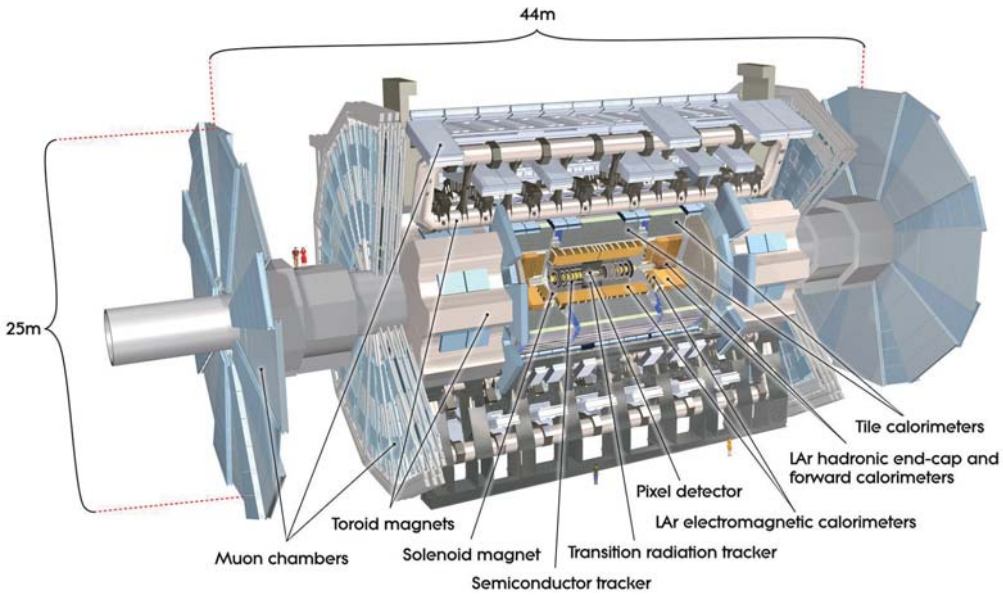

Figure 3.4: Sectional view of the ATLAS detector [48]. The height of the ATLAS detector is 25 m, the length is 44 m, and the weight is approximately 7000 tons.

showers due to decay of π^0. The first layer is also used to improve the resolution of the shower position and the shower direction measurement. In the region of $|\eta| < 1.8$ between the TRT and the EM calorimeter, there is a detector called pre-sampler, which compensates for energy loss before the calorimeter. The Hadron calorimeter exploits two different technologies in barrel part with $|\eta| < 1.7$ and end cap part with $1.5 < |\eta| < 3.2$. The barrel portion is composed of a tile calorimeter that uses iron plates as absorber and accumulates the energy with plastic scintillators, while the end cap portion is an LAr calorimeter. In the forward direction ($3.2 < |\eta| < 4.9$), LAr calorimeters are used as both electromagnetic and hadron calorimeters. The muon spectrometer (MS) surrounds the calorimeter and consists of three large superconducting toroidal magnets, high precision tracking detectors, and detectors for high speed trigger. Each superconducting toroidal magnets is made up of eight coils. By combining these detectors, highly accurate measurement of charged particles in the area of $|\eta| < 2.5$ can be realised. Also, photon, jet and missing transverse energy are reconstructed by energy measurement at $|\eta| < 4.9$. Further information on each subdetector are given in the coming sections.

3.2.1 Inner Detector

The ATLAS inner detector, which consists of three sub-detectors, Pixel detector (Pixel), Semiconductor Tracker (SCT) and Transition Radiation Tracker (TRT), is surrounded by a superconducting solenoid magnet which generates a 2 T magnetic field. The tracker is designed to provide precise track and vertex reconstruction with high momentum resolution within $|\eta| < 2.5$. The nominal lower track p_{T} threshold is 400 MeV, although lower threshold can be tuned for different use cases. Electron identification is also performed with the TRT taking advantage of large amount of its transition radiation over a large kinematic range of 500 MeV to 150 GeV within $|\eta| < 2.0$ corresponding to the coverage of the TRT in η direction. A schematic r–z cross section of the ATLAS inner detector

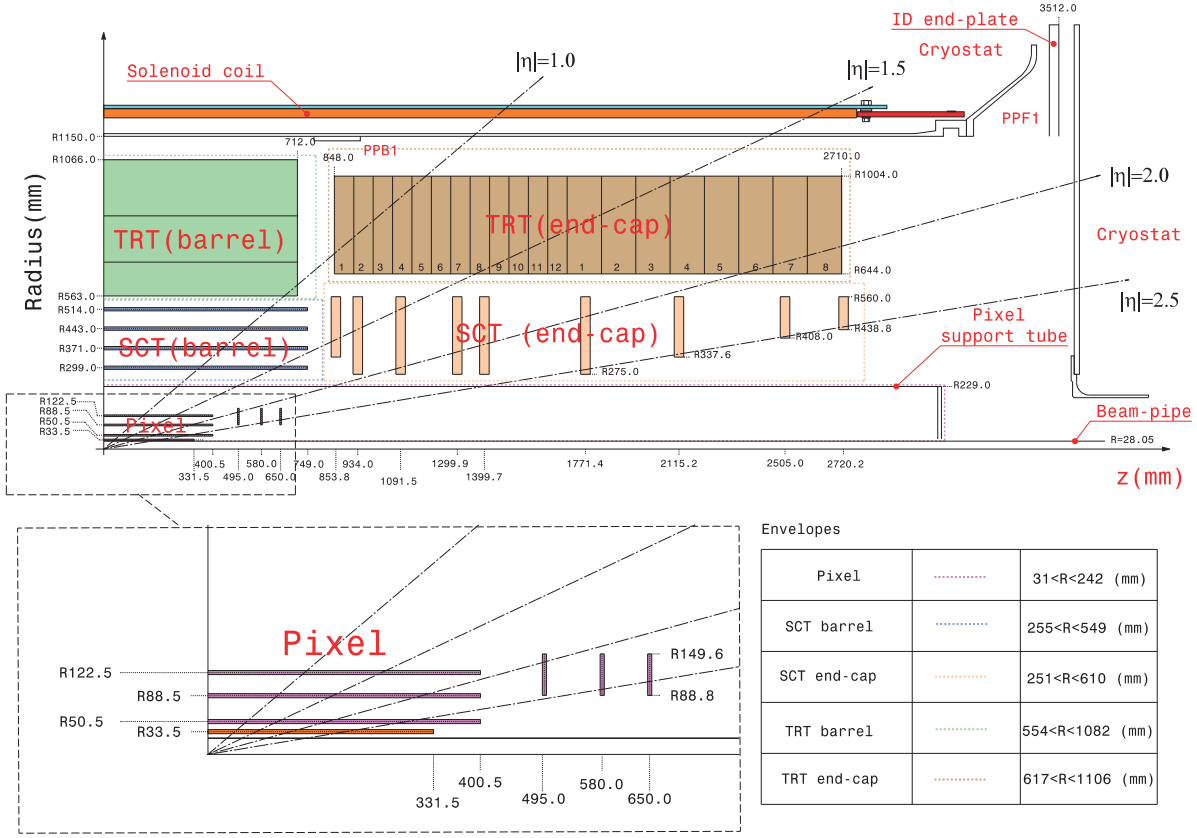

Figure 3.5: The r–z cross section of a schematic diagram of the ATLAS inner detector for Run 2. The upper pad shows the whole Inner Detector, whereas the lower panel shows a zoomed view of only the IBL (orange) and Pixel (purple) region. [49]

is shown in Figure 3.5. The layout of the ATLAS inner detector is also illustrated in Figure 3.6.

Pixel

The innermost subdetector of the ATLAS inner detector is the Pixel, which contains four layers of high-granularity and highly radiation tolerant semiconductor modules.

The innermost layer of the Pixel detector is called Insertable B-Layer (IBL) [51, 52], which was newly installed in May 2014 during the long shutdown 1 of the LHC in order to preserve tracking performance from Run 2. The IBL modules are arranged in a cylindrical layer which consists of 14 staves surrounding the beam pipe and the layer is located at radius r of 33.25 mm from the interaction point. Each IBL stave contains 12 double-chip planar sensor modules located at the centre of the stave, and 4 single-chip 3D sensor modules at each end of the stave, in the forward direction. The signal from each sensor is processed by a new front-end (FE) readout chip FE-I4 [53] which is connected with the sensors by flip-chip bump bonding at IZM[4]. All planar sensors were produced

[4] *Fraunhofer IZM-Berlin, Gustav-Meyer-Allee 25, 13355 Berlin*

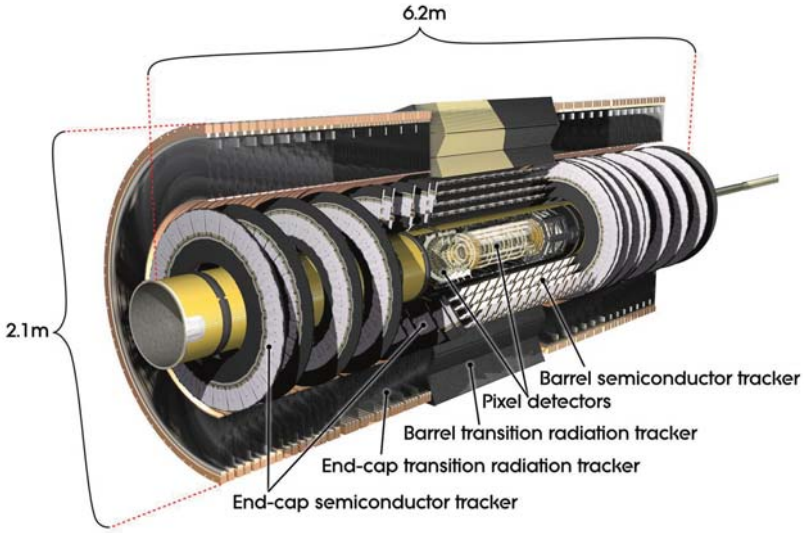

Figure 3.6: Computer generated cut-away view of the ATLAS inner detector. [50]

at CiS[5] and the 3D sensors were produced at CNM[6] or FBK[7].

A conservative and well-established n^+-in-n technology is adopted for the IBL planar pixel sensors, which is similar to the technology used for the original ATLAS pixel detector. The thickness of the IBL planar sensors is reduced to 200 μm and the inactive edge is minimised to 200 μm, resulting in higher radiation tolerance and smaller insensitive region at the sensor edges.

The 3D sensor is a new technology with a complex fabrication process and it is one of the most radiation-hard designs currently available. The 3D columns in the IBL 3D sensor are obtained by processing each side of the silicon wafer. The n^+ columns are obtained by first etching and then doping on the front side, and a similar process is then applied on the back side of the sensor to obtain the p^+ columns [54]. This is the first time that the 3D sensor technology is used in a high energy physics experiment.

FE-I4 is the largest FE chip for pixel detectors for high energy physics. The FE-I4 is produced using the 130 nm CMOS technology and contains approximately 70 million transistors. The pixel readout is arranged in 80 columns and 336 rows, and each pixel has a size of 250×50 μm^2. Each chip has an area of 20.2×18.8 mm^2, of which 90% corresponds to the active area on the sensor. Each pair of columns are further divided into regions of 2 by 2 pixels that share a local memory, where hits can be stored locally until a Level 1 trigger is received, avoiding the bottleneck problem of the existing FE chip in which the buffers are located at the end of a double column [55].

The other three barrel layers and three endcaps contain 1744 planar sensor modules and each is composed of 16 FE-I3 chips [55]. A 3D computer graphic of the Pixel detector without the IBL is shown in Fig. 3.7. An FE-I3 chip contains 2880 pixels in a matrix of 18 columns and 160 rows, which are individually 250 μm thick and the pixel size is 400×50 μm^2. This segmentation achieves good position resolution, for instance, an

[5] *Forschungsinstitut fur Mikrosensorik und Photovoltaik GmbH, Konrad-Zuse-Strasse 14, 99099 Erfurt, Germany*

[6] *Centro Nacional de Microelectronica (CNM-IMB-CSIC), Campus Universidad Autonoma de Barcelona, 08193 Bellaterra (Barcelona), Spain*

[7] *Fondazione Bruno Kessler, Via Sommarive 18, 38123 Povo di Trento, Italy*

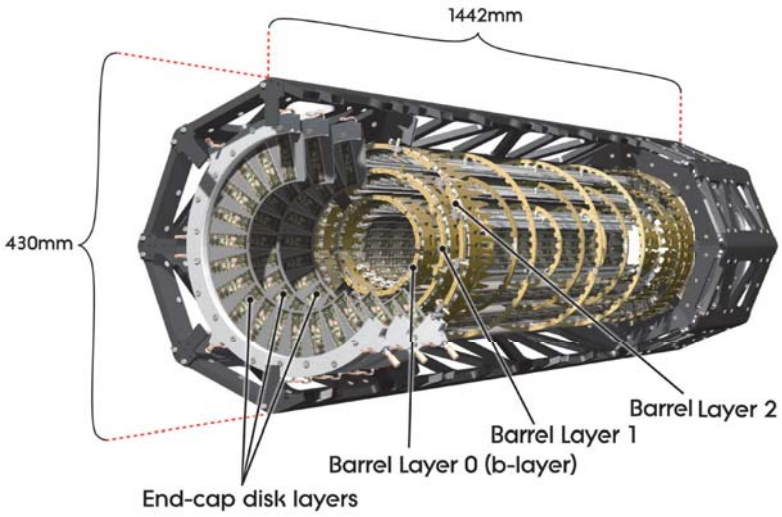

Figure 3.7: Cut-away view of the Pixel, part of the ATLAS inner detector [56]. The IBL is not included here. The diameter and length of the pixel support frame is also shown.

individual layer resolution of 10 μm in the transverse ($r - \phi$) plane and 115 μm in the axial plane (z, barrel) or radial plane (r, endcaps). The three barrel layers of the Pixel detector are located at $r = 50.5$, 88.5, and 122.5 mm from the interaction point and the three endcap layers are located at $z = 495$, 580, and 650 mm from the interaction point.

SCT

The second subdetector of the ATLAS inner detector is called the SCT, which contains several layers of microstrip silicon modules. 15,912 sensors in total forms four layers in the barrel, and nine layers are located in the endcap. The length of a strip is 6 cm and it is arranged with a pitch of 80 μm. A SCT module is composed of a pair of two SCT sensors tilted by 20 mrad against its counterpart to perform measurement of 3D position of a charged particle. This segmentation achieves intrinsic accuracies of 17 μm in the transverse (R-ϕ) plane and 580 μm in longitudinal (z for barrel or r for endcap) direction. The total number of readout channels in the SCT is approximately 6.3 million.

The four barrel layers of the SCT are located at $r = 299$, 371, 443, and 514 mm from the interaction point and the nine endcap layers are located at $z = 853.8$, 934, 1091.5, 1299.9, 1399.7, 1771.4, 2115.2, 2505, and 2720.2 mm from the interaction point.

TRT

The third and outermost subsystem of the ATLAS inner detector is the TRT, which is composed of 370 thousand straw-shaped drift tubes with the diameter of 4 mm. Any charged particles ionise the gas mixture of 70% Xe, 27% CO_2, and 3% O_2 inside the straws. The generated electrons are amplified when they drift in the electric field towards the central anode wire. The FE electronics samples the signal in 24 time bins with the width of 3.12 ns and compares it against a threshold corresponding to 300 eV. The electrons take up to 48 ns to reach the wire on average. The arrival time of the first electron can be used to determine the position, where the particle passed through, from the centre of the straw.

Table 3.2: Position and number information of the Pixel and IBL [51]. Positions of support structures denoted as Envelop is also shown as well as those of the sensitive materials.

Item		**Radial Extension** [mm]	**Length** [mm]	**Staves / Sectors**	**Modules**	**Pixels** ($\times 10^6$)
Beam pipe (with IBL)		$25 < R < 29$				
IBL	Envelope	$31.0 < R < 40.0$				
	Sensitive	$< R >= 33.25$	$\|Z\| < 332$	14	224	12.0
Pixel	Envelope	$45.5 < R < 241.0$	$\|Z\| < 3092$			
B-layer	Sensitive	$< R >= 50.5$	$\|Z\| < 400.5$	22	286	13.2
Layer 1	Sensitive	$< R >= 88.5$	$\|Z\| < 400.5$	38	494	22.8
Layer 2	Sensitive	$< R >= 122.5$	$\|Z\| < 400.5$	52	676	31.2
Disk 1	Sensitive	$88.8 < R < 149.6$	$< Z >= 495$	8×2	48×2	4.4
Disk 2	Sensitive	$88.8 < R < 149.6$	$< Z >= 580$	8×2	48×2	4.4
Disk 3	Sensitive	$88.8 < R < 149.6$	$< Z >= 650$	8×2	48×2	4.4
					Pixel Total	92.4

The regions between up to 73 (160) layers of polyimide straw tubes are filled with polymer fibres (barrel) or foils (endcaps). Transition radiation is emitted by highly relativistic charged particles (with the Lorentz boost factor $\gtrsim 1000$) when they pass over the boundary. In general, an amount of the transition radiation of an electron is larger than that of a pion, which might mimic an electron, so that the TRT is used to identify electrons as well. The position resolution of the TRT is significantly poorer than the Pixel or the SCT, with the entire detector providing a resolution of 130 μm. However the TRT enhances momentum resolution with its long lever arm for continuous tracking.

The barrel of the TRT is positioned from 563 to 1066 mm in r with respect to the interaction point, while the endcap covers 848 to 2710 mm in z. The coverage of the barrel is within $|\eta| < 1.0$, and the endcap reaches up to $|\eta| \approx 2.0$, rather than 2.5 like the Pixel and SCT.

3.2.2 Calorimeters

The electromagnetic (EM) and hadronic calorimeters are combination of multiple sub-detectors covering up to $|\eta| < 4.9$. The EM barrel calorimeter uses a liquid argon (LAr) as active medium and lead as absorbers. In the region with $|\eta| < 1.7$, the hadronic (Tile) calorimeter is constructed from steel absorber and scintillator tiles with a ratio by volume of approximately 4.7:1 and is separated into barrel ($|\eta| < 1.0$) and extended barrel ($0.8 < |\eta| < 1.7$) sections. The calorimeter end-cap ($1.375 < |\eta| < 3.2$) and forward ($3.1 < |\eta| < 4.9$) regions are instrumented with LAr calorimeters for both EM and hadronic energy measurements. The LAr barrel has three longitudinal EM layers as shown in Figure 3.8(a), the LAr end-cap has three EM layers (EMEC) and four hadronic layers (HEC), the forward LAr calorimeter (FCal) has three layers, and the Tile calorimeter has three longitudinal layers. In addition, there is a pre-sampler (PS) layer in front of the LAr electromagnetic calorimeter within $|\eta| < 1.8$ that provides a measurement of the energy lost in non-instrumented material in front of the EM calorimeter. The

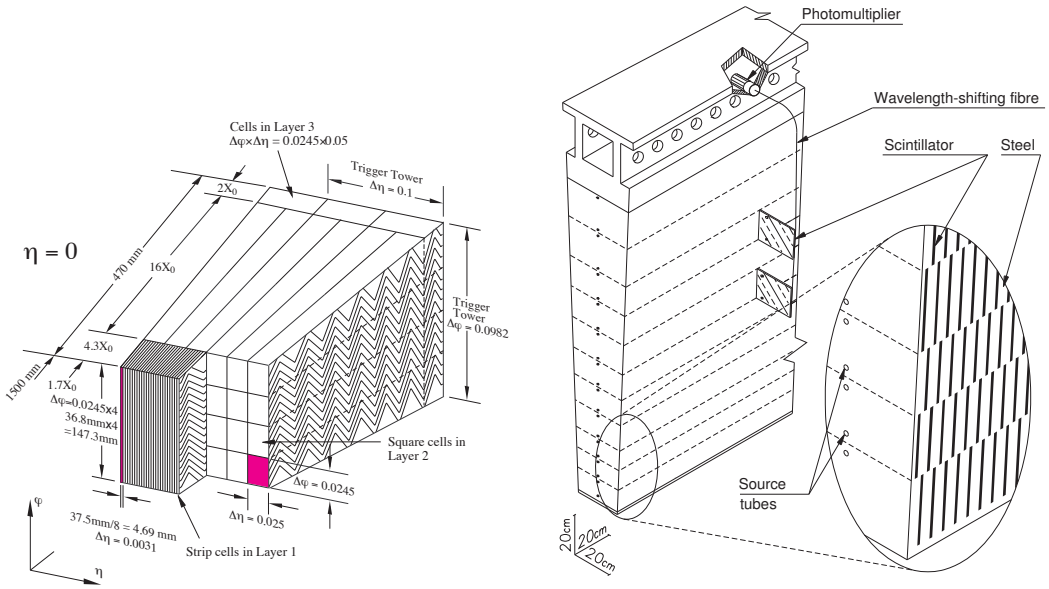

(a) (b)

Figure 3.8: (a) Sketch of a barrel module where the different layers are clearly visible with the ganging of electrodes in ϕ. The granularity in η and ϕ of the cells of each of the three layers and of the trigger towers is also shown. (b) Schematic showing how the mechanical assembly and the optical readout of the tile calorimeter are integrated together. The various components of the optical readout, namely the tiles, the fibres and the photomultipliers, are shown. [5]

analog signals of the LAr detector are sampled digitally once per bunch crossing over 4 bunch crossings and those measurements are converted to an energy measurement using constants calculated using dedicated calibration runs [5,57]. During the 2012 data-taking period, 5 samples instead of 4 were used in the LAr calorimeters energy measurement. The LAr readout is sensitive to signals from the preceding 12 bunch crossings during 50 ns bunch spacing operation [5,57]. For the 25 ns bunch spacing scenario this increases to 24 bunch crossings. The LAr detector has thus been exposed to more out-of-time pile-up since 2015 run. In contrast, the fast readout of the Tile calorimeter makes it relatively insensitive to out-of-time pile-up [58,59].

3.2.3 Muon Spectrometers

The muon spectrometers (MS) are the outermost subdetectors of the ATLAS detector. It is designed to reconstruct tracks of muons within the region up to $|\eta| = 2.7$. The relative resolution of the momentum is better than 3% over a wide p_T range and it is at most 10% at $p_T \approx 1$ TeV. The MS employs a toroidal magnet field provided by a system of three superconducting air-core toroidal magnets with the bending integral of about 2.5 Tm in the barrel region and up to 6 Tm in the endcaps.

The MS is composed of one barrel ($|\eta| < 1.05$) and two endcap sections ($1.05 < |\eta| < 2.7$) as illustrated in Fig. 3.9. Four kinds of detectors, Resistive Plate Chamber (RPC), Thin Gap Chamber (TGC), Monitored Drift Tube (MDT) and Cathode Strip

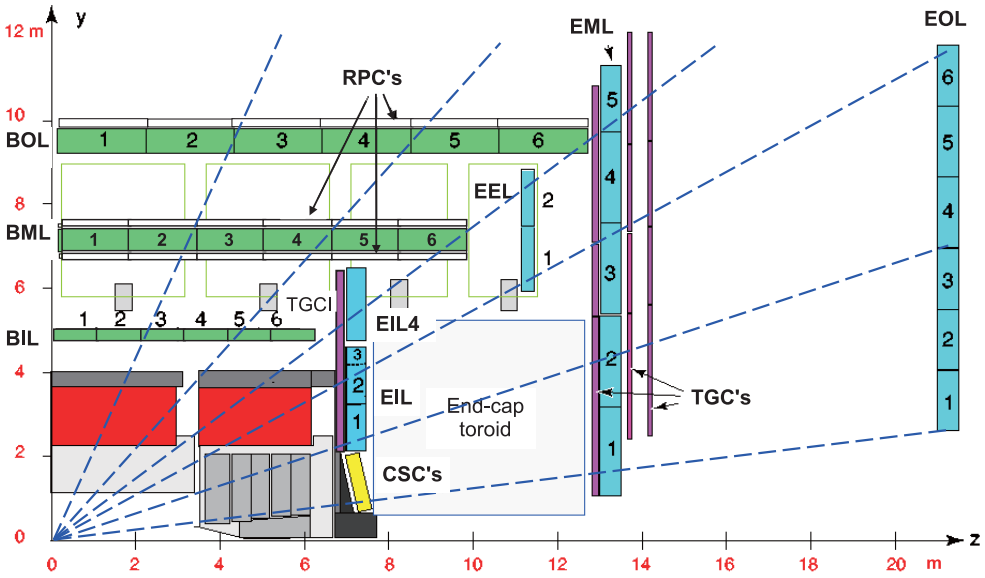

Figure 3.9: The yz cross section of a schematic diagram of the ATLAS muon spectrometers [5]. The white rectangles represent the RPCs, the green boxes represent barrel MDTs, the cyan boxes represent endcap the MDTs, the purple lines represent the TGCs and the yellow box represents the CSC.

Chamber (CSC), are used for each purpose. RPC, which is formed by three doublet layers for $|\eta| < 1.05$, and TGC consisting of one triplet layer followed by two doublets for $1.0 < |\eta| < 2.4$, provide precise position measurements of muons with typical spatial resolution of $5 - 10$ mm. These detectors are also used to trigger events in which a high momentum muon exists, taking advantage of the great timing resolution. Three layers of MDT provides a precise position and momentum measurement for muons passing through a region within $|\eta| < 2.7$. Typically a muon is detected at six to eight measurement points on each MDT layer (chamber). Instead of MDTs, The inner layer for $2 < |\eta| < 2.7$ is instrumented with CSC which is composed of 32 four-layer chambers with high timing resolution of few ns. The position resolution of the MDT and CSC for a single hit in the bending plane (r–z plane) is about 80 μm and 60 μm, respectively. Despite the tens metre size of the muon spectrometers, they are aligned with accuracy of 30-60 μm.

3.2.4 Trigger System

The vast majority of collision events is dominated by diffractive and inelastic QCD events which is not targeted in the ATLAS experiment. The cross sections and corresponding event rates of SM processes are shown in Fig. 3.10. The data acquisition (DAQ) system of the ATLAS, however, cannot afford to record all collision events. When the detectors detect a particular event with high p_{T} objects or large $E_{\mathrm{T}}^{\mathrm{miss}}$, a *trigger* is generated as a go sign to record data.

The trigger in the ATLAS experiment is a two stage system including a hardware-based Level-1 (L1), and the software-based High Level Trigger (HLT). The trigger system reduces the event rate from the bunch-crossing rate of 40 MHz to 100 kHz at L1 and to an average recording rate of 1 kHz after passing the HLT. The L1 is based on fast custom-made electronics; it collects coarse information from the calorimeter and the

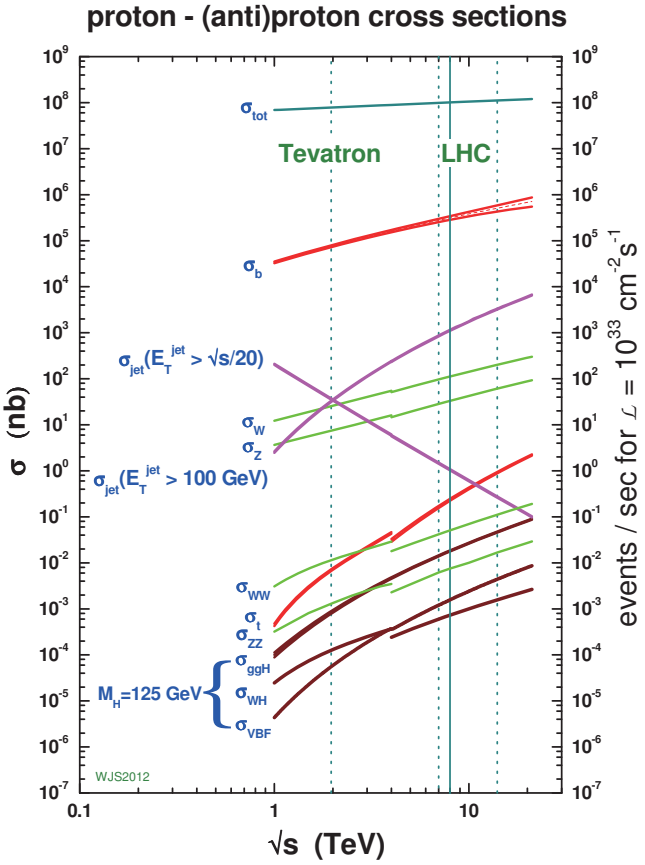

Figure 3.10: Standard Model cross sections and corresponding event rates as a function of collider energy, with 125 GeV Higgs [60].

muon spectrometer and processes it with a latency of less than 2.5 μs. The L1 trigger is composed of four different systems, i.e. the L1 calorimeter trigger system (L1Calo), the L1 muon trigger system (L1Muon), the Central Trigger Processors (CTP) and the L1 topological trigger modules (L1Topo). The HLT exploits fast offline-like algorithms to achieve higher resolution information than the L1. A processing time of the HLT is approximately 0.2 s per event on average. Regions of interest (RoI) are defined by the L1, and precise objects reconstruction is performed typically only there in order to save processing time. A schematic overview of the ATLAS Trigger and DAQ system is shown in Fig. 3.11.

3.2.5 Luminosity Detectors

The ATLAS uses several independent detectors for the luminosity measurement in order to control its systematic uncertainties. An overview of representative ones are briefly introduced in this section.

The LUCID (Luminosity measurement Using a Cherenkov Integrating Detector) is the only detector dedicated for luminosity measurement in the ATLAS. The LUCID consists of twenty aluminium tubes with the length of 1.5 m and the diameter of 15 mm

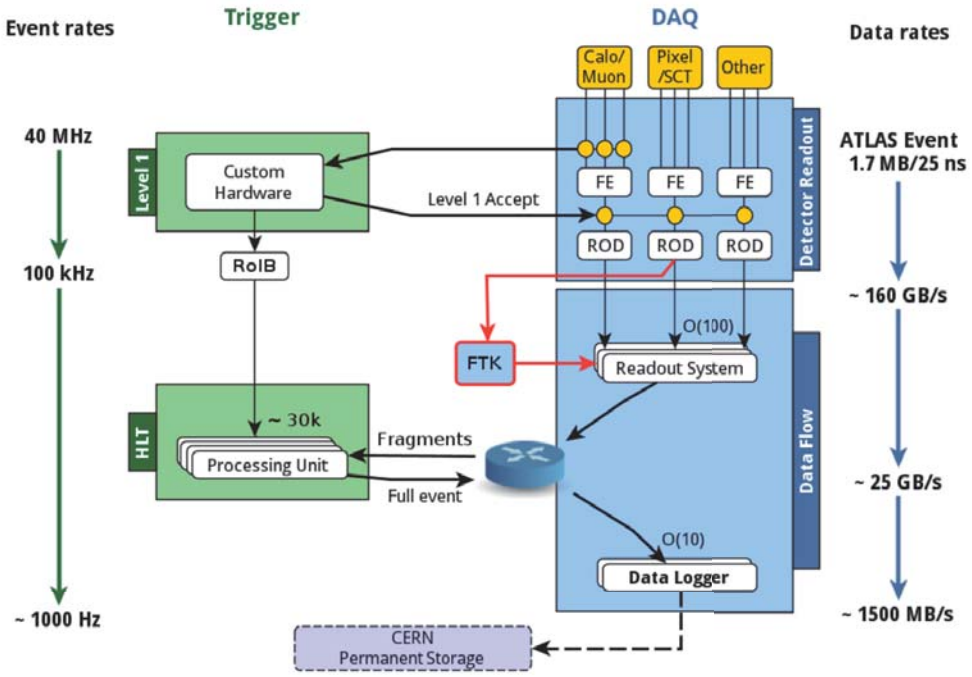

Figure 3.11: The setup of the ATLAS trigger and data acquisition system for Run 2 [61]. The event and data rates are also given.

each. These tubes surround the beam pipe symmetrically at about ±17 m. When a charged particle comes into a tube with the momentum above the Cherenkov threshold, Cherenkov light is emitted and then detected by a photomultiplier tube (PMT). The Beam Conditions Monitor (BCM) is a set of diamond sensors with the size of 1×1 cm^2 and 500 µm thickness each. Four sensor modules are located at the each side of the ATLAS at $z = \pm 184$ cm and $r = 55$ mm. The Zero Degree Calorimeter (ZDC) is a neutral particle detector located at $z = 140$ m covering small acceptance of $\eta > 8.3$. The ZDC consists of six modules which use tungsten plates as absorbers. Charged particles generated in the plates go into quartz strips, and then Cherenkov light is emitted and read out by PMTs. The Diamond Beam Monitor (DBM) is composed of diamond and silicon sensors covering the pseudo-rapidity range of $3.2 < |\eta| < 3.5$. The DBM is located at $z = \pm 90$ cm and tilted by ~ 70 mrad against the beam pipe. Four tracking telescopes (3 diamond + 1 silicon telescopes) are on each side. Each telescope consists of three layers of diamond or silicon sensors integrated with FE-I4 as same as the IBL.

In addition, the Minimum Bias Trigger Scintillators (MBTS), located between the inner detector and the EM calorimeter, is also used as one of the luminosity detectors covering the interval of $2.1 < |\eta| < 3.8$. Although the MBTS has large acceptance, it saturates at high luminosity. The forward calorimeter (FCAL) can measure luminosity by integrating energy deposition over long periods of time.

Chapter 4

Object Reconstruction

The conversion from detector readout signals to original physics objects is called *object reconstruction*. The physics analysis in this dissertation predominantly uses tracks and vertices, and the sensitivity of the search largely depends on the performance of their reconstruction. The standard reconstruction techniques of track and vertex as well as the ones which are specific to this analysis are discussed in this chapter. Other physics objects, such as electrons, muons, jets, and missing transverse momentum, are briefly outlined as they are partially used in the analysis as well.

4.1 Track and Vertex

One of the most fundamental and important parts of the physics analysis is track reconstruction. Charged particles are produced by the beam collisions, and they pass through the highly segmented detectors. They deposit the energies along their traverse through the detectors. By connecting the points where the detector hits are created, the paths of charged particles are reconstructed. Owing to the magnetic fields in the tracking volume, the path of a charged particle draws curve with a certain curvature. When a charged particle with the transverse momentum p_{T} passes through uniform magnetic field B, the relation between p_{T}, B and radius R of the circular motion is given as follows:

$$p_{\mathrm{T}}\,[\mathrm{GeV/c}] = 0.3 \cdot B\,[\mathrm{T}] \cdot R\,[\mathrm{m}]. \tag{4.1}$$

A crossing point of at least two tracks is called *vertex*. The reconstruction of production or decay positions of particles (vertices) is performed by finding the crossing points of tracks. For any analysis, it is important to find primary vertex to suppress effects from pileup collisions, and also b-jet tagging exploits a secondary vertex coming from the decay of b hadrons.

The standard tracking and vertex reconstruction will be reviewed in Section 4.1.1 and 4.1.3. The special reconstruction of tracks with large impact parameters and vertices largely displaced from the beam collision point will be given in Section 4.1.2 and 4.1.4, respectively.

4.1.1 Standard Tracking

The ATLAS inner trackers are composed of roughly two parts, finely segmented silicon detectors (Pixel and SCT) and thin long straw tube detector (TRT). Similarly, there

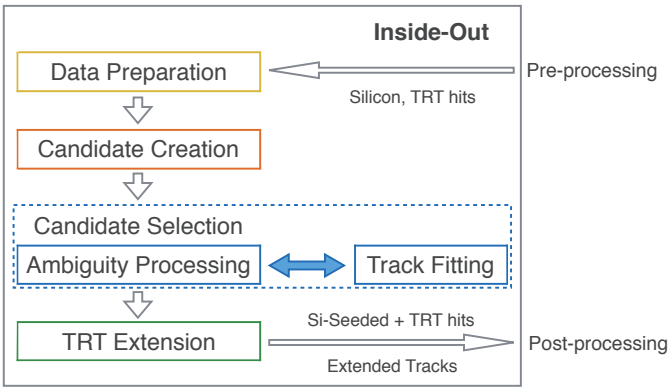

Figure 4.1: Schematic diagram of the standard inside-out tracking flow in the ATLAS experiment.

are two approaches in the track reconstruction with the inner trackers: the main *inside-out* track reconstruction and consecutive *outside-in* track reconstruction. The inside-out track reconstruction creates track seeds from silicon hits and extend them to TRT track segments, while the outside-in track reconstruction tries to extend TRT track segments to silicon hits. More details of the standard track reconstruction will be discussed in this section. Further technical and conceptual details of the standard track reconstruction of the ATLAS are summarised in Ref. [62].

Inside-out Track Reconstruction

The primary track finding in the ATLAS inner detector is based on an inside-out strategy for pattern recognition from measurement points. A schematic flow of the standard inside-out track finding is shown in Fig. 4.1. The inside-out track reconstruction can be divided into roughly four parts as follows.

(1) Space Point Formation: The first step of the inside-out track reconstruction is converting detector measurements into points on three dimensional coordinate, called *space point* objects. It is straightforward to form a space point from a measurement of Pixel which provides two dimensional position on its surface. A space point can be created by using the position information of a measurement on the detector surface and a position of the detector. As for a sensor of the SCT, a precise measurement is achieved only in transverse direction with respect to silicon strips. Since a SCT module is composed of a pair of two sensors tilted by 40 mrad, a measurement on the counterpart sensor is used to form a space point. When a pair of two SCT strips is found, the incident angle of a charged particle can be roughly estimated. The rate to create fake space points is reduced by restricting the incident angle to be compatible with the direction from the beam spot to the space points.

(2) Space Point seeded Track Finding: The track candidate search is carried out using the space point objects created in the previous step. To begin with, the track seed search is performed by connecting three silicon hits. Conventionally, the constraint on the z position of a primary vertex was used to suppress the number of seed combinations, however the standard seed search in this thesis is performed without the z constraint.

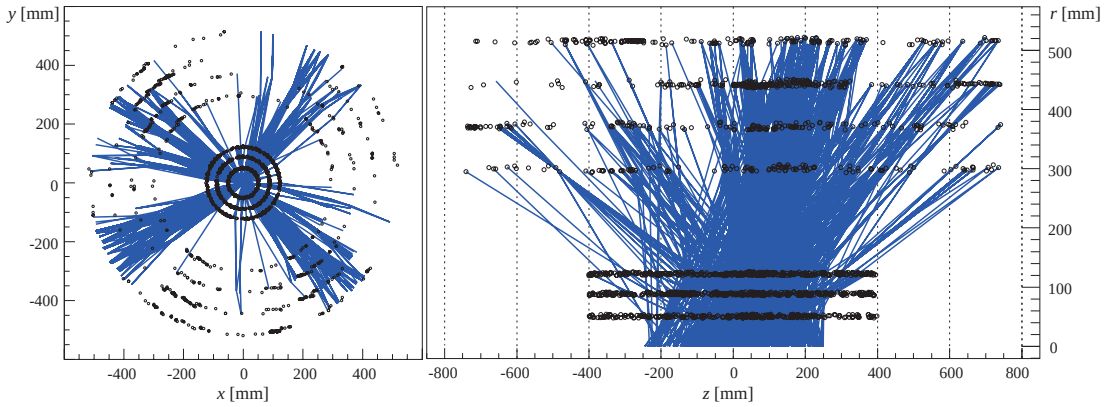

Figure 4.2: Space point seeds in the ATLAS inner detector barrel for a $t\bar{t}$ event [62]. The space point seeds built of three measurements are spread over a large z-range that leads to an increase of the track candidates for further processing.

The current one is more efficient to reconstruct tracks in events such as $H \to \gamma\gamma$ decays without tight constraint on primary vertices. Fig. 4.2 shows the track seeds created without z vertex constraint in a $t\bar{t}$ event of Monte Carlo simulation (MC).

Once the track seeds are found, then the track road building is performed, that is the further search of associated hits to a track candidate. The track parameters of the candidates could have been biased because the procedure of the track candidate finding was coarse. Therefore, the track is refitted using a combination of a standard Kalman filter and smoother [63] based on a least squares approach to obtain more precise track parameters. The Kalman filter, also known as linear quadratic estimation (LQE), is an algorithm that progressively estimates unknown variables using a set of measurements by taking into account statistical noise and other uncertainties. This can be used to estimate the track information and the covariances in the environment where, e.g., a huge number of hits exist and a trajectory does not always draw a simple curve due to scattering with detector materials.

(3) Ambiguity Solving: A large number of track candidates are created in the previous step of the track finding. Many of them are actually just fake tracks which are accidentally reconstructed from unrelated hits. In order to reject such tracks, the track candidates are ranked by order of the scores which are corresponding to the likelihoods. Before assigning scores to the track candidates, they are refitted using the refined geometry information with a detailed material description, and the χ^2 divided by the degrees of freedom (reduced χ^2) is obtained for each candidate. Not only reduced χ^2 but also a track scoring strategy [64] is used for the classification of tracks. A qualitative overview of the scoring strategy is given in Tab. 4.1. In general, the scoring rule is defined to give a better score to a track with relatively larger number of associated hits. If a detector layer does not have a hit on the intersection with a track, i.e. a track has a *hole*, a certain amount of penalty is given to the track. In case that a track, passing through a region where adjacent detector modules are overlapped as the track **b** in Fig. 4.3, has hits on the both modules, a strong benefit is added to the track score. When a hit is shared between different tracks, it is generally assigned to the track with better score and the

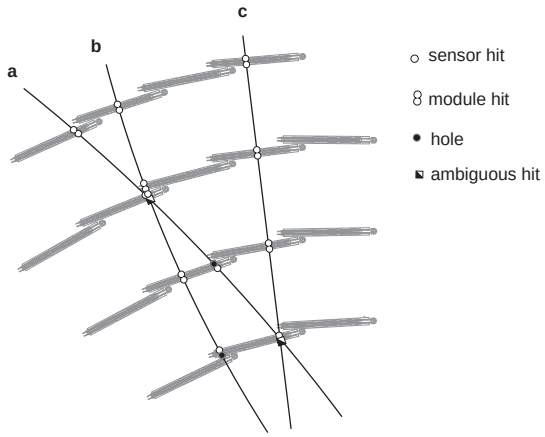

Figure 4.3: Simplified model of the ambiguity solving process, illustrated in the SCT Barrel [62]. Tracks **a**, **b** and **c** have been found through the seeded track finding, but share several hits. The χ^2/n_{dof} may not be appropriate to distinguish a true from a fake track, therefore dedicated track scoring that is optimised for each subdetector is used. In the shown example, e.g. a module hit representing measurements on both sides of the SCT silicon detector are scored relatively higher than two single hits without associated backside module. Hits in a overlap region as for track **b** are in particular high scored, while holes on track, i.e. an expected hit that has not been found, lead to a penalty in the track score.

other track is refitted again without the shared hit. After iterations of this procedure, the tracks whose scores are higher than a certain quality cut are stored.

(4) TRT Track Extension: The tracks which passed the ambiguity solving process are further tried to extend to the TRT measurements. A line fit is performed to estimate whether the hits on a TRT track segment are compatible with the silicon track or not in the r–ϕ coordinate for the barrel region and the r–z coordinate in the endcap regions, respectively. Fig. 4.4 shows a result of the extensions of the silicon tracks into the TRT for a MC generated $t\bar{t}$ event. If the track score of the original silicon track is higher than that of the track after extension, the original one is stored and the TRT hits are treated as *outlier*[1] measurements onto the track.

[1] *outlier* is a term of statistics which represents a data point on a graph that is very much bigger or smaller than the next nearest data point.

Table 4.1: Track characteristics that lead to benefits or penalties in the ATLAS silicon detector track score [62].

Track characteristics	Detector	Effect on the track score
IBL/B-Layer hole	Pixel	strong penalty
Layer hole	Pixel	penalty
Overlap hit	Pixel, SCT	strong benefit
Sensor hole	SCT	weak penalty
Layer hole (module)	SCT	strong penalty

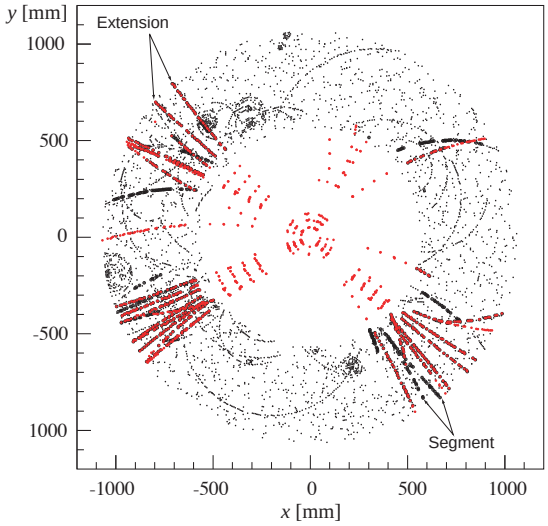

Figure 4.4: The $t\bar{t}$ event for the two possible TRT hit associations (only the barrel measurements): the brighter coloured hits show the extensions that originate from following the space point seeded tracks into the TRT, the silicon space point objects are also shown in the same colour. The black circles mark the hits that have been associated to TRT segments, which build the start point of the back tracking application. The particular power of the back tracking approach is to find the additional track segments, that have not been found through the inside-out sequence, simply for the fact that no appropriate silicon seed existed for the further extension process. This is mainly due to strong energy loss of the particle, or due to the fact that the track segments originate from photon conversions or other decay vertices inside the Inner Detector volume.

Outside-in Track Reconstruction

The inside-out track reconstruction is optimised to find relatively high p_{T} tracks coming from the beam collision point. Tracks from secondary decay vertices of long-lived particles, e.g. K_s, or from photon conversions into an electron-positron pair, are likely missed. Electrons losing the energies as bremsstrahlung might fail to be reconstructed as well. Such tracks are targets of the outside-in strategy of track reconstruction. The outside-in track reconstruction is carried out in a similar flow with the inside-out approach as schematically shown in Fig. 4.5. The TRT track segment finding exploits the Hough transformation [65]. This transforms the TRT hit positions on a track into lines which cross at the point in a parameter space. The crossing point specifies the actual parameters of the track line and the point can be determined by searching the position of peaks in a histogram which contains the lines in a parameter space. This method works when a track draws approximately straight line in the r–ϕ plane in the TRT barrel region and the r–z plane in the endcap part. The minimum p_{T} threshold for tracks is set at 2 GeV for the nominal outside-in tracking in 2016 data taking. Finally, the backward tracking of the segments into the hits on the silicon detectors is performed and the ambiguities are solved by the track scoring method.

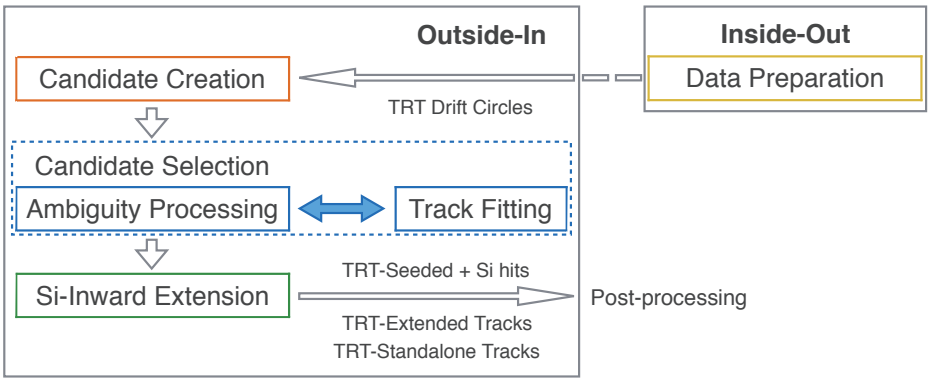

Figure 4.5: Schematic diagram of the standard outside-in tracking flow in the ATLAS experiment.

4.1.2 Reconstruction of Tracks with Large Impact Parameters

The ATLAS standard track reconstruction in the inner detector is composed of the two approaches of inside-out (first pass) and outside-in (second pass). A hypothetical heavy long-lived particle is, however, not efficient to be reconstructed with the standard tracking because of its constraint on the impact parameters, denoted as z_0 for the beam direction and d_0 for the transverse plane. Tracks from decay of the heavy long-lived particle are likely to have the large impact parameters. In order to improve the tracking efficiency for tracks with large impact parameters, a specialised third-pass tracking, *re-tracking* [66], is successively performed after the standard trackings. The re-tracking is based on the standard inside-out sequence where the hits used to seed and construct the tracks are the leftovers of the previous steps. Some modifications in the algorithm cuts allow to increase the efficiency for tracks with large impact parameters without including too many fake tracks. The main differences with respect to the standard sequence are follows:

1. the allowed region to search hits for seeding is slightly extended to the larger radius.
2. the cuts in the transverse and longitudinal impact parameter are loosened.
3. some quality cuts (hit-related mainly) are re-tuned.

The cuts applied in the standard ATLAS tracking algorithms (inside-out and outside-in) and re-tracking are listed in Tab. 4.2.

4.1.3 Primary Vertex Reconstruction

The procedure of primary vertex reconstruction can be divided into *vertex finding* and *vertex fitting* [67]. An iterative approach is used to the primary vertex reconstruction in the ATLAS experiment. The detailed procedure and performance of the iterative algorithm are described in Refs. [66, 68]. A brief overview of the primary vertex reconstruction is given in the following.

Tracks which passed the following requirements are considered to be used for constructions of the vertices [69]:

- $p_{\mathrm{T}} > 400$ MeV

Table 4.2: Cuts applied in the different tracking algorithms.

cut	inside-out	outside-in	large-d_0 tracking
max d_0	10 mm	100 mm	300 mm
max z_0	250 mm	-	1500 mm
min p_t	400 MeV	2 GeV	500 MeV
min Pix hits	0	-	0
min Si hits	7	4	7
min TRT hits	9*	15	9*
min NOT Shared	6	4	5
max Shared	1	1	2
max Si Holes	2	2	2
max Pixel Holes	1	2	1
max SCT Holes	2	2	2
max Double Holes	1	1	1

*on track extension

- $|\eta| < 2.5$
- Number of silicon hits ≥ 9 if $|\eta| \leq 1.65$ or 11 if $|\eta| > 1.65$
- Number of IBL hits + B-Layer hits ≥ 1
- A maximum of 1 shared module (1 shared pixel hit or 2 shared SCT hits)
- Number of Pixel holes $= 0$
- Number of SCT holes ≤ 1

An outline of the procedure of the iterative algorithm using the selected tracks is as follows:

1. The seed position of the vertex fitting is determined as the mode (most probable value) of the impact parameters z_0 with respect to the beam spot of all tracks. The mode in z is calculated using the Half-Sample Mode algorithm [70].

2. Tracks which are compatible with the seed are grouped together for the successive fitting.

3. With the seed position as the starting point and parameters of selected tracks as input, the adaptive vertex fitting algorithm with an annealing procedure [71] is used to estimate the position and covariance of the vertex. A weight reflecting the compatibility with the estimated vertex and the annealing temperature parameter is assigned to each input track.

4. After the vertex candidate is created, tracks that are not already fit to vertices are then used to repeat the process for a new vertex finding from the seeding step.

The iterative algorithm is tuned in advance to avoid assigning a single track to multiple reconstructed vertices.

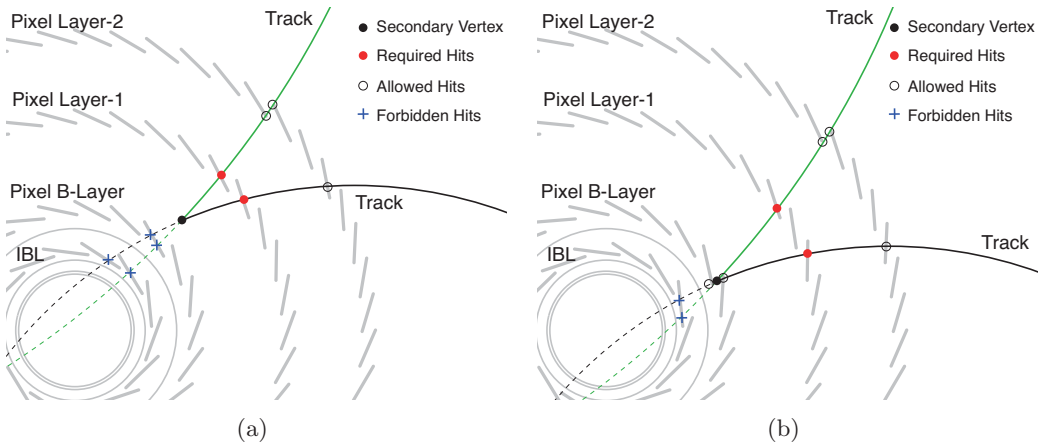

Figure 4.6: Schematic illustration of fake tracks rejection. (a) The vertex is between the two layers of B-Layer and Layer-1 sensors. The tracks of the reconstructed secondary vertex must not have hits on the layers inner than the vertex radius (i.e. IBL and B-Layer), and must have hits on the closest layer outside the vertex (i.e. Layer-1). (b) The vertex is close to the Pixel B-Layer sensors. In this example where the vertex is just inside the B-Layer, the tracks are not allowed to have hits on the IBL but may have hits on the B-Layer, and must have hits on the Layer-1. Analogous requirements are made on vertices close to the other layers [49].

4.1.4 Displaced Vertex Reconstruction

Vertices which are displaced with respect to the beam collision point are reconstructed using the `VKalVrt` vertex reconstruction algorithm [72]. The input tracks to this algorithm are required to pass the following additional requirements:

- Number of SCT hits ≥ 2
- Transverse momentum $p_{\mathrm{T}} > 1$ GeV
- Transverse impact parameter $|d_0| > 2$ mm
- Tracks are rejected if they have fewer than two Pixel hits *and* no TRT hits. This requirement is effective at removing fake tracks made up of hits in the SCT endcaps.

The algorithm, first, creates a set of two-track "seed" vertices using the incompatibility graph method [73]. The seed vertices are required to satisfy the fitting quality cut of $\chi^2/N_{\mathrm{dof}} < 5$. A functionality to reject a fake vertex is applied to these seed vertices. It requires certain hit patterns in the Pixel and SCT for tracks associated with the seed vertices. The hit patterns depend on the position of the reconstructed vertex. Fig. 4.6(a) schematically shows how the fake-tracks rejection works when a vertex is reconstructed in the middle of two adjacent layers. If a vertex is formed by tracks which have hits in the inner layers than the vertex position, the vertex is regarded as a fake and removed. The tracks are also required to have hits in the neighbour layer at larger radii. If a vertex is reconstructed around a detector layer, hits are required on the next outer layer and forbidden on the next inner layer as shown in Fig. 4.6(b).

The incompatibility graph is then applied again in order to use the surviving seed vertices to create all possible N-track vertices. At this point it is possible that the same

track is used in more than one vertex. An iterative "clean-up" algorithm is therefore applied as follows:

1. For all tracks that are used in more than one vertex, the vertex+track combination with the largest χ^2 is found.
2. If this χ^2 is greater than 6, or the two vertices are separated by more than 3σ (according to the uncertainties on their fitted positions), the track is removed from that vertex.
3. Otherwise, the two vertices are merged and fitted to obtain vertex parameters.
4. Return to step 1.
5. Once the process has converged such that there are no tracks shared between vertices, a final merging step is performed where pairs of vertices separated by less than 1 mm are merged, and the combined vertex is refitted.

4.2 Electron and Photon

The reconstruction of electrons and photons is performed on the measurements of electromagnetic showers in the electromagnetic calorimeter (ECAL). A brief overview of the reconstruction of electrons and photons is summarised in this section. Further details can be found in, e.g. Refs. [74, 75].

The signal pulse from each calorimeter cell (of electromagnetic or hadronic calorimeter) is sampled by the readout electronics. The amplitude of the signal is estimated by fitting the sampled points with a template of signal shape. The amplitude is then converted into the energy deposited in the cell of the calorimeter using a hardware calibration.

The reconstruction of electrons and photons is performed using information of energy deposits in the Electromagnetic Calorimeter (ECAL). The energy deposits in adjacent cells are summed up and a set of the cells are called a *cluster*. The standard clustering algorithm for electrons and photons reconstruction in the ATLAS is the "sliding-window" algorithm. This algorithm sums energy deposits in cells within a fixed-size rectangular window and the position of the window is scanned such that the energy in the window is a local maximum. The cluster window size in the barrel region is defined as 3×7 cells in the middle layer of the ECAL. The size is equivalent to an area of size $\Delta\eta \times \Delta\phi = 0.075 \times 0.175$). On the other hand, a cluster size of 5×5 cells in the middle layer is used in the endcap regions, corresponding to an area of $\Delta\eta \times \Delta\phi = 0.125 \times 0.125$. The ϕ size of the cluster is increased because the electron trajectory is bended in the ϕ direction due to the magnetic field of the solenoid. In the endcaps, the effect of the magnetic field is relatively small.

Electron and photon cannot be distinguished only from the energy deposits in the ECAL. The classification of them is based on the presence of tracks reconstructed in the inner detector, which are associated with the ECAL clusters. If no track matches a cluster, it is classified as an "unconverted photon". If a pair of oppositely charged tracks identified as electrons in the TRT is associated with a cluster and the tracks are nearly collimated at the production vertex, the cluster is classified as a "converted photon". In order to take track reconstruction inefficiency at large radius, a cluster which matches one track is also classified as a converted photon if the track have no hit on the innermost

layer of the Pixel. The other clusters which are associated with track passing a certain quality cut are classified as electrons.

4.3 Muon

The reconstruction of muon is performed using independent track reconstruction in the inner detector (ID) and muon spectrometers (MS). The track reconstruction in the ID was already given in Section Section 4.1. The track reconstruction in the MS is described in, e.g. Ref. [76]. This section is devoted to an overview of the combined muon reconstruction using information of the ID and MS.

4.3.1 Combined reconstruction

Several algorithms are used in the combined muon reconstruction in order to minimise the geometrical inefficiency. The combined muons are categorised into four types depending on subdetectors used in reconstruction as follows:

- Combined (CB) muon: is formed by globally refitting the hits on the ID and MS. The combined muons are generally reconstructed with an outside-in approach, i.e. extrapolating a track in the MS inward to a matched ID track. An inside-out reconstruction for combined muon is used as a complementary approach.

- Segment-tagged (ST) muon: is an ID track which, once extrapolated to the MS, matches at least one local track segment in the MDT or CSC chambers (see Section 3.2.3. The ST muons are selected if muons go across only one layer of MS chambers to save those with low p_{T} or passing regions where the MS do not cover.

- Calorimeter-tagged (CT) muon: is an ID track which is associated with an energy deposit in the calorimeter compatible with a minimum ionising particle. The muon reconstruction efficiency for the region with $|\eta| < 0.1$ can be recovered by this type. The MS does not fully cover the region with $|\eta| < 0.1$ due to cables and services of the calorimeters and ID.

- Extrapolated (ME) muon: is the muon track in the region with $|\eta| > 2.5$ and roughly originated from interaction point. The ME muons are used to extend the muon reconstruction acceptance to region with $2.5 < |\eta| < 2.7$ which is out of the acceptance of the ID.

Overlaps between different muon types are resolved by basically setting priority to CB , ST, CT muons in order. The overlap with ME muons is resolved by selecting the track with better fit quality and larger number of hits.

4.4 Jet

When a high p_{T} gluon or quark is produced, it becomes a collimated bunch of hadrons, called a *jet*. Jets are dominant objects in high energy proton-proton collision experiments like the ones at LHC.

Jets in the ATLAS calorimeters are reconstructed mainly with the anti-k_{T} algorithm [77], which is the standard jet finding algorithm in the ATLAS. The input for the algorithm in this paper is topological calorimeter clusters (*topo-clusters*) [78, 79] with a positive

energy. The topo-clusters are built from topologically connected calorimeter cells that contain a significant energy deposit well above noise. The topo-clusters are reconstructed at the electromagnetic scale [80], i.e. calibrated to correctly measure the energy deposits from electromagnetic showers in the calorimeter.

The anti-k_{T} algorithm introduces distances $d_{i,j}$ between entities (clusters, pseudo-jets) i and j and $d_{i,B}$ between entity i and the beam axis defined as the following:

$$d_{i,j} = \min(k_{\mathrm{T}i}^{-2},\, k_{\mathrm{T}j}^{-2})\frac{\Delta R_{ij}^2}{D^2}, \tag{4.2}$$

$$d_{i,B} = k_{\mathrm{T}i}^{-2}, \tag{4.3}$$

where $\Delta R_{ij}^2 = (\eta_i - \eta_j)^2 + (\phi_i - \phi_j)^2$ and $k_{\mathrm{T}i}$, η_i and ϕ_i are respectively the transverse momentum, pseudorapidity and azimuthal angle of particle i. D is the jet-cone radius parameter which is fixed at 0.4 in the analysis of this dissertation. The clustering proceeds by identifying the smallest of the distances between $d_{i,j}$ and $d_{i,B}$. If it is a $d_{i,j}$, entities i and j are combined. On the other hand, if $d_{i,B}$ is the smallest, entity i is defined as a jet and removed from the list of entities. The distances are then recalculated and the procedure repeated until no entities are left.

4.5 Missing Transverse Momentum

The missing transverse momentum $E_{\mathrm{T}}^{\mathrm{miss}}$ is an important observable which represents the transverse momentum carried by undetectable *non-interacting* particles such as neutrinos. The missing transverse momentum in ATLAS is reconstructed from the components $p_{x(y)}$ of the transverse momentum p_{T} of the various contributions, given by

$$E_{x(y)}^{\mathrm{miss}} = -\sum_{i\in\text{hard objects}} p_{x(y),i} - \sum_{j\in\text{soft signals}} p_{x(y),j}. \tag{4.4}$$

The second term of the right hand side of Eq. (4.4) is called soft term. The set of observables is constructed from $E_{x(y)}^{\mathrm{miss}}$:

$$\boldsymbol{E}_{\mathrm{T}}^{\mathrm{miss}} = (E_x^{\mathrm{miss}},\, E_y^{\mathrm{miss}}), \tag{4.5}$$

$$E_{\mathrm{T}}^{\mathrm{miss}} = |\boldsymbol{E}_{\mathrm{T}}^{\mathrm{miss}}| = \sqrt{(E_x^{\mathrm{miss}})^2 + (E_y^{\mathrm{miss}})^2}, \tag{4.6}$$

$$\phi^{\mathrm{miss}} = \arctan(E_y^{\mathrm{miss}}/E_x^{\mathrm{miss}}). \tag{4.7}$$

In this dissertation, the $\boldsymbol{E}_{\mathrm{T}}^{\mathrm{miss}}$ is defined as the vectorial sum of missing transverse momentum terms $\boldsymbol{p}_{\mathrm{T}}^{\mathrm{miss},i}$ of hard objects, with $i \in \{e,\, \gamma,\, \mu,\, \mathrm{jet}\}$, and the corresponding soft term $\boldsymbol{p}_{\mathrm{T}}^{\mathrm{miss,soft}}$ constructed from tracks which are not associated with the hard objects. This yields

$$\boldsymbol{E}_{\mathrm{T}}^{\mathrm{miss}} = -\sum_{\text{electrons}} \boldsymbol{p}_{\mathrm{T}}^{e} - \sum_{\text{photons}} \boldsymbol{p}_{\mathrm{T}}^{\gamma} - \sum_{\text{muons}} \boldsymbol{p}_{\mathrm{T}}^{\mu} - \sum_{\text{jets}} \boldsymbol{p}_{\mathrm{T}}^{\mathrm{jet}} - \sum_{\text{unused tracks}} \boldsymbol{p}_{\mathrm{T}}^{\mathrm{track}}. \tag{4.8}$$

Object definition and procedure for overlap removal between objects found in the similar position might differ analysis-by-analysis. The particular selections for the analysis in this dissertation are presented in Section 5.5.6.

Chapter 5

The Displaced Vertex Analysis

This chapter of the thesis describes a search for a long-lived supersymmetric partner of the gluon in the data collected with the ATLAS detector in 2016 at $\sqrt{s} = 13$ TeV. Final states containing at least one massive displaced vertex with high track multiplicity and missing transverse momentum are investigated. The search strategy and the backgrounds, which dominantly originate from instrumental effects, are introduced in this chapter.

5.1 Introduction

Search for massive long-lived particles is an important part of the ATLAS programs of searches for new physics [31]. Pioneering work was done in the ATLAS experiment with pp collisions at $\sqrt{s} = 7$ TeV in 2010 [81], which focused on a signature with Displaced Vertices (DVs) associated with high-p_{T} muons, predicted in a specific R-parity violating model [82]. The same signature was investigated with the 2011 data of pp collisions at $\sqrt{s} = 7$ TeV [83] and 2012 data at $\sqrt{s} = 8$ TeV [84]. Following these searches, other signatures with displaced vertices were explored with the 2012 data, i.e., a DV associated with a high-p_{T} lepton, or in an event with several high-p_{T} jets or large missing transverse energy ($E_{\mathrm{T}}^{\mathrm{miss}}$) [32, 85], which could explore more general R-parity violating models [82], a Split SUSY model [24] and a Gauge-Mediated SUSY model [86].

In this analysis, 32.7 fb^{-1} pp collision data at $\sqrt{s} = 13$ TeV recorded in 2016 are used. The production cross section of heavy particles has significantly increased as the beam energy of the LHC has increased. In addition, a newly installed layer of the Pixel detector (IBL) has improved the performance of track and vertex reconstruction [52]. The sensitivity to new physics phenomena which result in DVs has been expected to increase thanks to these improvements.

As the first such search in Run 2 of the LHC, a signature with a DV and significant $E_{\mathrm{T}}^{\mathrm{miss}}$ is focused. This channel is sensitive to large regions of phase space in the various signal models and has the benefit that complex uncertainties related to the reconstruction of muons and electrons from displaced decays are avoided. A Split SUSY model (see Section 2.2.3) is considered here and the process of pair-production of long-lived gluinos which hadronise into R-hadrons before decaying into two quarks and neutralino, shown as Fig. 5.1, is a target of this analysis.

The previous search in Run 1 [32, 85] targeted high-mass gluinos with a fixed neutralino mass at 100 GeV, so that it was required that at least two energetic jets with $E_{\mathrm{T}} > 50$ GeV and total p_{T} of tracks associated with the jet is less than 5 GeV, called a *trackless jet* requirement. The search presented in this dissertation also targets scenarios

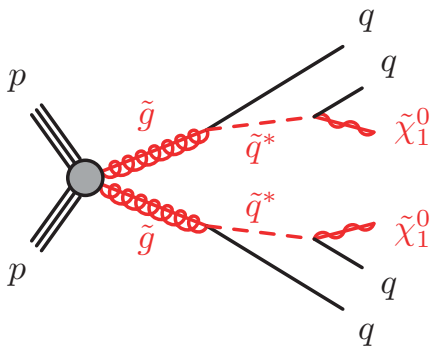

Figure 5.1: Feynman diagram representing production of long-lived gluinos in a Split SUSY model, which form *R*-hadrons and give rise to displaced decays with hadronic final states.

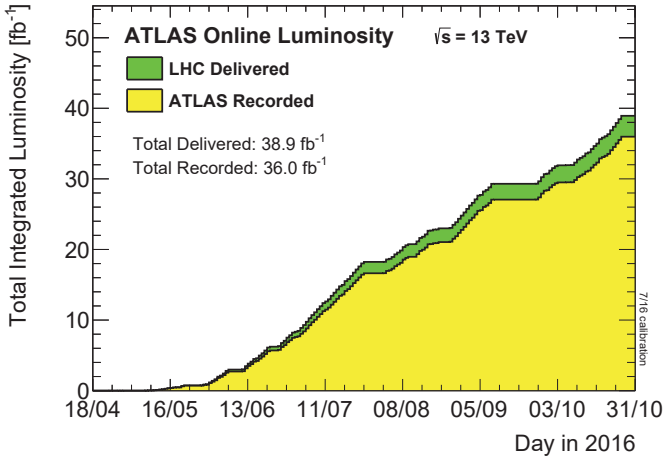

Figure 5.2: Cumulative luminosity as a function of time delivered to (green), recorded by ATLAS (yellow) during stable beams for pp collisions at 13 TeV centre-of-mass energy in 2016 [47].

in which a neutralino mass is close to a gluino mass. This mass relation would realise a so-called *gaugino co-annihilation* mechanism and thus it is favoured from the relic dark matter abundance [44] as explained in Section 2.3.1.

5.2 Dataset Information

5.2.1 Data Samples

The full dataset of ATLAS *pp* collision data at $\sqrt{s} = 13$ TeV, recorded between April and October in 2016, is used in the analysis. Figure 5.2 shows the integrated luminosity as a function of time for the dataset. In total, 36.0 fb^{-1} of data was recorded, however, a part of the recorded data is not used due to the temporal detector failure or any other defects in data taking conditions. The events recorded during a certain interval of time in such bad condition are tagged as bad events in an ATLAS database. The events which

Table 5.1: Data taking periods and the corresponding amount of the integrated luminosity for the 2016 dataset after the application of data quality requirements. Runs in period H were recorded with the beam condition of low μ for forward physics. Runs in period J were taken with $\beta^* = 2.5$ km for the measurement of elastic pp-scattering by the "Absolute Luminosity For ATLAS" (ALFA) detector.

Period	Run Numbers	Dates	Integrated Luminosity [pb^{-1}]
A	297730 - 300279	28 Apr. - 27 May.	552.7
B	300345 - 300908	27 May. - 06 Jun.	1922.6
C	301912 - 302393	11 Jun. - 21 Jun.	2861.3
D	302737 - 303560	24 Jun. - 10 Jul.	4624.2
E	303638 - 303892	10 Jul. - 16 Jul.	1481.0
F	303943 - 304494	16 Jul. - 25 Jul.	3398.9
G	305380 - 306451	02 Aug. - 17 Aug.	3818.4
H	N/A	N/A	N/A
I	307126 - 308084	25 Aug. - 10 Sep.	5760.7
J	N/A	N/A	N/A
K	309375 - 309759	26 Sep. - 03 Oct.	2191.6
L	310015 - 311481	06 Oct. - 26 Oct.	6127.5
A-L	297730 - 311481	28 Apr. - 26 Oct.	32739.0

are not regarded as bad are added to a list. This list is called a Good Runs List (GRL). According to the GRL, a total usable integrated luminosity corresponds to 32.7 fb^{-1}. The total dataset is broken down into data-taking periods, with individual integrated luminosities listed in Tab. 5.1.

As the standard ATLAS tracking algorithms are inefficient for finding tracks with impact parameters larger than 100 mm, track reconstruction has to be re-run with relaxed tracking parameters as shown in Tab. 4.2. This "re-tracking" procedure (see Section 4.1.2) requires low-level information such as hits on surfaces of the detectors. This is a time consuming process that is not allowed to be applied to the whole dataset in 2016. It is necessary to prepare the data format with low-level information but containing much less number of events. A specific event filter has been prepared to reduce events which seem not to be interesting by applying certain kinematic cuts. Each group searching for long-lived particles in ATLAS has designed a filter for its analysis. A filter used in this analysis is based mainly on $E_{\mathrm{T}}^{\mathrm{miss}}$ as later shown in Section 5.5.1. After filtering events, the remaining number of events is required to be $\mathcal{O}(1)\%$ of the original dataset. This data format is designed specifically to give access to low-level detector and reconstruction information for searches that need to do custom reconstruction or use unconventional variables based on low-level detector data.

5.2.2 Simulated Samples

The displaced vertex analysis makes use of a number of signal MC samples to determine the expected signal efficiencies and to estimate uncertainties in the efficiency. For metastable R-hadrons, pair production of gluinos with masses ($m_{\tilde{g}}$) between 400 GeV and 2000 GeV with the neutralino mass varied between 100 and $m_{\tilde{g}} - 30$ GeV is simulated in Pythia 6.4.28 [87]. The AUET2B [88] set of tuned parameters for the underlying event and the CTEQ6L1 [89] parton distribution function (PDF) set are used. The dedicated routines [90] for hadronization of heavy particles are used to simulate the

production of R-hadrons. The cross sections are calculated at next-to-leading order (NLO) assuming a squark mass of 10 TeV. The most significant contributions to the NLO QCD corrections come from soft-gluon emission off the coloured particles in the initial and final state [91]. The resummation of soft-gluon emission is taken into account at next-to-leading-logarithmic accuracy (NLO+NLL) [92–95]. The uncertainty on the cross-section predictions are defined as an envelope of cross-section predictions using different PDF sets (CTEQ6.6 [96] and MSTW2008 [97]) and factorisation and renormalisation scales, as described in Ref. [91]. The nominal cross-section is obtained using the midpoint of the envelope.

The ATLAS reconstruction simulation framework [98] using GEANT4 [99–101] is used for detector simulation. The dedicated routines based on the physics model described in Refs. [90, 102] are incorporated to emulate interactions of R-hadrons with matter. This model assumes the cross section of 12 mb per nucleon for each light valence quark. The interaction of heavy parton is neglected. A gluino would form a R-hadron with one or two quarks, or even with a single gluon [31]. In this analysis, the probability to form a gluon-gluino bound state is assumed to be 10%.

The gluinos within R-hadrons decay via the process $\tilde{g} \to qq\tilde{\chi}_1^0$ using PYTHIA 6 as illustrated in Fig. 5.1. The gluino lifetime (τ) is varied from 0.01 to 50 ns. All simulated samples include a modelling of pileup. The pileup modelling is done by adding the expected number of minimum-bias pp interactions from the same (in-time pileup) and nearby (out-of-time pileup) bunch crossings. Simulated events are reconstructed using the same software as the one used for the collision data. PYTHIA 6 can perform the simulation of R-hadrons, however it suffers from inaccuracy for radiative effects, known as initial state radiation (ISR) or final state radiation (FSR). To get a more accurate description of them, additional samples of gluinos are generated using MG5_aMCNLO [103], interfaced to the PYTHIA 8.186 [104] parton shower model, with the A14 [105] set of tuning parameters together with the NNPDF2.3LO [106] PDF set. The distribution of the transverse momentum of the gluino-gluino system simulated with PYTHIA 6 is then reweighted to match the distribution obtained in samples of MG5_aMCNLO.

5.3 Background Sources

One of the powerful features of the search for new physics via high-mass and high-track-multiplicity DVs is the extremely low level of background. However, there are three sources of background, which may produce the massive non-signal DVs with high track multiplicities as illustrated in Fig. 5.3.

- **Hadronic interactions:** Particles interacting with the detector material can produce secondary vertices, which are difficult to be distinguished from DVs arising from long-lived particle decays. These can potentially be massive and have a high track multiplicity to fall into the analysis signal region.

- **Merged vertices:** The last step in the vertexing algorithm are to merge vertices if they are within 1 mm from each other (see Section 4.1.4). Therefore, it is possible that two vertices from two different decays are merged accidentally. The merged vertex may have a high track multiplicity and large invariant mass.

- **Random Crossings:** A track, from an arbitrary source, which lies very close to the real vertex might be reconstructed as a part of the vertex. If the angle at which

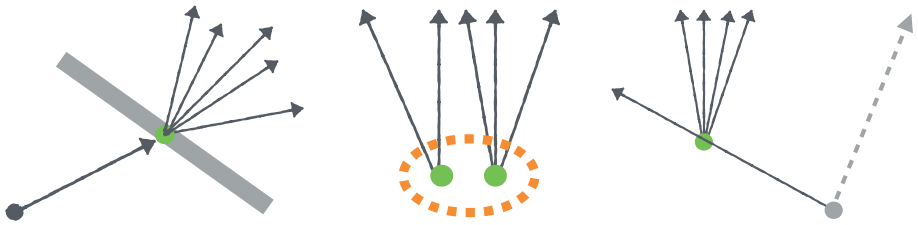

Figure 5.3: Illustrations of three sources of background which may result in massive non-signal displaced vertices with high track multiplicities. (a) shows hadronic interaction with a detector material, (b) shows a pair of vertices merged by the secondary vertexing algorithm because the distance between them is less than 1 mm and (c) shows a vertex at which an independent track randomly crosses with large opening angle.

a track crosses the vertex is large, the invariant mass of the vertex also becomes large. Thus, the number of tracks associated to the vertex as well as the invariant mass of the vertex might become large enough to be included in the signal region.

The first source of background, the hadronic interaction vertices, are significantly reduced by applying a material veto, where any vertices found in the dense material regions of the detector are removed. Further details regarding the material veto are covered in Section 5.6.4. The second source of background, merged vertices, is expected to be small. In the previous search in Run-1 [32] it was found that the contribution of this source to the total background was 0.03%, which was a factor of ten smaller than the statistical uncertainty applied to the estimation. The last source is the dominant contribution of the backgrounds. The number of expected background vertices from these sources is estimated using a fully data-driven methods and shall be explained in Section 5.7.

5.4 Overview of Signal, Control and Validation Regions

The displaced vertex search makes use of a signal region, several control regions and validation regions, all of which are defined by multiple kinematic selections. Before going into the details in Section 5.5, an overview of the regions is given to clarify their roles and the requirements.

The signal region (SR) is defined by a set of selections used to maximise the signal-to-background ratio as well as to minimise the systematic uncertainties. A final decision whether signal events exist or not is done in this region. Several control regions (CRs) are defined by sets of basic selections and are used to estimate the numbers of background vertices. The validation regions (VRs) are kinematically neighbouring regions to the SR and are used to validate the methods of background estimation.

Table 5.2 contains a summary of the requirements that define the samples of events (and vertices considered within those events) used to derive the background estimates and validate the estimation methods.

Table 5.2: Definitions of the control, validation and signal regions in the analysis. The validation and signal regions are defined by the control region requirements and some additional selections.

Control Region (CR):	
Event-level requirements:	
`DRAW_RPVLL` filter:	see description in Section 5.5.1
`DAOD_SUSY15` filter:	see description in Section 5.5.1
Event cleaning	Rejection of bad/corrupted events (LAr, Tile, TTC restart, ...)
Good Runs List	Removal of bad lumi blocks based on data quality assessment
Primary vertex	At least 1 good PV, with $N_{\mathrm{PV}}^{\mathrm{tracks}} \geq 2$ and $\lvert z_{\mathrm{PV}}\rvert < 200$ mm
Non-collision background veto	Reject events where the leading jet satisfies $f_{\mathrm{max}} > 0.8$ or $f_{\mathrm{EM}} > 0.96$
Vertex-level requirements:	
Fiducial region	$R < 300$ mm and $\lvert z\rvert < 300$ mm
Vertex fit quality	$\chi^2/\mathrm{N_{dof}} < 5$
Displacement from PV (in x–y plane)	$d_{\mathrm{T}}^{\mathrm{PV-DV}} > 4$ mm
Material veto	Not in volume marked as dominated by material
Disabled-module veto	Not in volume affected by disabled Pixel detector modules
Low-$E_{\mathrm{T}}^{\mathrm{miss}}$ Validation Region (VRLM):	(On top of CR requirements)
Additional event-level requirements:	
Upper $E_{\mathrm{T}}^{\mathrm{miss}}$ cut	Offline calibrated $E_{\mathrm{T}}^{\mathrm{miss}} < 150$ GeV
Upper $\Delta\phi_{\mathrm{min}}(E_{\mathrm{T}}^{\mathrm{miss}}, \mathrm{jets})$ cut	$\Delta\phi_{\mathrm{min}}(E_{\mathrm{T}}^{\mathrm{miss}}, \mathrm{jets}) < 0.75$, using all selected jets with $p_{\mathrm{T}} > 30$ GeV
Additional vertex-level requirements:	
Track multiplicity	$n_{\mathrm{tracks}} = 4$
Invariant mass	$m_{\mathrm{DV}} > 10$ GeV
Material Validation Region (VRM):	(On top of CR requirements, *except material veto*)
Additional vertex-level requirements:	
Material region	The vertices considered are *required* to be in volume marked as dominated by material
Track multiplicity	$n_{\mathrm{tracks}} = 4$
Invariant mass	$m_{\mathrm{DV}} > 10$ GeV
Signal Region (SR):	(On top of CR requirements)
Additional event-level requirements:	
$E_{\mathrm{T}}^{\mathrm{miss}}$ trigger	Requiring the lowest unprescaled $E_{\mathrm{T}}^{\mathrm{miss}}$ trigger to pass
$E_{\mathrm{T}}^{\mathrm{miss}}$ filter	Requiring a set of selections shown in Section 5.5.1
$E_{\mathrm{T}}^{\mathrm{miss}}$ cut	Offline calibrated $E_{\mathrm{T}}^{\mathrm{miss}} > 250$ GeV
Additional vertex-level requirements:	
Track multiplicity	$n_{\mathrm{tracks}} \geq 5$
Invariant mass	$m_{\mathrm{DV}} > 10$ GeV

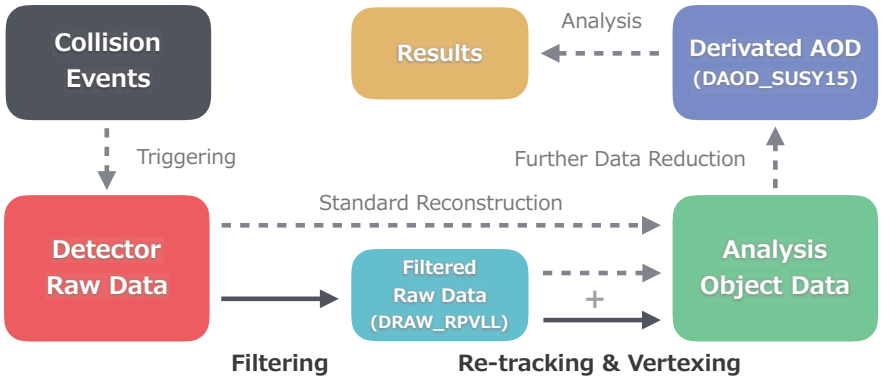

Figure 5.4: Schematic flow of data format conversion adopted in this analysis. The dashed arrows represent the standard processes in ATLAS and the solids arrows represent specific operations. `DRAW_RPVLL` and `DAOD_SUSY15` in the parentheses are names of data formats used in this analysis.

5.5 Event Selection and Cleaning

The selection of events of interest with signal characteristics is performed by applying a sequential cuts described in the following sections

5.5.1 Triggering and Filtering

Due to limitation of the storage resources, data size of recorded collision events is required to be reduced. This reduction is done in several steps as shown in Fig. 5.4. The details of each step are described in this section.

Triggering Events

Triggering events is an important first step in the event selection. The trigger controls what kinds of collision events are to be recorded. Every analysis must find appropriate triggers for its topologies at first.

For the search for meta-stable R-hadron, the trigger based on $E_{\mathrm{T}}^{\mathrm{miss}}$ is used. The triggers used for this analysis is `HLT_xe100_mht_L1_XE50` for period A-E and `HLT_xe110_mht_L1_XE50` for period F-L, which were unprescaled for the entire periods, respectively. At the High-Level Trigger (HLT) level, the *missing* H_{T} (MHT) algorithm calculates $E_{\mathrm{T}}^{\mathrm{miss}}$ as the negative vector sum of transverse energy of calibrated jets and its trigger thresholds are 100 GeV and 110 GeV of $E_{\mathrm{T}}^{\mathrm{miss}}$ (xe100 and xe110). At the L1 level, the *cell algorithm* is used instead for the entire 2016 dataset. The algorithm calculates the $E_{\mathrm{T}}^{\mathrm{miss}}$ as the negative sum of transverse energy deposited in calorimeter clusters above a certain noise threshold. The clusters are split as fixed-size trigger towers. The size of a trigger tower is 0.1×0.1 in (η, ϕ) space in the barrel region but 0.2×0.2 in the forward regions because of reduced calorimeter granularity. The trigger threshold at the L1 level is 50 GeV of $E_{\mathrm{T}}^{\mathrm{miss}}$ (XE50). The technical details of the implementation of $E_{\mathrm{T}}^{\mathrm{miss}}$ triggers at ATLAS is discussed in Ref. [107].

The $E_{\mathrm{T}}^{\mathrm{miss}}$ calculation in the online HLT is generally not the same as that in offline reconstruction. The online $E_{\mathrm{T}}^{\mathrm{miss}}$ might be calculated as smaller value than the offline one

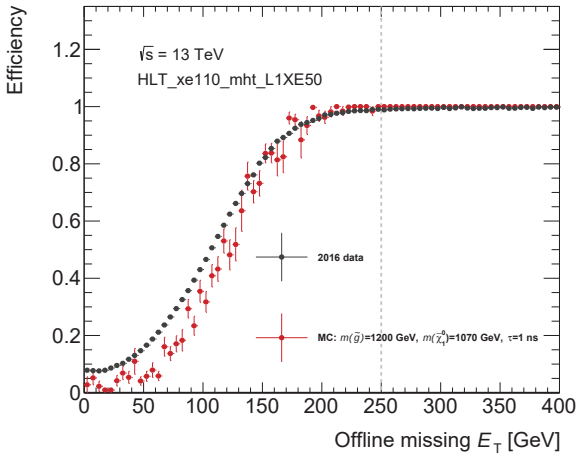

Figure 5.5: Turn-on curve of `HLT_xe110_mht_L1XE50` trigger for a certain MC signal (red) and 2016 data from Period F (black).

due to the resolution. Events with the $E_{\mathrm{T}}^{\mathrm{miss}}$ around the trigger threshold are sometimes not recorded. Figure 5.5 shows the so-called *turn-on curve* of `HLT_xe110_mht_L1_XE50`. The turn-on curve was derived using data samples recored with jets triggers. The curve was created by dividing the offline $E_{\mathrm{T}}^{\mathrm{miss}}$ distribution of sampled events which passed the $E_{\mathrm{T}}^{\mathrm{miss}}$ trigger by that of all sampled events. The triggering efficiency reaches 100% at the offline $E_{\mathrm{T}}^{\mathrm{miss}}$ of approximately 200 GeV. The offline $E_{\mathrm{T}}^{\mathrm{miss}}$ threshold is set at 250 GeV to ignore the disagreement of the turn-on curve between data and MC in low-$E_{\mathrm{T}}^{\mathrm{miss}}$ region (see also Section 5.5.6).

DRAW Filtering

This analysis needs to do custom reconstruction and use unconventional variables based on low-level detector data. The specific data format used is designed to give access to low-level detector and reconstruction information.

In order to minimise the disk space used by this format, only a small subset of events are made available. To select them, tight trigger and offline selections are applied to "skim" the data, while retaining the full RAW contents for the selected events. The filters for the 2016 `DRAW_RPVLL` dataset related to this search require at least one of the following triggers as a base selection:

- `HLT_xeXX_L1XEYY`
- `HLT_xeXX_tc_lcw_L1XEYY`
- `HLT_xeXX_topoclPS_L1XEYY`
- `HLT_xeXX_topoclPUC_L1XEYY`
- `HLT_xeXX_mht_L1XEYY`

where `XX` = 90, 100, 110, 120, 130 and `YY` = 50, 55, 60. The following online algorithms are used for the above triggers: a 2-sided 2-sigma noise suppression cell-based algorithm,

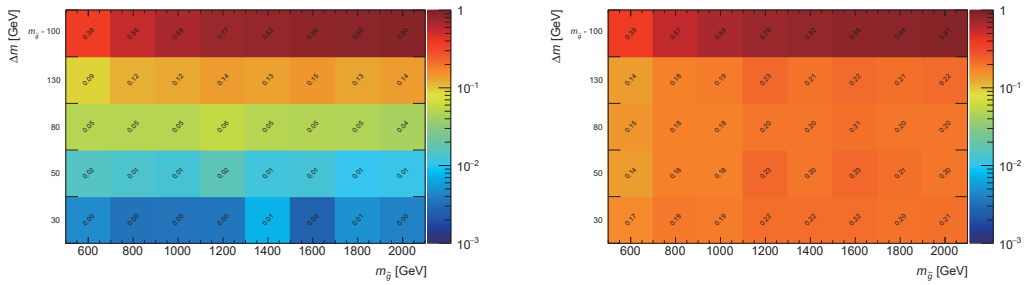

(a) With trackless jets requirement

(b) Without trackless jets requiment

Figure 5.6: Efficiencies of filter and offline calibrated $E_{\mathrm{T}}^{\mathrm{miss}}$ cut at 250 GeV for MC samples of R-hadrons (a) with trackless jets requirement and (b) without trackless jets requirement but the topocluster-based $E_{\mathrm{T}}^{\mathrm{miss}}$ threshold is raised to 180 GeV. The vertical axis shows the mass difference between gluino and the lightest neutralino and the horizontal axis shows gluino mass. In case of $\Delta m = M_{\tilde{g}} - 100$ GeV, the lightest neutralino mass is fixed at 100 GeV. It is shown that the efficiencies for small Δm scenarios are significantly improved by removing trackless jets requirement.

a topocluster-based algorithm in local calibration weighted scale with no further corrections (tc_lcw), an eta-ring pile-up subtraction (topoclPS), or a pile-up fit procedure (topoclPUC), and an algorithm based on the sum of jet momenta (mht), respectively [108]. On top of the trigger selection, some offline selections were applied depending on the data taking period. The topocluster-based $E_{\mathrm{T}}^{\mathrm{miss}}$ is required to be large. The use of topocluster-based $E_{\mathrm{T}}^{\mathrm{miss}}$ is motivated because it is a simpler value that will not change throughout data-taking. The difficulty in the previous analysis [32] was that the skim used a cut on one version of the calibrated $E_{\mathrm{T}}^{\mathrm{miss}}$. The calibration is periodically improved, therefore it was out of sync with the recommended analysis-level $E_{\mathrm{T}}^{\mathrm{miss}}$ by the time the analysis was completed. The existence of jets which are not associated with ID tracks was also required in periods A-J in 2016. Such jets are typically called *trackless jets*. The trackless jet was used in the analyses of the LHC Run 1 (-2012) as well, where the targeted scenarios predicted significant hadronic activity. This search also targets scenarios with small mass differences between the long-lived particle and the LSP (see Section 5.1). Such signatures do not provide displaced jets with enough energy to fulfil the trackless jet requirements. For this reason, the filter for the displaced vertex searches was changed during the year to use a simple but tighter requirement on topocluster-based $E_{\mathrm{T}}^{\mathrm{miss}}$ instead. This is justified by the increased signal efficiencies for the compressed signal scenarios shown in Fig. 5.6. In summary, the following offline criteria were applied depending on the data taking periods:

Periods A-J: topocluster-based $E_{\mathrm{T}}^{\mathrm{miss}} > 130$ GeV `AND` any of the following requirements:
at least one jet with $p_{\mathrm{T}} > 70$ GeV with `SumPtTrk` < 5 GeV,
at least two jets with $p_{\mathrm{T}} > 25$ GeV with `SumPtTrk` < 5 GeV,
where `SumPtTrk` $= \sum p_{\mathrm{T}}$ of tracks from the PV
(with $p_{\mathrm{T}} > 0.5$ GeV) associated to the jet

Periods K-L: topocluster-based $E_{\mathrm{T}}^{\mathrm{miss}} > 180$ GeV

The `SumPtTrk` requirement was used to select trackless jets.

Further Skimming and Corrections

The analysis data samples contain not only events passing the triggers and filter used in this analysis but also those which passed other triggers, such as jet or lepton triggers, and other filters prepared for other analyses. For further data size reduction and corrections, a proper derivation [109], `DAOD_SUSY15`, is applied to the filtered dataset. This skims the data sample by selecting the events passing any of a set of triggers defined within the ATLAS long-lived searches groups. This list includes the lowest-threshold unprescaled $E_{\mathrm{T}}^{\mathrm{miss}}$ triggers used by this analysis. This is used only for data and no skimming is applied to MC samples.

5.5.2 Good Runs List

As described in Section 5.2.1, data quality (DQ) information assessed by the DQ group is summarised in Good Runs List (GRL). In the GRL, flags of "good" or "bad" are assigned to each luminosity block in each run [110]. A luminosity block is the unit of time for data-taking, and lasts about one minute. For instance, if more than 30% of the modules in a Pixel layer is disabled for some reason in a certain luminosity block, an intolerable defect flag is assigned to the block. The GRL is used to justify that the dataset used in the analysis are in good condition. Approximately the GRL discards 3% out of the whole events passing the above selections.

5.5.3 Event Cleaning

The GRL provides the data quality information in the unit of luminosity blocks. Events in bad condition are sometimes not vetoed if the luminosity blocks pass the data quality requirements. Events that contains the following problems are further vetoed:

1. LAr noise bursts and/or data corruption
2. corruption of the Tile data
3. non-operational cells in the Tile and Hadronic End Cap (HEC) calorimeters
4. the recovery procedure for single event upsets in the SCT

5.5.4 Primary Vertex

In order to suppress effects on the $E_{\mathrm{T}}^{\mathrm{miss}}$ calculation from pile up collisions, the Primary Vertex (PV) is required to be indentified. The events are required to contain at least one good PV with at least two tracks, and z position $|z_{\mathrm{PV}}| < 200$ mm. When several such vertices are available, the one with the largest $\Sigma(p_{\mathrm{T}}^{\mathrm{trk}})^2$ is chosen as the selected PV.

5.5.5 Non Collision Background Veto

When the large $E_{\mathrm{T}}^{\mathrm{miss}}$ cut is applied, contribution from non-collision background (NCB) processes becomes significant. At the LHC, one of the main sources of NCB which comes into the detector is so-called *tertiary halo* [111]. Tertiary halo is a bunch of protons that escape the beam cleaning system and are scattered by the tertiary collimator (TCT) positioned at $|z| \approx 150$ m from the interaction point. Figure 5.7 shows a schematic illustration of the LHC beam cleaning system and how tertiary halo is produced. Particles which are produced by interaction between the tertiary halo and the TCT are generally

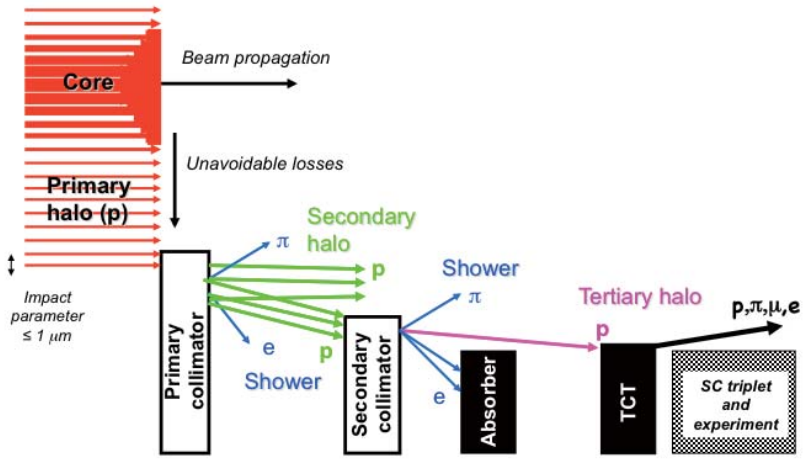

Figure 5.7: Schematic illustration of the LHC cleaning system. Primary and secondary collimators and absorbers in the cleaning insertions remove most of the halo. Some tertiary halo escapes and is intercepted close to the experiments by the TCT [111].

blocked by the shielding material, however high energy muons likely penetrate the shield and leave large energy in the calorimeters via radiative energy losses. Such energy deposit is reconstructed as a jet. Figure 5.8 shows the x–y position distribution of the CSC muon track segments in an endcap region. The two clear peaks at $\phi = 0$, $\pm\pi$ are corresponding to a horizontal spread of the NCB, most likely due to bending in the dipole magnets. Figure 5.9 shows the azimuthal $E_{\mathrm{T}}^{\mathrm{miss}}$ angle distributions. The plot on the left hand side is for three different selections on the dataset: all events passing the filtering and skimming (black), all events passing the event-level selection including the $E_{\mathrm{T}}^{\mathrm{miss}} > 250$ GeV cut (blue), and after also requiring a good DV passing all vertex selections except for the n_{tracks} and m_{DV} cuts (red). On the right hand side, this red distribution is split up for periods A-J and K-L showing that both periods are significantly contaminated, i.e. both of the two filters that were used for the processing of the data for the two periods select non-collision background events.

The event selection does not require any hard physics object associated to the PV, and this means the search is more sensitive to contamination of non-collision background events. The distribution of energy deposits by the jet, the shower shape and its direction can be employed to discriminate collision jets from NCB-induced fake jets. Studying many of the variables commonly used for jet cleaning, a few variables have been found to have efficient discriminating power between the events in the peaks around $\phi = 0$ and $\phi = \pm\pi$ from non-collision background processes and the events not contaminated by non-collision processes. In particular, when it is required that the leading jet has small value of the maximum jet energy fraction in any single calorimeter layer (f_{max}), the peaks are dramatically reduced for one significantly affected run as shown in Fig. 5.10.

It is also found that non-collision background has a large electromagnetic energy fraction (f_{EM}), defined as the ratio of the energy deposited in the electromagnetic (EM) calorimeter to the total energy. This analysis vetoes events where the leading jet satisfies either of these criteria:

- $f_{\mathrm{max}} > 0.8$

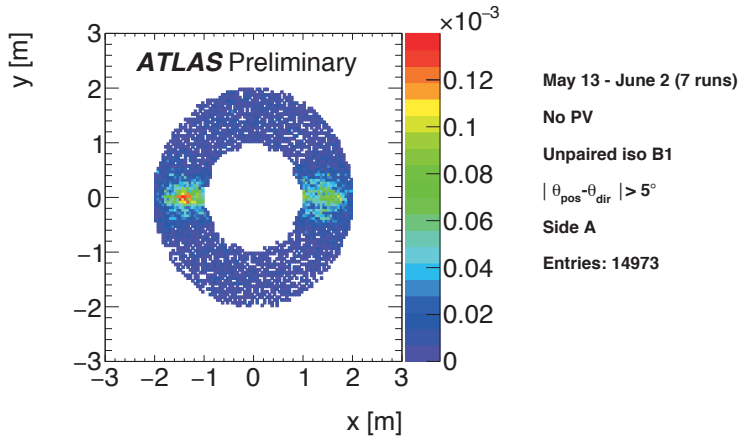

Figure 5.8: Distribution in the plane transverse to the beam pipe of the CSC muon segments in EndCap A, in runs from May 13 to June 2nd in 2016, in events from unpaired isolated bunches, without any primary vertex and passing a trigger requiring a jet with $p_{\mathrm{T}} > 12$ GeV [112]. A cut on the difference between the polar position and the polar direction of the muon segment is applied. The distributions for each run are normalised by the duration of the run in seconds, and the plot represents the average over all the runs.

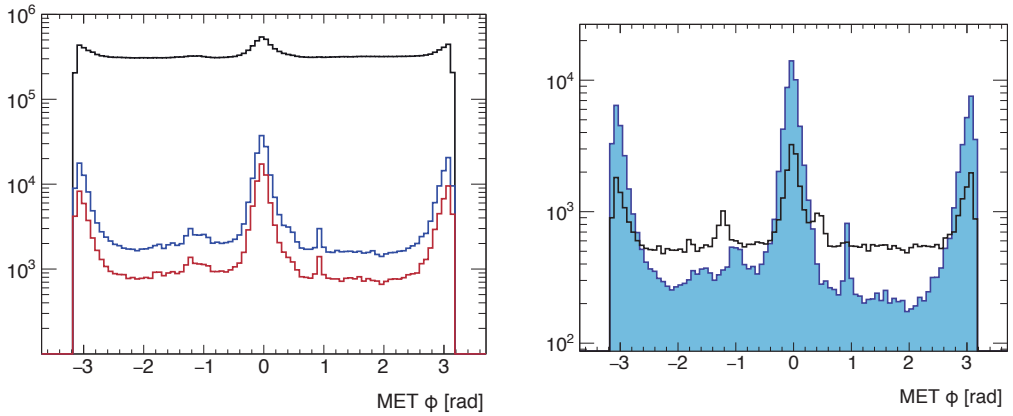

Figure 5.9: Distributions of the ϕ of the $E_{\mathrm{T}}^{\mathrm{miss}}$ for the data. Left: all events passing the DRAW+SUSY15 selection (black), all events passing the event-level selection including the $E_{\mathrm{T}}^{\mathrm{miss}} > 250$ GeV cut (blue), and after also requiring a good DV passing all but the n_{tracks} and m_{DV} cuts (red). Right: the events passing the last selection on the left but separated for periods A-J (blue) and K-L (black).

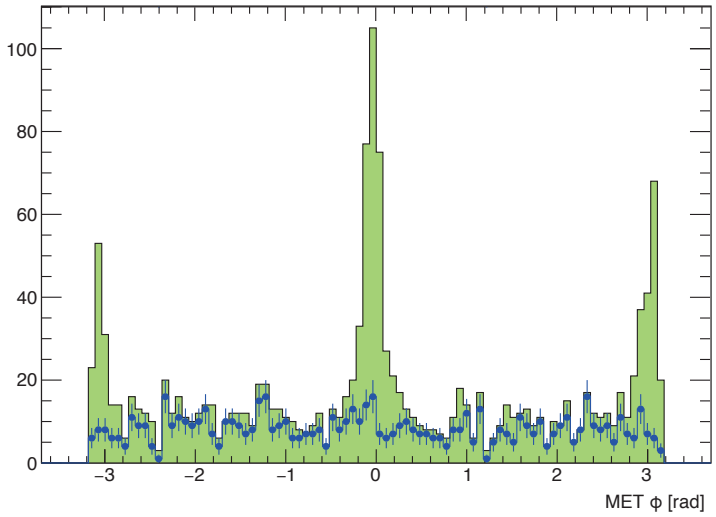

Figure 5.10: The ϕ distribution of the $E_{\mathrm{T}}^{\mathrm{miss}}$ for one run significantly contaminated by non-collision background before (green histogram) and after (blue markers) requiring $f_{\mathrm{max}} < 0.7$ for the leading jet.

- $f_{\mathrm{EM}} > 0.96$

Figure 5.11 shows the two-dimensional distributions for these variables for data (a) and an example signal MC sample (b). In summary, studies on a subset of the data and a representative set of signal MC samples indicate that the cuts above reject 90% of the data in the ϕ peaks (i.e. almost all NCB) while rejecting $< 1\%$ of the signal events.

Figure 5.12 shows the azimuthal $E_{\mathrm{T}}^{\mathrm{miss}}$ angle for events before and after the NCB veto described above. This is shown with and without an additional requirement the events have a DV with at least 3 tracks, showing that the final contribution of NCB on the analysis is significantly reduced after the explicit veto.

5.5.6 Offline Missing Transverse Energy Cut

The displaced vertex analysis does not explicitly use electrons, photons and muons, however these objects are necessary for the $E_{\mathrm{T}}^{\mathrm{miss}}$ calculation. The object definitions and the strategy to solve overlap between them are described in this section.

Electron and Photon definition

An electron and a photon are reconstructed as clusters of energies in the electromagnetic calorimeter and distinguished from each other by checking how many tracks match the cluster as described in Section 4.2. The electron is further required to pass the standard loose quality requirements, named as *LooseAndBLayerLLH* [113]. On the other hand, the photon is required to pass the standard *tight photon* identification criteria [114]. The tight requirements are chosen for photons because (unconverted) photons are reconstructed using only calorimeter information unlike electrons. The electron identification algorithm is the likelihood-based (LH) methods. It is a multivariate analysis (MVA) technique which deals with the signal and background probability density functions (PDFs) of the several discriminating variables simultaneously. On the other hand, the photon

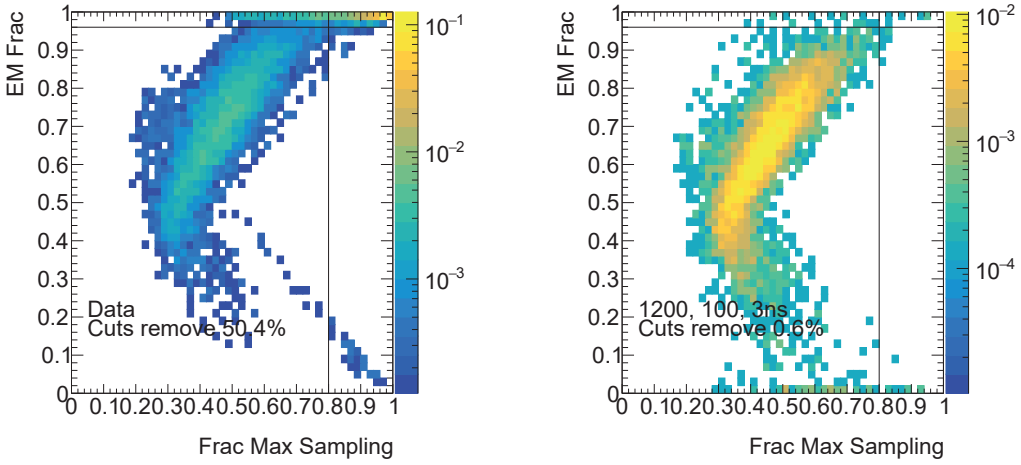

(a) (b)

Figure 5.11: Two-dimensional distributions for the two variables proposed to use for the NCB veto, for (a) data and (b) an example signal MC sample.

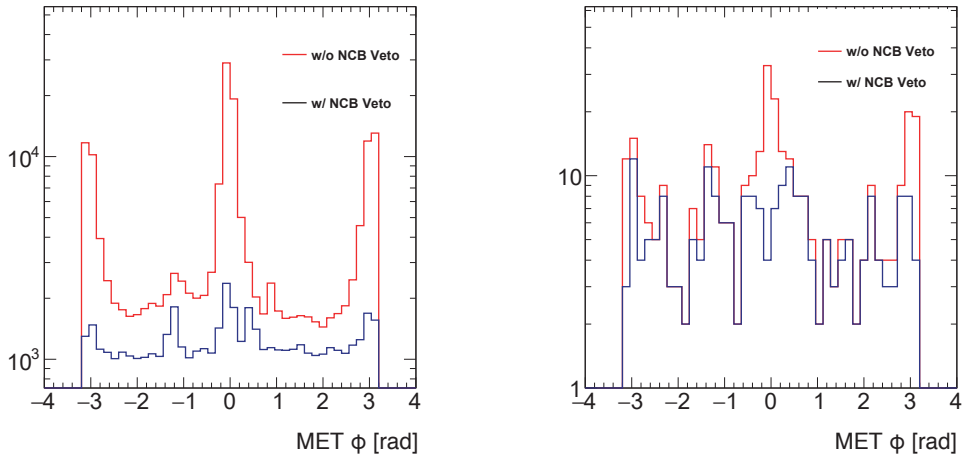

(a) (b)

Figure 5.12: The $E_{\mathrm{T}}^{\mathrm{miss}}$ ϕ distributions (a) for events passing the event-level selection with and without the NCB veto described in the text and (b) the same selection but also requiring the presence of a vertex with at least three tracks.

identification method is based on independent cut-based selection on the several discriminating variables.

In addition, the electron is required to have the transverse momentum of $p_{\mathrm{T}} > 10$ GeV and to be within the pseudo-rapidity range of $|\eta| < 2.47$. The photon p_{T} is required to be greater than 25 GeV and be within $|\eta| < 2.37$. The object is defined as bad and to be removed if its cluster is affected by the presence of a dead readout board in the first or second layer of the EM calorimeter or by the presence of a dead high voltage power supply (HV) region affecting the three layers or by the presence of a masked cell in the core of the cluster.

Muon definition

Muons are reconstructed in the inner detector and muon spectrometers independently and then combined as shown in Section 4.3. In the analysis stage, the muon is required to pass the *medium* muon identification criteria [115]. Although there are four options of the combined muon reconstruction, CB, ST, CT and ME (see Section 4.3), only CB and ME tracks are used. The CB muons are required to have at least 3 hits in at least two MDT layers, except for muons in the $|\eta| < 0.1$ where the detector coverage is not full. In this region, tracks are required to have measurements on at least one MDT layer and at most one MDT layer which does not have hits although a track is drawn on it. The ME muons are required to have measurements on at least three MDT or CSC layers. Further requirements are summarised in Ref. [115]. The kinematical selections are also applied on the transverse momentum of $p_{\mathrm{T}} > 10$ GeV and the pseudo-rapidity of $|\eta| < 2.7$.

Jet definition

The jets in this analysis are built with the anti-k_t algorithm using topological cluster calibrated in the EM scale as inputs with a distance parameter of $R = 0.4$ as described in Section 4.4. The full jet calibration scheme is applied to realise that the mean of the distribution for the ratio of the reconstructed jet energy to the truth jet energy is approximately 1 in the wide η range. The jet calibration is generally called Jet Energy Scale (JES). The `Moriond2017` release[1] of the JES calibration is used in this analysis. The jet is also required to have the transverse momentum of $p_{\mathrm{T}} > 20$ GeV and be within the pseudo-rapidity range of $|\eta| < 2.8$.

Overlap Removals

Since both electrons and jets are reconstructed as clusters in the calorimeters, a cluster is sometimes identified as an electron and a jet at the same time. Also, a muon as a decay product of a hadron in a jet is not supposed to be identified as a muon. Such "overlap" must be resolved. The overlap removal strategy is described below.

Overlap removal between jets and leptons:

1. First apply the jet-electron overlap removal using baseline, non isolated, electrons:
    - If ΔR(jet, electron) < 0.2, the jet is removed and the electron is kept.

[1] *The Rencontres de Moriond* is a series of one of the largest conferences in the high energy physics community. A recommended set of calibrations and accompanying uncertainties was prepared for analyses toward the `Moriond2017` conference by the ATLAS combined performance groups.

2. Then apply the second jet-electron and jet-muon overlap removal using the remaining jets:

    - If ΔR(jet, electron) < 0.4, the electron is removed and the jet is kept.
    - If ΔR(jet, muon) < 0.4, the muon is removed and the jet is kept unless the jet has less than 3 tracks with $p_{\mathrm{T}} > 500$ GeV, in which case the jet is removed and the muon is kept instead.

Overlap removal between photons, jets electrons and muons:

- If ΔR(photon, electron) < 0.4, the photon is removed and the electron is kept.
- If ΔR(photon, muon) < 0.4, the photon is removed and the muon is kept.
- If ΔR(photon, jet) < 0.4, the jet is removed and the photon is kept.

$E_{\mathrm{T}}^{\mathrm{miss}}$ calculation

Using the objects after resolving overlaps, the $E_{\mathrm{T}}^{\mathrm{miss}}$ is calculated as the momentum balance of them with Eq. (4.8). In this analysis, the threshold of the offline calibrated $E_{\mathrm{T}}^{\mathrm{miss}}$ is determined as the starting point of plateau of turn-on curve of combination of the $E_{\mathrm{T}}^{\mathrm{miss}}$ trigger and the topocluster-based $E_{\mathrm{T}}^{\mathrm{miss}}$ cut which are required in the pre-selection (see Section 5.5.1). Figure 5.13(a) shows the turn-on curve of the topocluster-based $E_{\mathrm{T}}^{\mathrm{miss}}$ (`MET_LocHadTopo`) with respect to the offline calibrated $E_{\mathrm{T}}^{\mathrm{miss}}$. The turn-on curve was derived using data samples recored with jets triggers. The curve was created by dividing the offline $E_{\mathrm{T}}^{\mathrm{miss}}$ distribution of sampled events which passed the topocluster-based $E_{\mathrm{T}}^{\mathrm{miss}}$ cut by that of all sampled events. The topocluster-based $E_{\mathrm{T}}^{\mathrm{miss}}$ threshold in the filter is 130 GeV during period A-J and 180 GeV during period K-L, respectively. The turn-on curve of the topocluster-based $E_{\mathrm{T}}^{\mathrm{miss}} > 180$ GeV cut reaches plateau at approximately the offline calibrated $E_{\mathrm{T}}^{\mathrm{miss}}$ of 250 GeV. Figure 5.13(b) shows the turn-on curve of efficiency for events passing the `HLT_xe110_mht_L1XE50` trigger and topocluster-based $E_{\mathrm{T}}^{\mathrm{miss}} > 180$ GeV cut for some MC signal and 2016 data of period F. In order to reduce systematic uncertainty regarding the turn-on curve, the threshold of the offline $E_{\mathrm{T}}^{\mathrm{miss}}$ is set at 250 GeV, corresponding to the starting point of the plateau region.

5.6 Vertex Selection

This section is devoted to give descriptions on vertex selections for reducing background-like vertices. The displaced vertex reconstruction itself is described in Section 4.1.4.

5.6.1 Fiducial Volume

The vertex position should be in the fiducial volume defined as the region with $r_{\mathrm{DV}} <$ 300 mm and $|z_{\mathrm{DV}}| < 300$ mm. This volume is roughly corresponding to the region inside the first barrel layer of the SCT and within the coverage of the first barrel layer of the Pixel (IBL). The SCT first layer is located around $r = 299$ mm and the z edge of the IBL is at $z = 331.5$ mm as shown in Fig. 3.5.

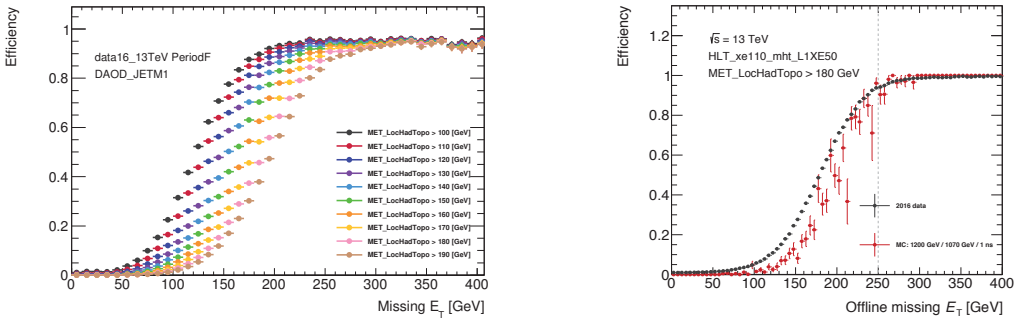

(a) (b)

Figure 5.13: (a) Turn-on curve of the topocluster-based $E_{\mathrm{T}}^{\mathrm{miss}}$ (`MET_LocHadTopo`) cut. (b) Turn-on curve of efficiency for events passing the `xe110` 2016 triggers and `MET_LocHadTopo` $>$ 180 GeV cut in a MC signal and 2016 data of Period F.

5.6.2 DV Displacement

The vertex should be separated by at least 4 mm in the x–y plane from all reconstructed primary vertices in the event. This cut is required to reduce DVs from decay of the Standard Model particles, such as B hadrons or τ leptons. For instance, the proper decay length of B^+ meson in x–y plane is approximately 4 mm if its transverse momentum is 50 GeV.

5.6.3 Vertex Fit Quality

In order to reduce the vertices with bad fitting quality, the upper limit on the reduced χ^2 of the fitting is set at 5.

5.6.4 Material Veto

Nuclear interactions with the material in the inner detector are the largest source of background vertices with high track multiplicities. Distinguishing this type of background vertices from displaced decays of long-lived particles is challenging. Any vertices found in the volume of the detector occupied by dense material therefore needs to be vetoed. A scheme to perform the veto is to construct a simplified map of these detector regions. In the previous DV search in 2012 [32] a three dimensional map was constructed and used as a map to veto material interaction vertices. The map covers the whole fiducial volume of $r < 300$ mm, $|z| < 300$ mm and in the full 2π in ϕ direction.

There are two methods used in the construction of the different parts of the map. The more complex structures of e.g. the pixel modules are extracted from vertices reconstructed in minimum bias data, whilst geometrical approximations are made for the more uniform shapes such as support rings. Figures 5.14(a) and 5.14(b) show two-dimensional maps of the number of vertices which are located in the material region, projected in the x–y plane and r–z plane, respectively.

The material veto must account for the slight movement of the detector due to its weight when approximating the position of the beam pipe, for instance. The position of these approximations have then been validated in the 2016 dataset to ensure their posi-

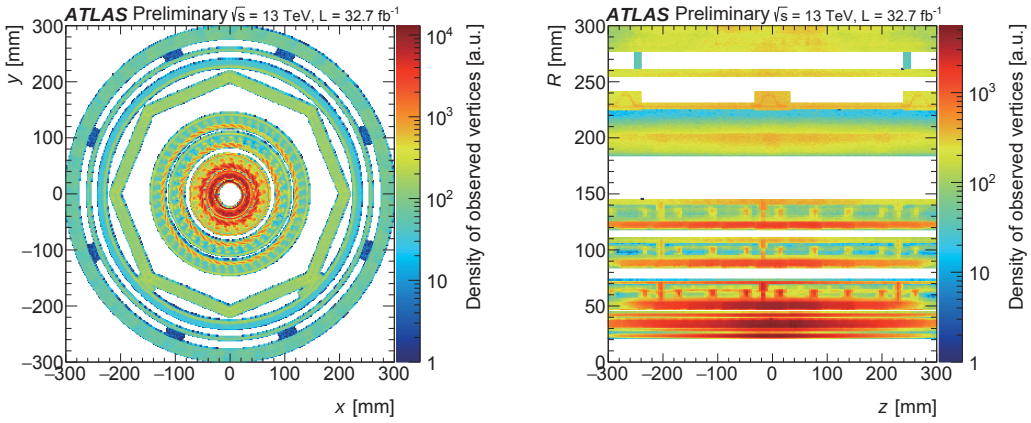

(a) (b)

Figure 5.14: Validation of the new material map. Two-dimensional maps of the number of vertices which do not pass the material veto, projected in the (a) x–y plane and (b) r–z plane.

Table 5.3: Approximations of uniform shapes augmented by the offsets created by the decoupling of the beam pipe from the ATLAS cavern.

Material layer	Radius	Thickness	x offset	y offset
Beam pipe	24 mm	3 mm	0 mm	−1.5 mm
Pixel support 1	29 mm	1.6 mm	−0.3 mm	−0.5 mm
Pixel support 2	42.5 mm	2.4 mm	−0.2 mm	−1 mm
Pixel support 3	68.5 mm	4.5 mm	−0.1 mm	−0.5 mm

tions are appropriate for the analysis described in this dissertation. The exact positions of the geometry augmented by this effect can be found in Tab. 5.3.

It should be noted that the material map is not perfect. Even if it were, there would be a chance that vertices arising from hadronic interactions with material in a vetoed region could be reconstructed in the wrong location and survive the veto. However, as a cut, it is effective in drastically reducing high-track-multiplicity background vertices arising from hadronic interaction. Contribution from vertices that were not vetoed correctly is quantified in the background estimation described in Section 5.7. Figures 5.15(a) and 5.15(b) show two-dimensional maps of the number of vertices in the 2016 data before material veto and after veto, respectively.

The volume vetoed by the material map is 42% of our fiducial volume ($\pi r^2 z \simeq 3.14 \cdot 30^2 \cdot 60$ cm^3) in total.

5.6.5 Disabled Module Veto

The functionality of fake vertex veto described in Section 4.1.4 is efficient to remove vertices constructed from randomly crossing tracks. As shown in Fig. 4.6, tracks associated with a vertex are required to have hits on the next layer. However, if a module on the layer becomes disabled in the middle of data taking, the module does not have hits and thus the vertex gets vetoed by the scheme as shown in Fig. 5.16(a). Because of this, regions directly in front of pixel modules that have been disabled for any portion

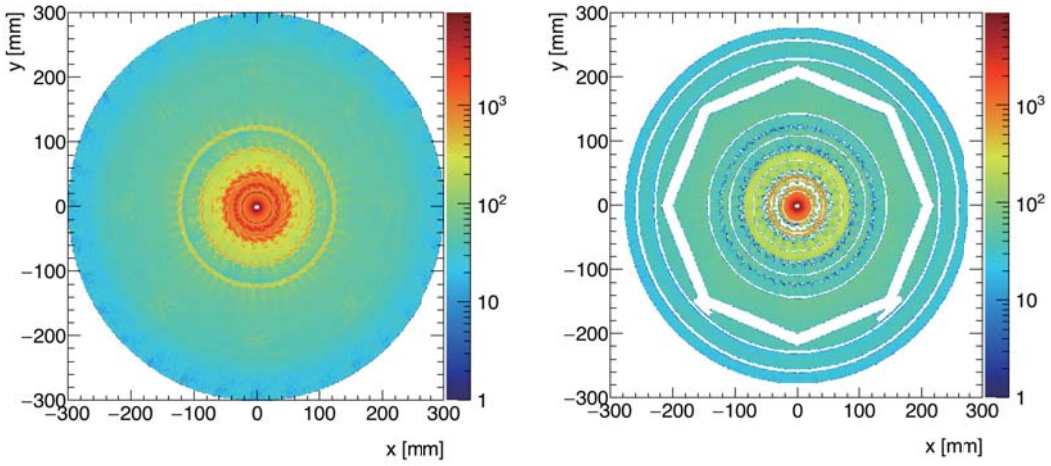

(a) (b)

Figure 5.15: Two-dimensional maps of the number of vertices in the 2016 DAOD_SUSY15 data (a) before material veto and (b) after veto. The number of vertices significantly is reduced thanks to the veto in regions where detector materials are placed.

of the 2016 dataset are explicitly vetoed in order to properly account for this effect in any simulation used. This conservative treatment should mitigate the problem at the price of only a few percent reduced overall signal acceptance. The overall volume vetoed by this procedure is $3,960$ cm^3 out of a total fiducial volume of $169,645$ cm^3, effectively vetoing 2.3% of the total fiducial volume. Figure 5.16(b) shows two-dimensional x–y map of the number of vertices sliced in z direction after applying the disabled module veto. Although some inefficient regions are still not vetoed, this can be explained by the presence of inefficient modules. Some modules which contain dead readout chips are inefficient in detection of charged particles.

5.6.6 Number of Tracks and DV Mass

The Signal Region for vertex candidates is then defined as $N_{\text{trk}} \geq 5$ and $m_{\text{DV}} > 10$ GeV, where m_{DV} is the invariant mass of the vertex calculated using the charged pion mass hypothesis for the tracks, i.e. instead of assuming massless tracks when calculating the invariant mass of the combination, it is assumed that all tracks have the mass of a charged pion. The vertex samples with $N_{\text{trk}} < 5$ and/or $m_{\text{DV}} < 10$ GeV are used for estimation of background DVs and validation of the estimation method.

5.7 Background Estimation

After the selections of events and vertices described in the previous section, the number of DVs from the Standard Model particles in the signal region becomes negligible. However there are still small contributions from experimental effects to the background as shown in Section 5.3. The methods to estimate background and the results are given in this section.

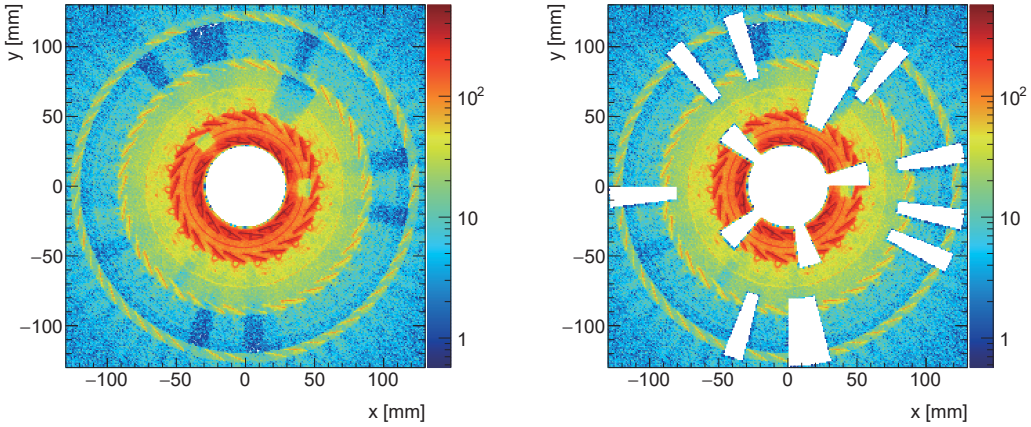

(a) (b)

Figure 5.16: (a) Two-dimensional map of the number of vertices within the region of $|z_{\mathrm{DV}}| < 20$ mm and $r_{\mathrm{DV}} > 30$ mm in x–y plane. (b) The same map as (a) but the disabled module veto is applied. The presence of inefficient modules explains some inefficient regions where are not vetoed.

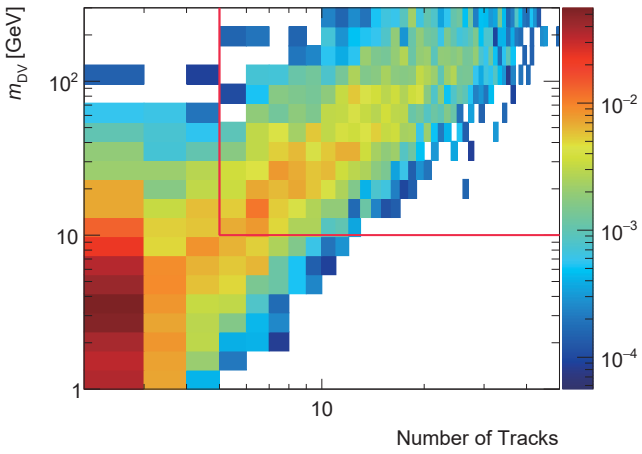

Figure 5.17: The normalised two-dimensional distribution of m_{DV} and track multiplicity for DVs in events that pass all signal region event selection criteria for signal MC with the gluino mass of 2000 GeV, the neutralino mass of 100 GeV and the gluino lifetime of 1ns. The red lines represent the boundary of the signal region requirements.

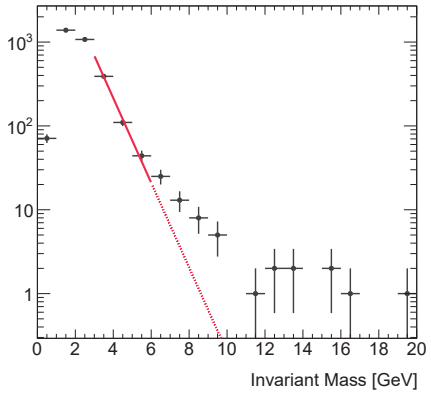

(a) 4-track DVs

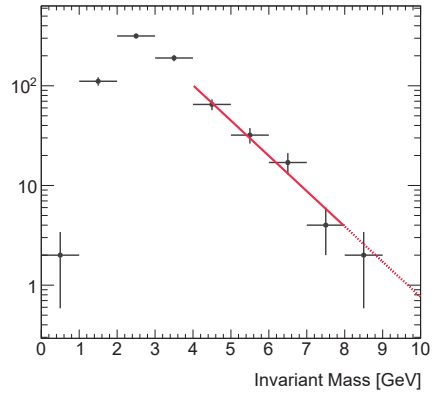

(b) 5-track DVs

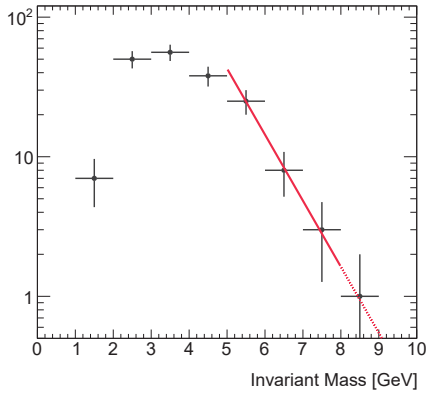

(c) 6-track DVs

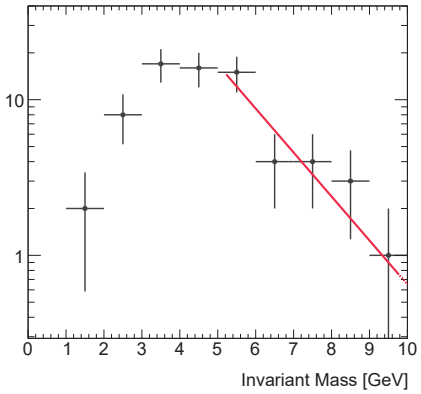

(d) ≥7-track DVs

Figure 5.18: The invariant mass distributions of vertices with more than 3 tracks after basic vertex selections. Red solid lines are fitted exponential functions and Red dashed lines are extrapolation of them.

5.7.1 Hadronic Interaction

The huge number of vertices originated from hadronic interactions is significantly reduced thanks to the material veto applied using the data-driven material map. However, the material map does not perfectly describe detector materials and there is a non-negligible possibility to hadronically interact with gaseous particles. A tiny fraction of them could leak into the signal region accidentally. The number of such vertices is estimated by taking advantage of the fact that the low mass peak in the invariant mass distribution is dominated by vertices from hadronic interaction; whereas the high mass tail is dominated by vertices with random crossing track. Figure 5.18 shows the invariant mass distributions of vertices with more than 3 tracks after the CR selections (see Tab. 5.2). A simple exponential function is used to fit the tail of the low mass peak in the DV-mass distribution, and then is extrapolated to the high mass region, i.e. $m_{\mathrm{DV}} > 10$ GeV. Appendix A confirms and quantifies the validity of the exponential assumption in this analysis by using a material rich selection. The fitted functions are $\exp(9.7 \pm 0.3 - (1.1 \pm 0.1) \cdot m)$ for 4-track DVs, $\exp(7.9 \pm 0.5 - 0.8 \pm 0.1) \cdot m)$ for 5-track DVs, $\exp(9.2 \pm 1.3 - (1.1 \pm 0.2) \cdot m)$ for 6-track DVs and $\exp(6.1 \pm 1.4 - (0.7 \pm 0.3) \cdot m)$ for $\geq$ 7-track DVs, where the uncertainties are fitting errors. The estimated number of hadronic interaction vertices with

$m_{\mathrm{DV}} > 10$ GeV is 0.3 ± 0.10 for 4-track DVs, 0.93 ± 0.56 for 5-track DVs, 0.18 ± 0.2 for 6-track DVs and 1.0 ± 1.3 for ≥ 7-track DVs, where the uncertainties are fitting errors. Note that these estimations should be scaled by the event-base scale factor described in Section 5.8.1, given that the sample is selected using the CR selection summarised in Tab. 5.2.

5.7.2 Merged Vertices

Inside the beam pipe, the vacuum is good and no hadronic interactions are expected. However due to the high-track density, there is a probability that two or more tracks cross each other and get reconstructed as a displaced vertex. Additionally close-lying meta-stable-standard-model particles such as B-hadrons can give rise to vertices, typically with masses of a few GeV at maximum (though these are almost all removed by the combination of the $|d_0| > 2$ mm cut and the requirement that the DV should be at least 4 mm from the PV in the transverse plane). Due to the high density at small r_{DV}, it is conceivable that two vertices could get merged into a single vertex with a significantly higher mass that could pass the signal region requirements. The estimation of this possibility is described in this section.

Vertex-pair distance method

The "vertex-pair distance method" [32] exploits the fact that the final step of our vertexing algorithm merges pairs of vertices separated by less than 1 mm (see Section 4.1.4). A random combination of 4 tracks can be viewed as two randomly merged 2-track combinations, and similarly for 5-track vertices and more. A pair of vertices within 1 mm is merged by the secondary vertexing algorithm, and thus a model of vertex pair distance is constructed to see how often the vertex pairs are separated by less than 1 mm. The models used in this method are distributions of the separation distance between pairs of two-track vertices, or between two-track and three-track vertices in different events. In order to normalise this model, the separation distance between vertex pairs in the same event is used. The idea is to use the bin (distance < 1 mm) of the model to estimate the background. (This bin will always be empty in the "same event" distance distribution, because any vertex pairs here would have been merged into a single vertex.) Figure 5.19(a) shows the modelled distribution for pairs of two-track vertices in different events, where the combination of vertices has mass > 10 GeV, and we can see that it looks slightly different from the distribution of vertex pairs in the same event. This motivates the use of a weight, derived from the distributions in the z direction, to make the model better match the "same-event" distribution. Figure 5.19(b) shows the distances between pairs of two-track vertices in the z directions. The reason for the difference in the z direction is the correlation between two-track vertices in the same event, which does not exist between the different events. To correct this difference, a weight is obtained from the difference between the "different-event" and "same-event" z-distance distributions, and applied to the 3D distance distribution. After the correction, the value of the model at distances < 1 mm is taken as an estimate of the number of background vertices that could have been formed from merging vertices.

Figure 5.20(d) shows the close-up distribution near 1 mm for five-track vertices made of two-track and three-track vertices. Note that the same weight is applied. The estimated numbers of merged vertices are 3.69 ± 3.69 for $2 + 2$ track vertex and 0.01 ± 0.01 for $2 + 3$ track vertex. Note, as in the previous section, that the background estimation

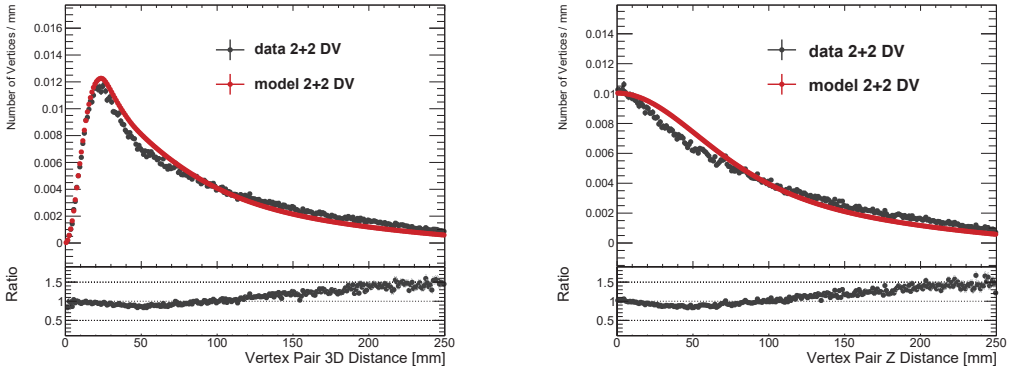

(a) 3D distance

(b) z distance

Figure 5.19: (a) Three-dimensional distance and (b) z distance between vertex pairs before weighting. The black points show the distance between the two-track vertices in the same event. The red points show a model calculated from the distance between two-track vertices in different events. The invariant mass for the combination of the two vertices is required to be > 10 GeV.

is made using events before the event cuts, therefore the estimation have to be scaled by the event-base scale factor described in Section 5.8.1.

In all these plots the black points indicate vertices found in the same event, while the blue line represents the model, constructed from pairs of vertices in different events.

5.7.3 Random Crossing Tracks

Displaced vertices arising from the Standard Model processes, such as meta stable particles, typically have low track multiplicity and mass. However, if a track from an arbitrary source gets mis-reconstructed as part of the vertex, it gets an additional track multiplicity. In addition, there is a possibility that the random track crosses the vertex with large opening angle by which the invariant mass becomes large enough to fall into the signal region. A data-driven method has been developed to estimate contribution of this kind of *random crossing tracks*. A model of the invariant mass distribution of vertices crossed by random crossing tracks is simulated by adding a track to a seed vertex and recalculating the invariant mass of the vertex.

Three regions, categorised by the number of tracks associated with vertices, are used in this method. The *control region* (CR) is made up of vertices with three tracks. The 3-track vertices are required to pass several quality cuts summarised in Tab. 5.2. The *validation region* (VR) is made up of vertices with four tracks passing the quality cuts but some requirements are changed. Finally, vertices with five or more tracks define the *signal region* (SR).

The geometric fiducial volume defined in Section 5.6.1 is divided into twelve individual regions as shown in Fig. 5.21. Invariant mass spectra of the vertices are created individually for these twelve regions. This division is made in order to consider the radial dependence on the properties of reconstructed vertices and random tracks. The properties of the tracks associated to vertices varies significantly with radial positions where the vertices were reconstructed because, for instance, the number of detector layers used in the track reconstruction depends on a vertex position. Therefore, the shape of the mass spectrum of the vertices with random crossing tracks depends on the radial regions

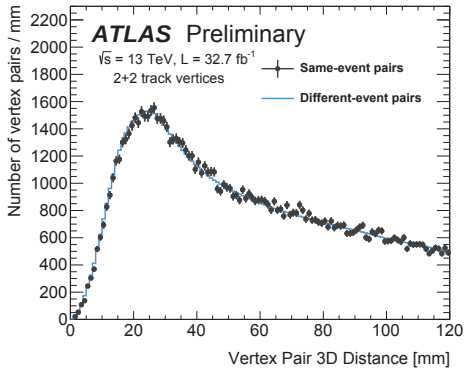

(a) 2+2 merged vertices

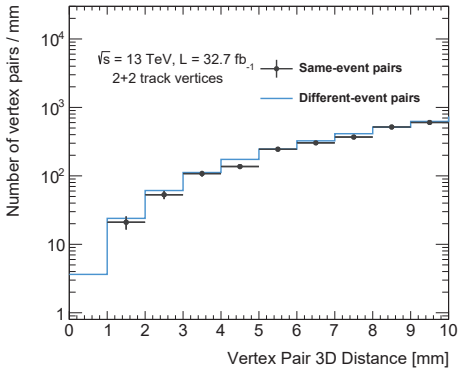

(b) zoomed view of 2+2

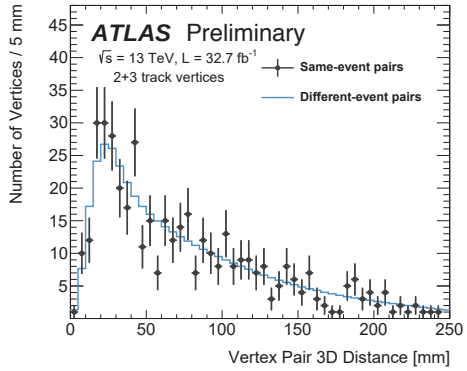

(c) 2+3 merged vertices

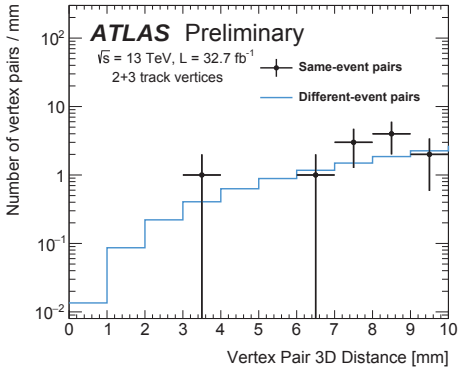

(d) zoomed view of 2+3

Figure 5.20: (a) Three-dimensional distance between two-track vertex pairs, after weighting. The right histogram (b) is a close-up view of the left histogram. (c) Three-dimensional distance between two-track and three-track vertices pairs, after weighting. (d) A close-up view of the 3D distance between two-track and three-track vertices, after weighting. The black points show the distance between the vertex pairs in the same event. The blue lines show a model calculated from the distance between vertex pairs in different events. The value of the model at less than 1 mm gives the estimate for the number of high-mass four-track or five-track vertices from this method.

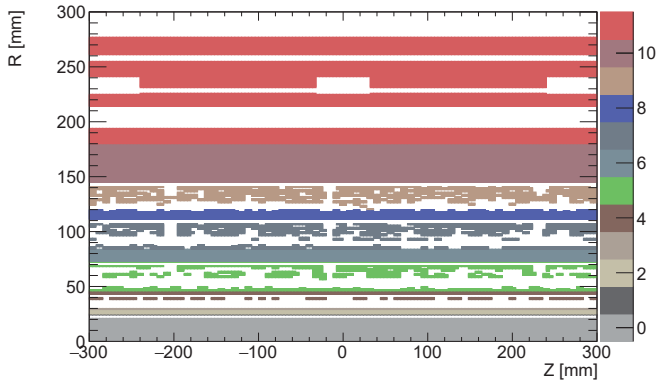

Figure 5.21: The properties of the displaced vertices changes as a function of r_{DV}, depending on the track properties. Therefore, to produce a correct background estimation, the fiducial volume is divided into twelve regions. The regions where detector materials exist are vetoed in this figure.

as well.

This data-driven method relies on the hypothesis that the probability for a track passing nearby a vertex, and get associated to it in the vertex reconstruction, is irrespective of the number of tracks on the original vertex. Figure 5.22 schematically describes the method for estimation of random crossing tracks. The method uses a vertex with $(n-1)$ associated tracks and adds a track to the vertex. Then, it becomes a n-track vertex with larger mass than the original one. Eq. (5.1) defines the expression for this model concisely and defines the components:

$$P_n(m_{\mathrm{DV}}) = f \cdot h_n(m_{\mathrm{DV}}), \tag{5.1}$$

where $h_n(m_{\mathrm{DV}})$ is a template of the high-mass vertex distribution built from $(n-1)$-track vertices by adding a random track and recalculating the invariant mass. $P_n(m_{\mathrm{DV}})$ is the *real* mass distribution of n-track vertices of data which is output from the vertex reconstruction algorithm, and f is the normalisation factor, also called a *crossing factor*. A crossing factor represents the probability that a vertex is randomly crossed by an additional track in the event. This is determined using data in the 3-track control region.

Seed vertices and track templates

Seed vertices are defined as $(n-1)$-track vertices. Mass spectra of n-track vertices are modelled by adding random tracks. All reconstructed vertices, passing the CR selection criteria in Tab. 5.2 are considered as seed vertices. The seed vertices are divided into the twelve radial regions.

The random tracks are sampled from track templates. The track templates are constructed by saving the track properties of (p_{T}, η, $\Delta\phi$) into three-dimensional histograms. All tracks in reconstructed vertices, with the mass above 3 GeV and the number of associated tracks is at least 3, are used to create the track templates. Here, $\Delta\phi$ is defined as the relative azimuthal angle between the track and the direction of the PV-DV vector. The relative angle is used instead of the absolute, in order to avoid creating vertices

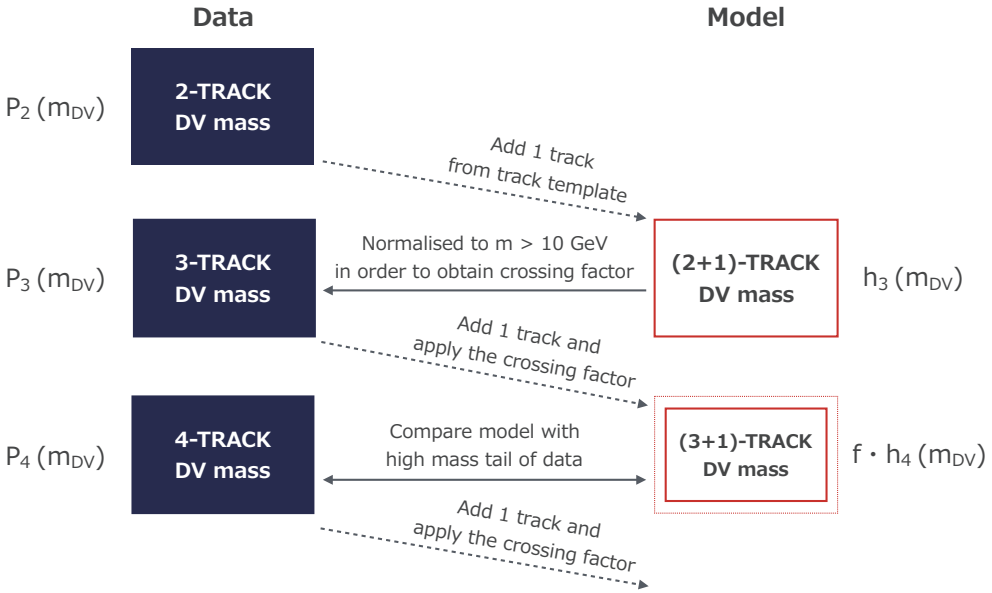

Figure 5.22: Schematic flow of the method for estimation of random crossing tracks.

that would not be reconstructed by the vertex algorithm. For instance, if the absolute angle is used, adding this track to a seed could easily create a vertex with a back-to-back topology. Such vertices would not be found in data as they are removed by the fake removal (see Section 4.1.4). A simple schematic in Fig. 5.23 shows how the relative angles of the track is defined and how the track is added to a seed vertex. The properties of template tracks are shown in Fig. 5.24 for all radial regions. Only tracks with $\Delta R \equiv \sqrt{(\Delta\phi)^2 + (\Delta\eta)^2} > 1.0$ are used to add to any seed vertices. Using tracks with lower ΔR would be a waste of statistics as these vertices would not contribute to modelling of high mass tail and fall outside the SR.

Constructing the invariant mass templates

The method is composed of the following three steps.

1. Construct templates for the DV mass distributions ($h_n(m_{\mathrm{DV}})$) of possible combinations of $(n-1)$-track DV plus a random track (e.g. 2+1, 3+1, 4+1 and 5+1 or higher).

2. Extract the normalisation factors f by scaling the mass templates from the random-track association method in the control region to the data, i.e. scaling the models of (2+1)-track vertices ($h_3(m_{\mathrm{DV}})$) to those of the 3-track vertices in the data ($P_3(m_{\mathrm{DV}})$):
$$f = \frac{\int_{10\,\mathrm{GeV}}^{+\infty} P_3(m_{\mathrm{DV}})\,\mathrm{d}m_{\mathrm{DV}}}{\int_{10\,\mathrm{GeV}}^{+\infty} h_3(m_{\mathrm{DV}})\,\mathrm{d}m_{\mathrm{DV}}} \tag{5.2}$$

3. Scale the estimated number of high-mass vertices with an event-based scale factor. This scale factor accounting for the difference between the efficiency of the event pre-selection and that of the final event selection which also includes explicit trigger, filter and offline $E_{\mathrm{T}}^{\mathrm{miss}}$ requirements.

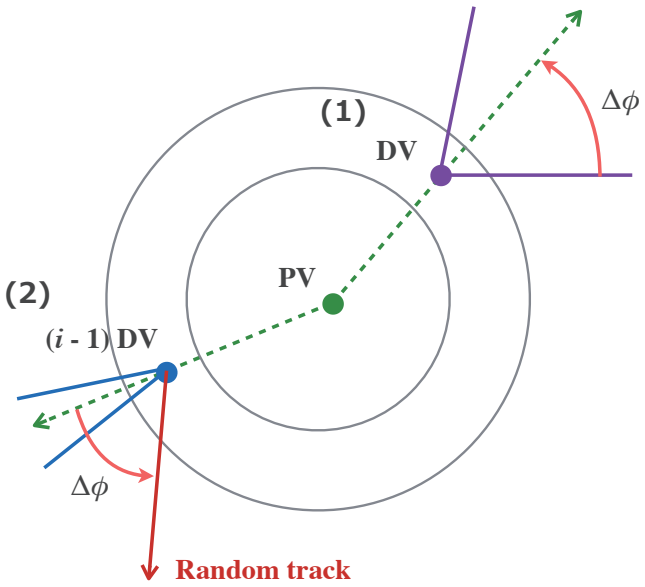

Figure 5.23: Schematic drawing showing the two steps of the random-track association method. In the vertex labeled (1) the relative azimuthal angle $\Delta\phi$ (marked with the curved red arrow) to the PV-DV direction (green dashed arrow) for each track in a DV which are filled into the track templates, and templates of η and p_{T} are built up in the same way. The vertex labeled (2) shows how the random track generated from the track templates are added to the $(n-1)$-track seed vertex to construct an n-track DV. A mass template is constructed by repeating the process many times. The concentric circles represent a simplification of a radial region of the fiducial volume.

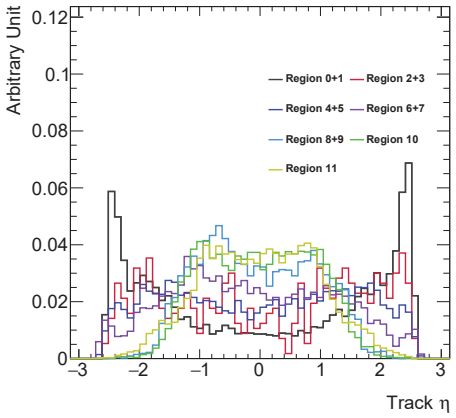

(a) Track η

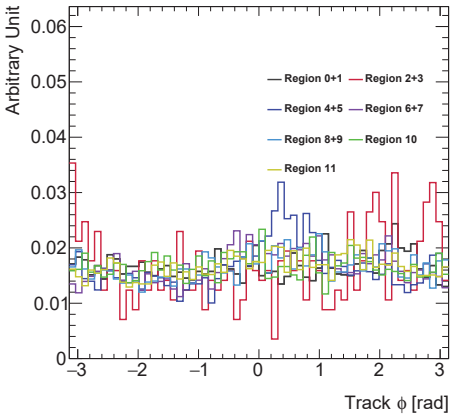

(b) Track ϕ

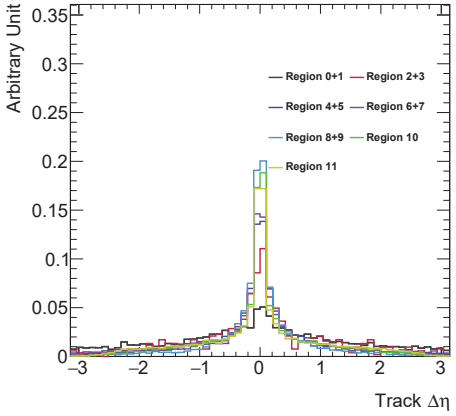

(c) Track $\Delta\eta$

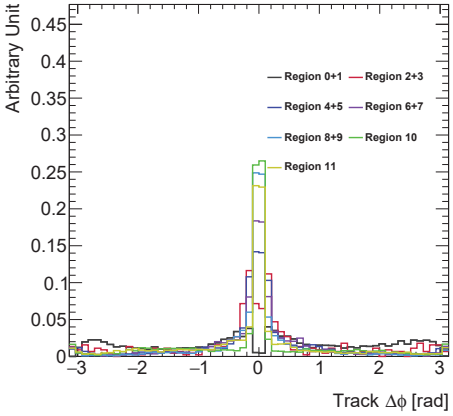

(d) Track $\Delta\phi$

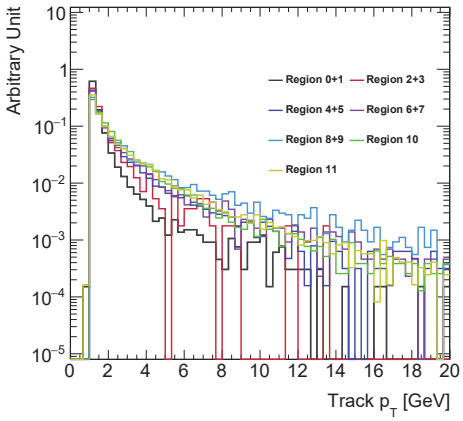

(e) Track p_T

Figure 5.24: The properties η, ϕ, $\Delta\eta$, $\Delta\phi$, p_{T} of tracks in the track templates for each region (Δ means with respect to the PV-DV direction). Several adjacent radial regions are merged because it is too dense to show 12 histograms overlaid. The central dips in $\Delta\phi$ distributions come from a requirement that only tracks with $d_0 > 2$ mm are used for secondary vertexing.

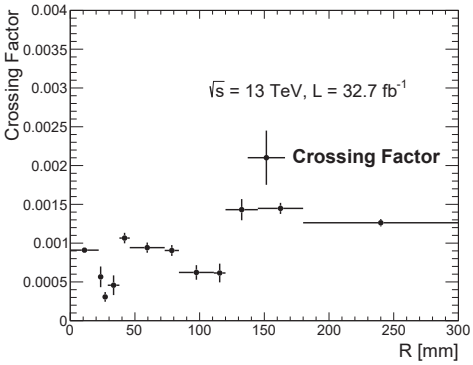

Figure 5.25: Crossing factor for the twelve radial region for 2016 data. The factors are calculated by normalising the model to data in the control region, for vertices with three tracks and mass larger than 10 GeV. The error bars represent the statistical uncertainties.

The first part constructs a mass template for each radial region by looping over all seed vertices and then sampling a random track from the track template of the corresponding region. This is done for all n-track multiplicities of the seed vertices. For the second step, a simple method is used to estimate the probability of having a randomly crossing track, denoted as a crossing factor. The 3-track control region is used, i.e. the (2+1)-track m_{DV} template is normalised to fit the high-mass region ($m_{\mathrm{DV}} > 10$ GeV) of the 3-track DV spectrum of the data. The extracted crossing fractions are shown in Fig. 5.25 for all radial regions. The resulting invariant mass spectra, after applying the crossing fraction, are able to reproduce the shape of the high-mass distribution from data in the CR (3-track DVs) as shown in Fig. 5.26 and 5.27.

Applying the crossing fractions to models of (3+1)-track (or higher track) DVs mass spectra, the number of 4-track (or higher track) DVs from random crossing tracks can be estimated. The estimated number of vertices from random crossing tracks with the mass of $m_{\mathrm{DV}} > 10$ GeV integrated over all regions is summarised in Tab. 5.4. Tab. 5.4 contains the estimations of hadronic interaction and merged vertices as well.

The background estimation method (including the crossing fractions) is validated in the two VRs. The two following sections discuss the details of validation of the background estimation.

5.7.4 Validation of the Background Estimation

The crossing factors are estimated in the 3-track control region. The number of 5 (or more track) DVs in the signal region can be estimated by applying the crossing factors to the templates of 4+1 (or 5+1, ...) track DVs and integrating them over the mass range above 10 GeV. However, the method itself needs to be validated before going into the signal region. Although it is a straightforward to use 4-track DVs as a validation region, this region could suffer from significant signal contamination and thus cannot be used for the validation without additional requirements. Here, two sets of requirements are used to create validation regions. The first set of requirements are an upper limit on $E_{\mathrm{T}}^{\mathrm{miss}}$ and a relative azimuthal angle between jets and $E_{\mathrm{T}}^{\mathrm{miss}}$. This low-$E_{\mathrm{T}}^{\mathrm{miss}}$ VR is denoted as "VRLM". The second region is made up of vertices in regions dominated by the detector materials and is denoted as "VRM". This region is enriched in hadronic

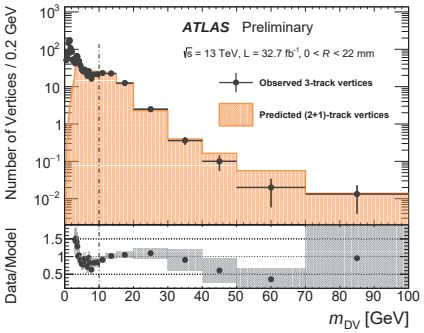

(a) inside Beam pipe ($R < 22$ mm)

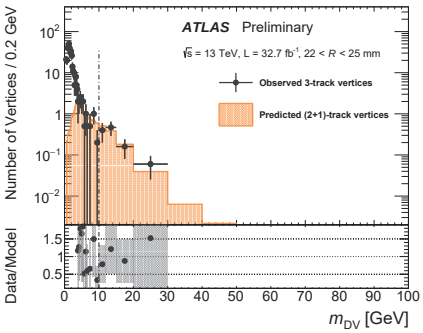

(b) around Beam pipe ($22 < R < 25$ mm)

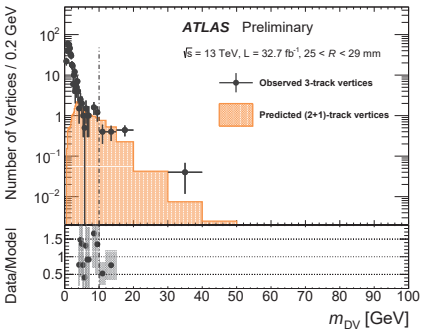

(c) inside IBL ($25 < R < 29$) mm)

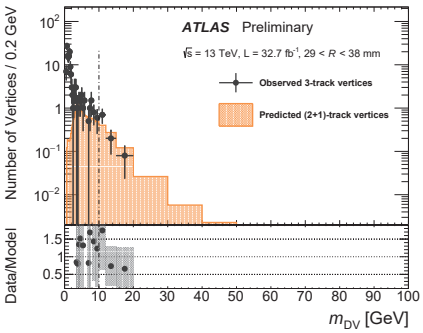

(d) around IBL ($29 < R < 38$ mm)

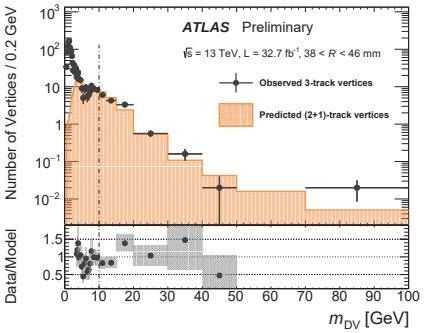

(e) inside B-Layer ($38 < R < 46$ mm)

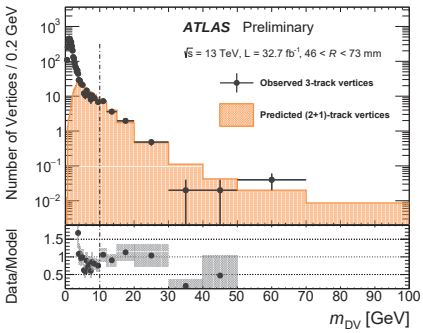

(f) around B-layer ($46 < R < 73$ mm)

Figure 5.26: 3-track m_{DV} distributions of 2016 data for regions 0–5. The modelled distributions are normalised to data by use of the high-mass range e.g. $m_{\mathrm{DV}} > 10$ GeV. The modelled vertices reproduce the high-mass shape distribution of the data.

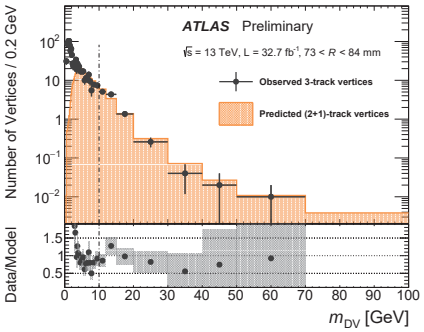

(a) inside Layer-1 ($73 < R < 84$) mm

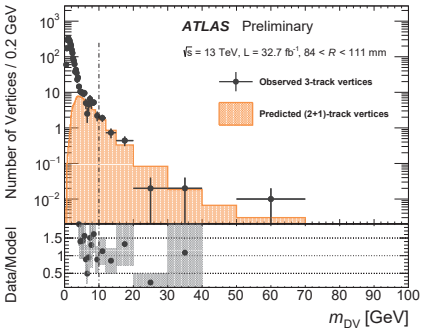

(b) around Layer-1 ($84 < R < 111$ mm)

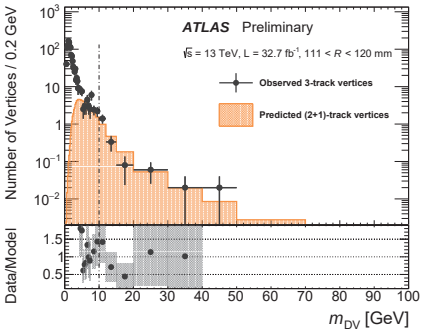

(c) inside Layer-2 ($111 < R < 120$ mm)

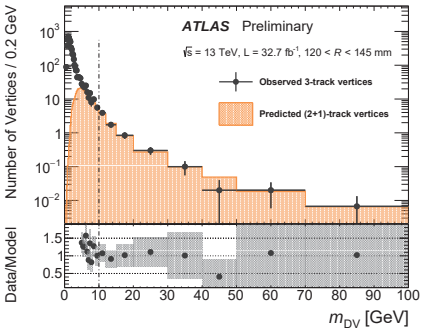

(d) around Layer-2 ($120 < R < 145$ mm)

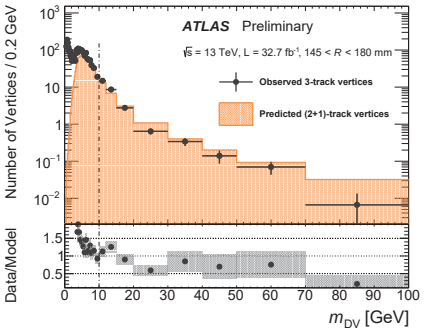

(e) inside octagonal support ($145 < R < 180$ mm)

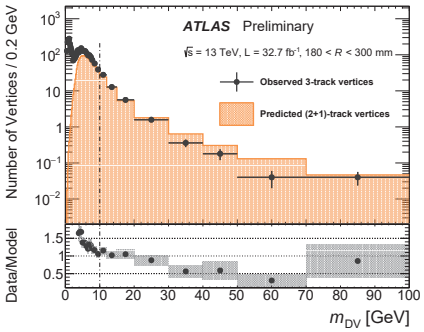

(f) inside 1st SCT Layer ($180 < R < 300$ mm)

Figure 5.27: 3-track m_{DV} distributions of 2016 data for regions 6–11. The modelled distributions are normalised to data by use of the high-mass range e.g. $m_{\mathrm{DV}} > 10$ GeV. The modelled vertices reproduce the high-mass shape distribution of the data. The error bars in the mass distributions and the grey bands in the bottom ratio distributions show the statistical uncertainties.

Table 5.4: Total number of estimated background vertices with a mass $m_{\mathrm{DV}} > 10$ GeV in the control, validation and signal regions, using the 2016 full integrated luminosity of 32.7 fb^{-1}. The numbers shown are obtained before applied the event-level transfer factors.

Control and Validation Regions				
	3 Track DV	4 Track DV		
	$(2+1)$ Track	$(3+1)$ Track	$(2+2)$ Track	Pure 4 Track
Estimation	3093 (Normalisation)	12.6 ± 0.3	3.64 ± 3.64	0.3 ± 0.9
Signal Region (before applying event-level transfer factor)				
	5 Track DV			
	(4+1) Track	(2+3) Track	Pure 5 Track	
Estimation	1.3 ± 0.07	0.01 ± 0.01	0.9 ± 2.8	
	6 Track DV		$7 \geq$ Track DV	
	(5+1) Track	Pure 6 Track	$(i+1)$ Track	Pure $7 \geq$ Track
Estimation	0.37 ± 0.03	0.18 ± 0.58	0.37 ± 0.03	1 ± 3

interactions by inverting the material veto requirement. In this region, it is expected to collect the DVs from instrumental effects more efficiently than the signal DVs of long-lived particles. Assuming that the number of vertices arising from random crossing tracks can be factorised into the product of the crossing factor and the number of "seed" vertices, an increase of the hadronic interaction vertices leads to a linear increase of the vertices from random crossing tracks. Therefore the VRM region allows for validation of the methodology used for the random-track crossing estimate with large statistics. In this sense, the VRM is complementary to the VRLM.

Low-$E_{\mathrm{T}}^{\mathrm{miss}}$ Validation Region - VRLM

Since non-negligible amounts of signal events would contaminate a simple 4-track data samples, a region with additional requirements for reducing the fraction of signal events is used for validation. An upper limit on the $E_{\mathrm{T}}^{\mathrm{miss}}$ would eliminate signal events with large mass difference between a gluino and the lightest neutralino to a large extent. The $E_{\mathrm{T}}^{\mathrm{miss}}$ cut is not effective for signal events in small mass difference scenarios due to the small amount of intrinsic $E_{\mathrm{T}}^{\mathrm{miss}}$. Instead an additional requirement is placed on the minimum azimuthal angle between the offline calibrated $E_{\mathrm{T}}^{\mathrm{miss}}$ and the reconstructed jets in the event, $\Delta\phi_{\mathrm{min}}$. Much of the background for this analysis originates from QCD multi-jet events. The energies of jets are occasionally mis-measured yielding $E_{\mathrm{T}}^{\mathrm{miss}}$, and thus the $\Delta\phi_{\mathrm{min}}$ of such events is peaked at 0 and $\pm\pi$. On the other hand, signal events with small intrinsic $E_{\mathrm{T}}^{\mathrm{miss}}$are more likely to obtain larger values of $\Delta\phi_{\mathrm{min}}$. For this analysis, this variable is calculated using all jets with $p_{\mathrm{T}} > 30$ GeV which passed the baseline jet selection described in Section 5.5.6. Distributions of the $E_{\mathrm{T}}^{\mathrm{miss}}$ and $\Delta\phi_{\mathrm{min}}$ are shown for data and various signals in Fig. 5.28 where the discrimination powers can be seen.

In order for a validation in VRLM to be valid in the SR as well, it must be shown that the DV properties are uncorrelated with both of $E_{\mathrm{T}}^{\mathrm{miss}}$ and $\Delta\phi_{\mathrm{min}}$. The distributions for the DV mass and track multiplicity are shown in slices of $E_{\mathrm{T}}^{\mathrm{miss}}$ and $\Delta\phi_{\mathrm{min}}$ in Fig. 5.29. The tails of the distributions are normalised to the same integral. These plots show only a tiny dependence on $E_{\mathrm{T}}^{\mathrm{miss}}$ and $\Delta\phi_{\mathrm{min}}$. Therefore, it should be reasonable to test the background estimation method using a part of data with selections on $E_{\mathrm{T}}^{\mathrm{miss}}$ and $\Delta\phi_{\mathrm{min}}$.

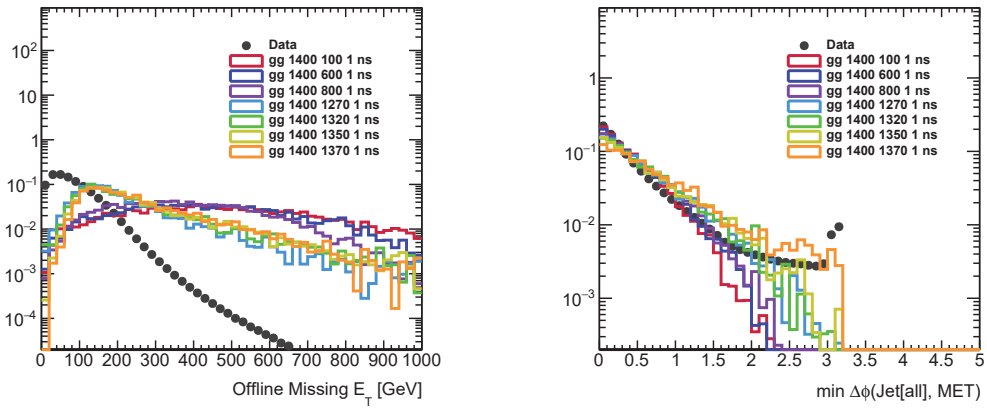

Figure 5.28: Normalised distributions are shown for data and various signals.

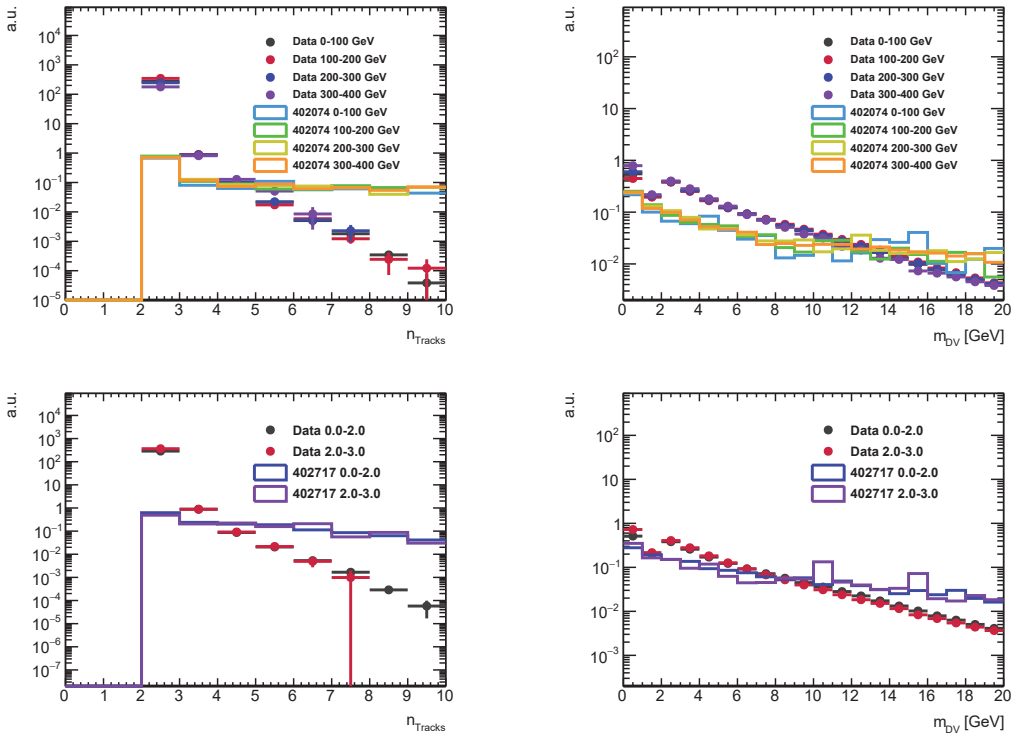

Figure 5.29: The properties of the DV candidates are shown as a function of $E_{\mathrm{T}}^{\mathrm{miss}}$ (top) and $\Delta\phi_{\mathrm{min}}$ (bottom). DV mass (right) and track multiplicity (left) are shown. The track multiplicity plots are normalised to the area above 3 and the mass distributions are normalised to the area above 3 GeV.

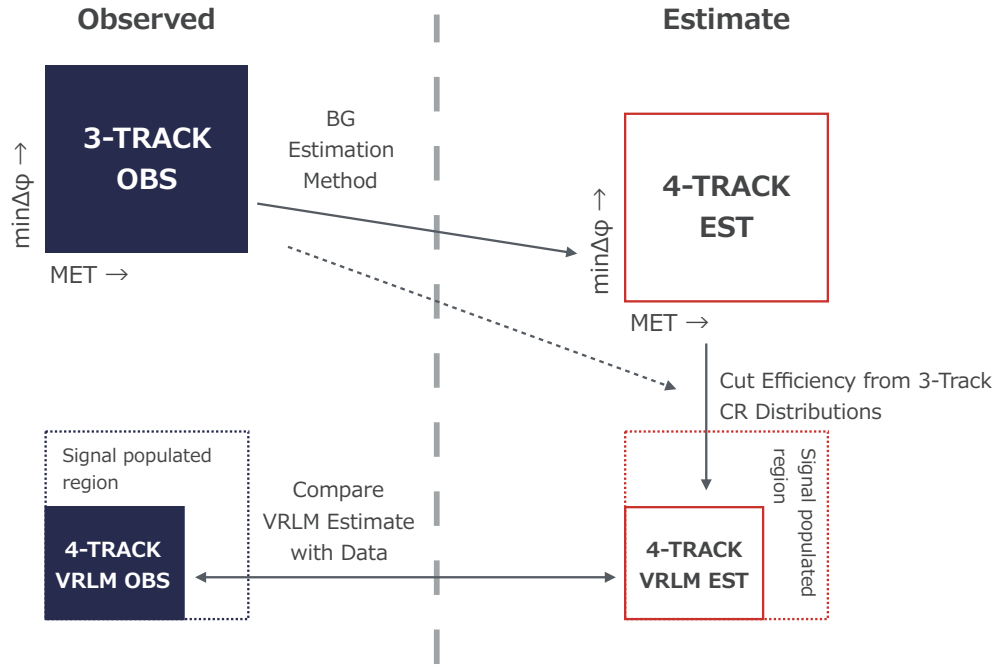

Figure 5.30: A qualitative diagram of the VRLM design is shown.

Since the correlation between DV properties and these variables is negligible, the estimation of 4-track DV in VRLM can be derived by scaling the estimation of 4-track DV in an original VR (16.5 ± 3.8 as shown in Tab. 5.4). The efficiency of passing the VRLM requirements of $E_{\mathrm{T}}^{\mathrm{miss}} < 150$ GeV and $\Delta\phi_{\mathrm{min}} < 0.75$ is measured in the 3-track control region to be $1854/3066 = 60.47\%$. The 4-track estimate in VRLM is then $(16.5 \pm 3.8) \times 60.47\% = 10.0 \pm 2.3$ events expected. The observed number of 4-track DVs in VRLM is 9 and these are consistent. A diagram summarising how the region is defined and where the various quantities are measured is shown in Fig. 5.30.

The levels of signal contamination expected in this region are shown in Fig. 5.31 for various gluino masses, neutralino masses and lifetimes. For the signal scenarios with $m_{\tilde{g}} \gtrsim \mathcal{O}(1)$ TeV that were not excluded by Run-1 results, signal contamination for this region is at most $\sim 10\%$ level although signal events were rather dominated before the selections.

Material-dominated Validation Region - VRM

When the material veto requirement is inverted, i.e. only vertices in the dense material-dominated regions are selected, the contributions from hadronic interactions increase dramatically. Just like the DVs from in-flight decays, these vertices can also be crossed by a random track. The amount of vertices with randomly crossing tracks is proportional to not only the track density but also the number of seed vertices. As the acceptance has been highly reduced, the contribution from the signal vertices to that region are going to be reduced also, allowing to obtain a region with high statistics but with low signal contamination. Figures 5.32 and 5.33 show 3-track m_{DV} distributions of 2016 data along with the predictions from the random-track model using the inverted material veto requirement. One can see that the predictions agree well with data in the material-rich

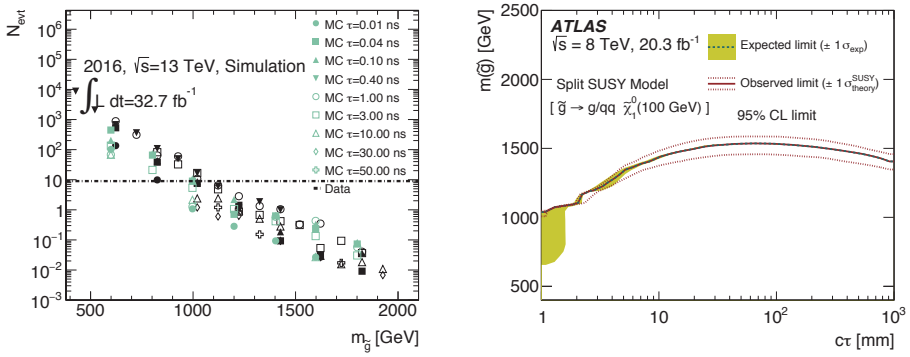

(a) (b)

Figure 5.31: (a) Signal yields are shown (markers) as a function of R-Hadron lifetime (shape) and gluino mass (x-axis). Those signal models with a 100 GeV LSP are shown in black. For reference, the yield in VRLM in data is shown in the dashed black line. For the signal scenarios with $m_{\tilde{g}} > 1000$ GeV that were not excluded by Run-1 results, signal contamination for this region is at most $\sim 10\%$ level. (b) For convenience, the Run-1 exclusion limits are shown for models with a 100 GeV LSP [32].

regions as well. Region 0, 6 and 10 (see Fig. 5.21) are excluded in the plots because the volume vetoed by material map in those regions is tiny.

In addition, Fig. 5.34 and 5.35 show the same distributions for 4-track DVs. The high-mass tails are well modelled by the orange mass templates.

Summary of the observed and expected numbers of 4-track DVs with $m_{\mathrm{DV}} > 10$ GeV in the regions with inverted material veto is shown in Fig. 5.36(a). The agreement between data and estimation is good in this region. The observed number of DVs there is 177. The expected number of DVs from randomly crossing tracks is $137.4 \pm 2.9\,(\mathrm{stat.}) \pm 29.8\,(\mathrm{syst.})$. The difference between these numbers could be explained by contribution of hadronic interactions as in the following paragraph.

Figure 5.36(b) shows the summation of the 4-track m_{DV} distributions. The number of DVs from hadronic interaction is estimated by fitting this using an exponential function and extrapolating it to $m_{\mathrm{DV}} > 10$ GeV. The estimated number of DVs from hadronic interactions is $16 \pm 1\,(\mathrm{stat.})$. The sum of these numbers are consistent with the observed number of DVs and the background estimation method has been validated in `VRM`.

Signal contamination in this VR is evaluated in Fig. 5.37. The event yields of signal samples which are not excluded yet ($m_{\tilde{g}} \gtrsim 1$ TeV) are below 10% level of the event yield of data, irrespective of the LSP mass and the gluino lifetime.

5.7.5 Systematic Uncertainties on Background Estimation Methods

Hadronic Interaction

The validity of the exponential assumption used in the estimation of hadronic interaction is tested in a truth-level study using the GEANT4-based simulation of hadronic interactions. Using PYTHIA8 dijet samples, the truth-level mass distributions of hadronic interactions are studied in bins of vertex track multiplicity. When fitting the mass distribution to an exponential in the range 5-10 GeV and extrapolating to the region for

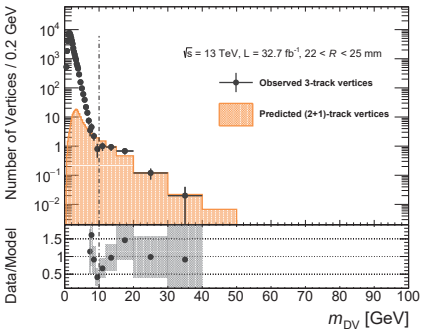

(a) around Beam pipe ($22 < R < 25$ mm)

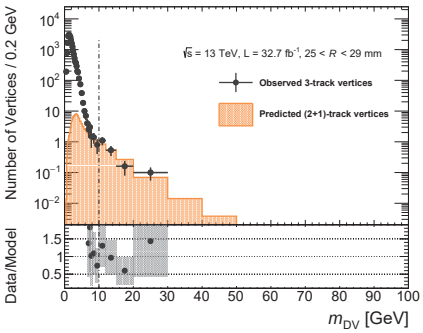

(b) inside IBL ($25 < R < 29$) mm)

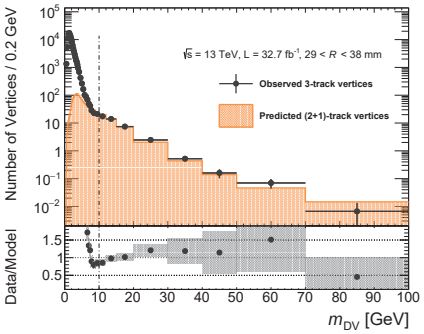

(c) around IBL ($29 < R < 38$ mm)

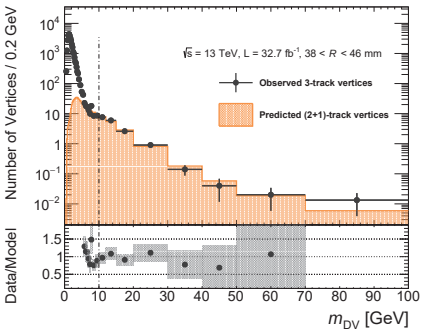

(d) inside B-Layer ($38 < R < 46$ mm)

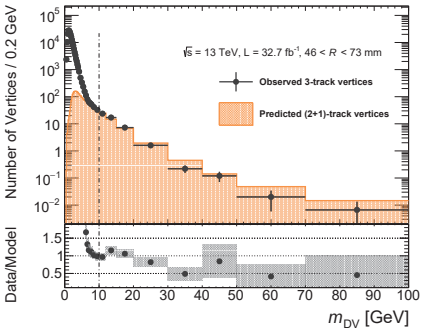

(e) around B-layer ($46 < R < 73$ mm)

Figure 5.32: 3-track m_{DV} distributions of 2016 data with inverted material veto requirement for regions 1–5. The modelled distributions are normalised to data by use of the high-mass range e.g. $m_{\mathrm{DV}} > 10$ GeV. The model reproduces shape of the distribution of the data at high mass well.

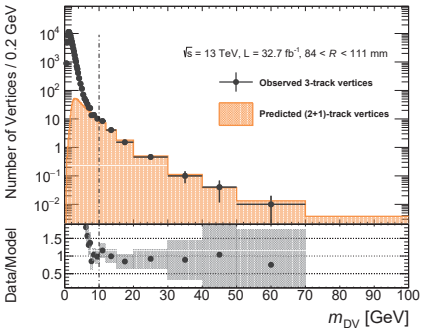

(a) around Layer-1 ($84 < R < 111$ mm)

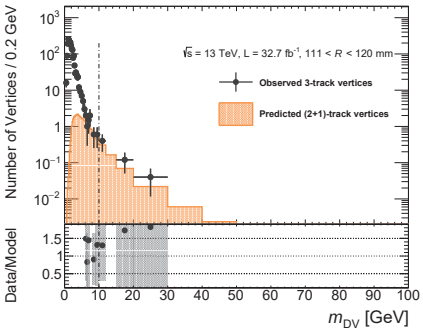

(b) inside Layer-2 ($111 < R < 120$ mm)

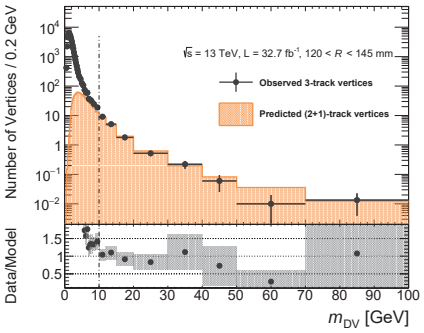

(c) around Layer-2 ($120 < R < 145$ mm)

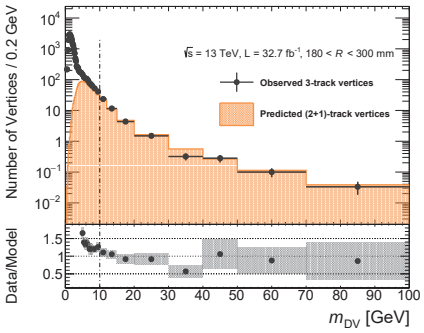

(d) inside 1st SCT Layer ($180 < R < 300$ mm)

Figure 5.33: 3-track m_{DV} distributions of 2016 data with inverted material veto requirement for regions 7-9 and 11. The modelled distributions are normalised to data by use of the high-mass range e.g. $m_{\mathrm{DV}} > 10$ GeV. The model reproduces the shape of the high-mass region of the distribution for the data well. The error bars in the mass distributions and the grey bands in the bottom ratio distributions show statistical uncertainties only.

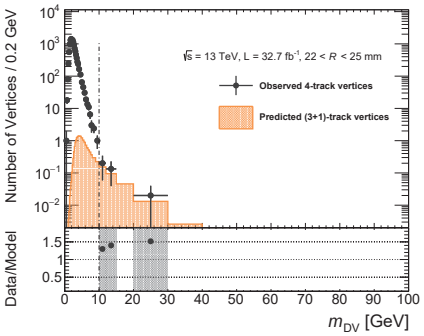

(a) around Beam pipe ($22 < R < 25$ mm)

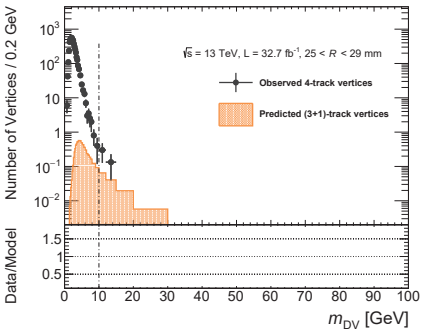

(b) inside IBL ($25 < R < 29$) mm)

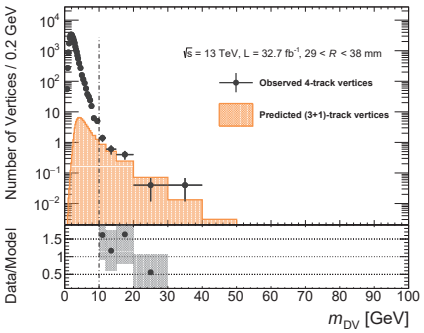

(c) around IBL ($29 < R < 38$ mm)

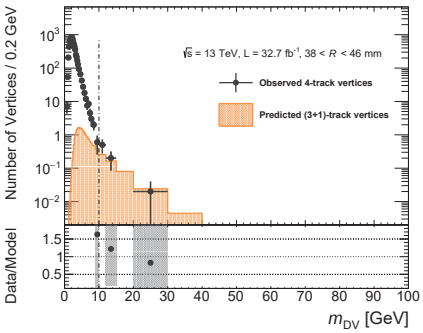

(d) inside B-Layer ($38 < R < 46$ mm)

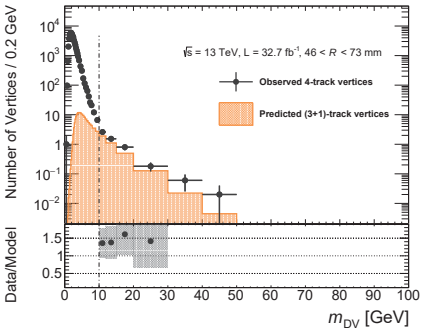

(e) around B-layer ($46 < R < 73$ mm)

Figure 5.34: 4-track m_{DV} distributions of 2016 data with inverted material veto requirement for regions 1–5. The modelled distributions are normalised to data by use of the high-mass range e.g. $m_{\mathrm{DV}} > 10$ GeV. The model reproduces the shape of the high-mass region of the distribution for the data well.

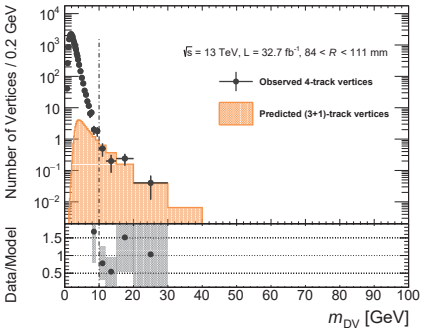

(a) around Layer-1 ($84 < R < 111$ mm)

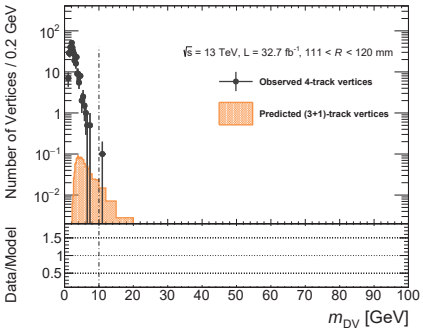

(b) inside Layer-2 ($111 < R < 120$ mm)

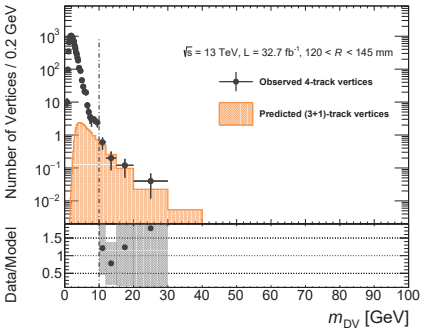

(c) around Layer-2 ($120 < R < 145$ mm)

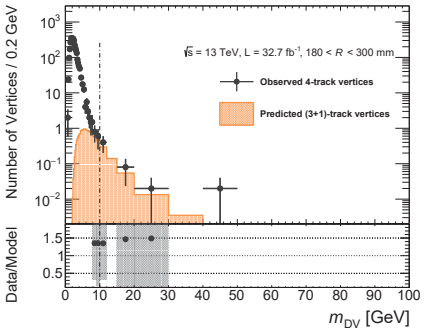

(d) inside 1st SCT Layer ($180 < R < 300$ mm)

Figure 5.35: 4-track m_{DV} distributions of 2016 data with inverted material veto requirement for regions 7-9 and 11. The modelled distributions are normalised to data by use of the high-mass range e.g. $m_{\mathrm{DV}} > 10$ GeV. The model predictions match the shape of the high-mass region of the distribution for the data well. The error bars in the mass distributions and the grey bands in the bottom ratio distributions show statistical uncertainties only.

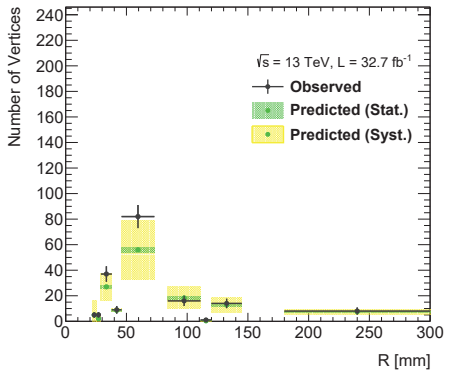

(a)

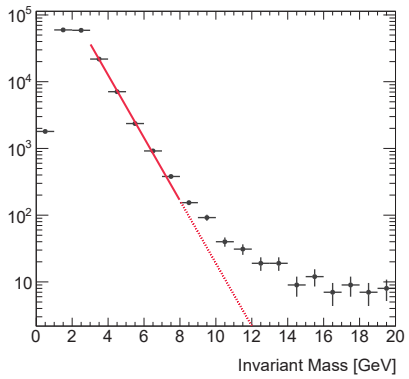

(b)

Figure 5.36: (a) Summary of the observed and expected numbers of 4-track DVs with mass above 10 GeV in the regions with inverted material veto. Region 0, 6 and 10 are excluded in this figure because too tiny volume is vetoed by material map there. (b) The summation of the 4-track m_{DV} distributions in Figure 5.34 and 5.35. The red line represents a fitted exponential function.

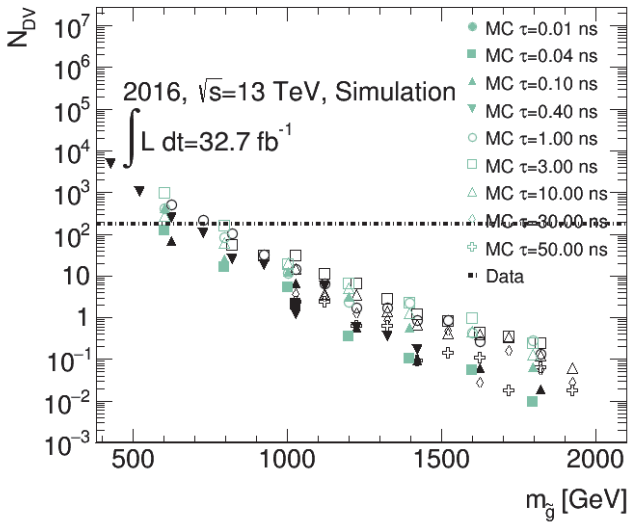

Figure 5.37: Yields of data and R-hadron pair production events in the additional VR with inverted material veto requirement. The horizontal dashed line represents the yield of data. The black markers show event yield of each sample with the lightest neutralino mass of 100 GeV. The green markers show event yield of each sample but the lightest neutralino mass is not 100 GeV. For the signal scenarios with $m_{\tilde{g}} > 1000$ GeV that were not excluded by Run-1 results, signal contamination for this region is at most $\sim 10\%$ level.

$m_{\mathrm{DV}} > 10$ GeV, a deviation of approximitely 300% is seen between the integral of the fit function and the truth level distribution. As a result, an additional 300% uncertainty is added to the estimate of hadronic interactions. With this additional uncertainty, the hadronic interaction estimates become 0.3 ± 0.9 for 4-track DVs, 0.9 ± 2.8 for 5-track DVs, 0.18 ± 0.58 for 6-track DVs and 1 ± 3 for $\geq$ 7-track DVs. The details of this study can be found in Appendix A.

Random Crossing Track

The crossing fractions are derived using the number of vertices with the mass above 10 GeV to normalise the mass spectra of model to that of data for all the twelve regions. However, if the shape of model distribution does not perfectly agree with data, an uncertainty on the model will enter into the background estimation. The effects can be estimated by varying the mass interval ± 5 GeV used to estimate the crossing fractions. This gives an estimate of how stable the crossing fraction is and an uncertainty of the shape of the model as shown in Fig. 5.38. The systematic uncertainties on the final estimates are summarised in the next section.

5.8 Results

5.8.1 Total Background Estimate and Event-Selection Transfer Factor

The output of the background estimation techniques, the total number of vertices, integrating over all regions for vertices with a mass larger than 10 GeV, is shown in Tab. 5.5.

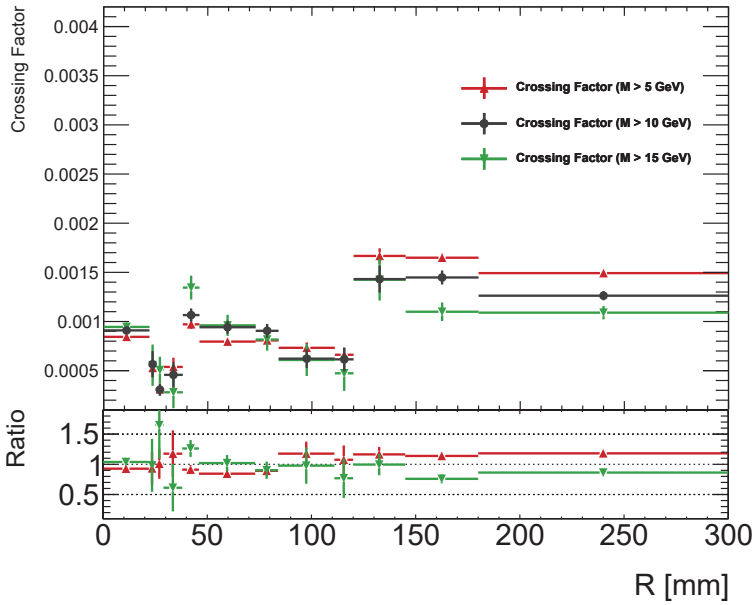

Figure 5.38: Crossing factors which are derived from different m_{DV} intervals for fitting mass template to data in each region in 2016. Black dots show the crossing factors in nominal setting (using data points in $m_{\mathrm{DV}} > 10$ GeV for fitting, red dots are those with $m_{\mathrm{DV}} > 5$ GeV cut, and green dots are those with $m_{\mathrm{DV}} > 15$ GeV cut.

The SR was blinded until the background estimation became convincing. These estimates represent the expected number of selected vertices (i.e. *not number of events*) based on the CR selections as defined in Tab. 5.2.

In order to obtain an estimate for the number of events in the signal region, two conversions must be made. One must account for difference of the acceptances between the CR selections and the SR selections used for the signal region events. Multiplying the estimate by the ratio of the yields for the two selections accounts for this effect.

The second consideration is the conversion from a vertex-level estimate to an event-level estimate for the sake of interpretations. This is, ideally, the ratio of the number of *vertices* observed in the SR selections to the number of *events* observed in the SR selections. Unfortunately, this was not accessible when the signal region was blinded, so a proxy is used: the ratio of the number of *vertices* in the CR selections to the number of *events* in the CR selections. The degree to which this is an appropriate proxy will be taken as a systematic.

The steps above are summarised in Eq. (5.3).

$$\begin{aligned} N_{SR}^{Event} &= N_{Base}^{DV} \times \frac{N_{Full}^{Event}}{N_{Base}^{Event}} \times \left(\frac{N_{Full}^{DV}}{N_{Full}^{Event}} \right)^{-1} \\ &\approx N_{Base}^{DV} \times \frac{N_{Full}^{Event}}{N_{Base}^{Event}} \times \left(\frac{N_{Base}^{DV}}{N_{Base}^{Event}} \right)^{-1}, \end{aligned} \tag{5.3}$$

where N^{Event} and N^{DV} are the number of events and DVs after certain selections, respectively. The subscript *Base* indicates that the number is one after the CR selections and the subscript *Full* indicates that the number is the one after the SR selections except

Table 5.5: Total number of estimated background vertices with a mass $m_{\mathrm{DV}} > 10$ GeV for the vertex selections used in the control, validation, and signal regions. The $(n+1)$-track contributions are estimated using the accidental-crossing factor method (Section 5.7.3), the $(n+2)$-track contribution is obtained from merged vertices (Section 5.7.2), and the pure n-track estimation is evaluated using the hadronic interactions (Section 5.7.1). The control region yield is normalised to data. Also shown are the estimated background event yields in the pre-selection region with at least 5 tracks. The predicted background yield in the full signal region appears in the bottom row, and includes the transfer factors shown.

Vertex Selection	Sub-Region	Background component	Estimated
CR, 3-track		$(2+1)$-track	3093 (Normalised)
VRs, 4-track	VRLM	$(3+1)$-track	$12.6 \pm 0.3 \pm 1.1$
		$(2+2)$-track	3.64 ± 3.64
		Pure 4-track	0.3 ± 0.9
		Sub-total	16.5 ± 3.9
		Selection eff. corr.	$(\ldots \times [56 \pm 6]\%)$
		Total	9 ± 2
	VRM	$(3+1)$-track	$137.4 \pm 2.9 \pm 29.8$
		Pure 4-track	16 ± 47
		Total	153 ± 55.7
SR-like, ≥5-track	5-tracks	$(4+1)$-track	$1.3 \pm 0.07 \pm 0.12$
		$(2+3)$-track	0.01 ± 0.01
		Pure 5-track	0.9 ± 2.8
		Total	2.2 ± 2.8
	6-tracks	$(5+1)$-track	$0.37 \pm 0.03 \pm 0.04$
		Pure 6-track	0.18 ± 0.58
		Total	0.55 ± 0.58
	$\geq$ 7-tracks	$(n+1)$-track	$0.37 \pm 0.03 \pm 0.04$
		Pure $\geq$ 7-track	1 ± 3
		Total	1.4 ± 3
	Total		4.2 ± 4.1
Full SR event & Vertex selection	*Event selection transfer factor*		$(\ldots \times [5.08 \pm 2.56] \times 10^{-3})$
	Vertex-to-event transfer factor		$(\ldots \times [1.0 \pm 0.16])$
	Total		0.02 ± 0.02

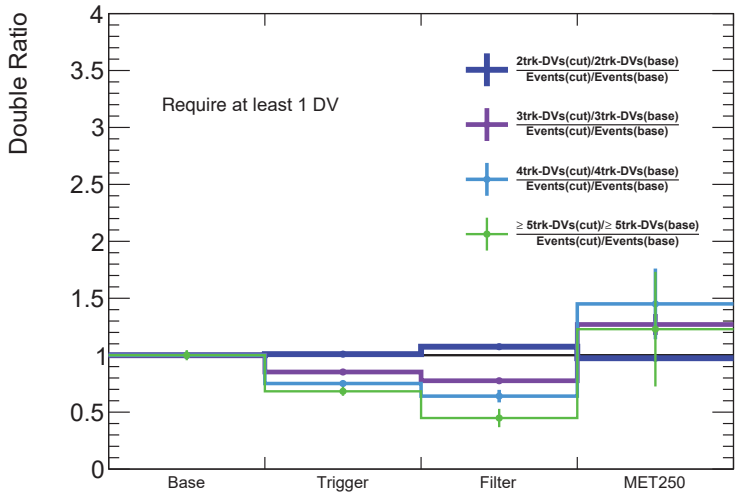

Figure 5.39: Cut flow showing how the number of displaced vertices per event changes with applied selections. The horizontal axis shows the cut level and the vertical axis shows the double ratio of the number of DVs and events after the full selections to those after the base (CR) cuts. If there is no correlations between the number of DVs and events, the double ratio would lie on unity. The discrepancies from unity are taken as systematic uncertainty of the event selection transfer factor.

for the cuts on m_{DV} and the number of associated tracks (see Tab. 5.2). The second factor in Eq. (5.3) is found to be 5.08×10^{-3} ($\pm 0.02 \times 10^{-3}$ [stat.]). The third factor is found to be 1.0. The degree to which the approximation in Eq. (5.3) is valid can be quantified by studying the double ratio

$$\frac{N_{Full}^{DV}/N_{Full}^{Event}}{N_{Base}^{DV}/N_{Base}^{Event}} = \frac{N_{Full}^{DV}/N_{Base}^{DV}}{N_{Full}^{Event}/N_{Base}^{Event}}. \tag{5.4}$$

This double ratio as a function of the cut level is shown in Fig. 5.39 for different DV track multiplicities. The deviation from unity suggests that a 50% uncertainty accounts for the degree to which the assumption holds. An additional uncertainty comes from the dependence of the third factor in Eq. (5.3) on the properties of the reconstructed DVs. The number of vertices per event as a function of the mass and track multiplicity of the vertices in the CR is shown in Fig. 5.40. It is shown that the number of DVs per event is 1.0 for DVs with any masses and at least 3 associated tracks. For 2-track DVs, the value varies up to 1.16. This 0.16 difference is taken as the systematic uncertainty conservatively. This gives a total scaling factor of $5.08 \times 10^{-3} \pm 2.56 \times 10^{-3}$.

With this, the final nominal estimate for the number of events in the signal region is

$$\begin{aligned} N_{SR}^{Events} &= [4.2 \pm 4.1] \times [\, 5.08 \times 10^{-3} \pm 2.56 \times 10^{-3}] \\ &= 0.02 \pm 0.02 \end{aligned} \tag{5.5}$$

Table 5.6 summarises the estimates described above and the observed numbers. Figure 5.41 shows the two-dimensional distribution of m_{DV} and track multiplicity for DVs in events that pass all signal region event selection criteria. Drawn numbers correspond to

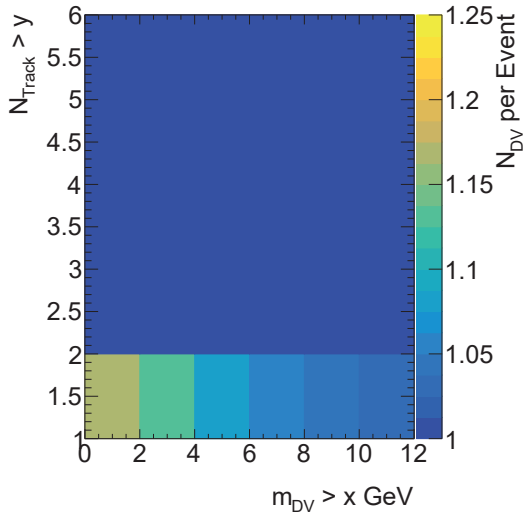

Figure 5.40: Number of DVs per event as a function of DV mass and track multiplicity. The dark blue region with $N_{\text{Track}} > 2$ indicates that the bin entries are unity there.

Table 5.6: The observed results for the control, validation, and signal regions are shown along with the background expectations for the 32.7 fb^{-1} of data collected in 2016.

Vertex Selection	Sub-Region	Estimated	Observed
CR, 3-track			3093
VRs, 4-track	VRLM	9 ± 2	9
	VRM	153 ± 56	177
SR-like, ≥5-track	5-tracks	2.2 ± 2.8	1
	6-tracks	0.55 ± 0.58	1
	≥7-tracks	1.4 ± 3.0	3
	Total	4.2 ± 4.1	5
Full SR event & vertex selection	**Total**	0.02 ± 0.02	0

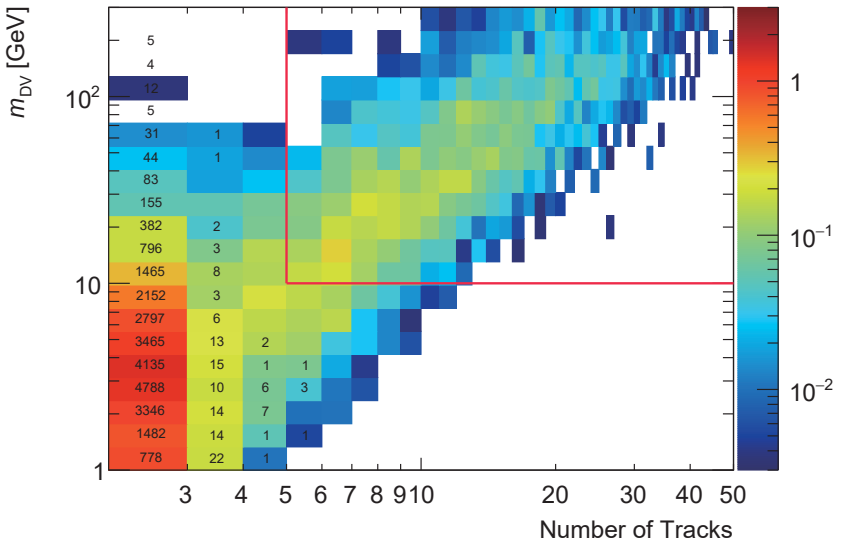

Figure 5.41: The two-dimensional distribution of m_{DV} and track multiplicity for DVs in events that pass all signal region event selection criteria. Drawn numbers correspond to the observations in data, while the colour-representation shows an example distribution for an R-hadron signal MC sample with $(m_{\tilde{g}}, m_{\tilde{\chi}_1^0}, \tau_{\tilde{g}}) = (2000\,[\mathrm{GeV}], 100\,[\mathrm{GeV}], 1\,[\mathrm{ns}])$ as a reference. The red lines represent the boundary of the signal region requirements.

the observations in data, while the colour-representation shows an example distribution for an R-hadron signal MC sample with $(m_{\tilde{g}}, m_{\tilde{\chi}_1^0}, \tau_{\tilde{g}}) = (2000\,[\mathrm{GeV}], 100\,[\mathrm{GeV}], 1\,[\mathrm{ns}])$ as a reference. The red lines represent the boundary of the signal region requirements.

The number of observed events in the signal region is 0 in the dataset used in this analysis. The observations are consistent with all the estimates of background events within the uncertainties. Given the results, limit setting on parameter space of a Split-SUSY model will be discussed in the next chapter.

Chapter 6

Interpretation in Supersymmetry

6.1 Introduction

The ATLAS and CMS experiments have tested many models of physics beyond the Standard Model. The Minimal Supersymmetric Standard Model (MSSM) is one of the main targets of the experiments. Despite their enthusiastic efforts, no evidence of new physics has been observed and a wide range of parameter space has been excluded.

In setting limits in the parameter space, there are two main conceptual approaches to statistics: *Frequentism* and *Bayesianism*. In the classical Frequentist approach, data are regarded as a repeatable random sample and there is a frequency. Probability is interpreted as the limit of a relative frequency in an infinite number of trials given a certain hypothesis. In the latter Bayesian approach, data are rather fixed and one can consider probability of a hypothesis. Probability is then interpreted as a degree of belief in the reliability of the hypothesis in a Bayesian view. It is arbitrary to choose one of the approaches, or to make use of the hybrid of them. In this analysis, the Bayesian approach is adopted for estimation of credible interval of parameters of interest. Statistical tools needed for this purpose is provided by the RooStats toolkit [116, 117], which was developed originally within the BaBar collaboration [118]. The 95% credible intervals are calculated by integrating the posterior distribution from its mode downwards until the interval has a 95% of whole probability contents. For the integration, a conventional Markov-Chain Monte Carlo (MCMC) method is used in this analysis. A Markov Chain is constructed with the Metropolis-Hastings algorithm [119, 120].

The target signature is a pair production of long-lived gluinos which both form R-hadrons and decay to a pair of quarks and the lightest neutralino via squark exchange expected in a Split-SUSY model. When the mass of squarks are fixed at a certain value (10 TeV in this dissertation), parameters of interest are just the gluino mass ($m_{\tilde{g}}$), neutralino mass ($m_{\tilde{\chi}_1^0}$) and gluino lifetime (τ). Although each MC sample is generated in a configuration of fixed parameters, the effective gluino lifetime of a sample is varied by applying a proper weight. A method of the *lifetime reweighting* is described in Section 6.2 and a summary of systematic uncertainties on the signal efficiency is given in Section 6.3. Given these information and the analysis results shown in Section 5.8.1, several limit plots are illustrated and discussed in Section 6.4.

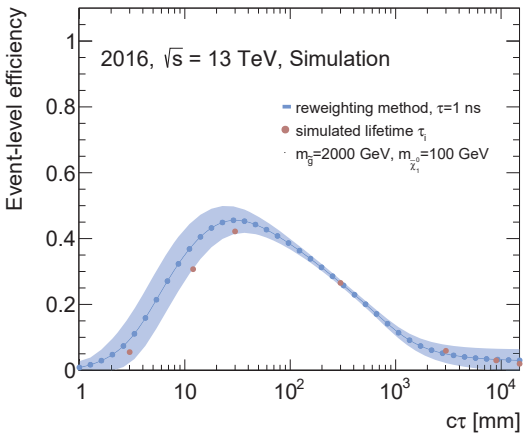

Figure 6.1: Closure test for the efficiency re-weighting procedure. A sample generated with $\tau = 1$ ns ($c\tau \simeq 300$ mm) is re-weighted to give the blue curve (statistical uncertainty considered only). This is compared with several samples with the same mass spectrum but generated at different $\tau = 0.01$, 0.04, 0.1, 1, 10, 30 and 50 ns, (corresponding to $c\tau = 3.0$, 12.0, 30.0, 300, 3000, 9000 and 15000 mm), which are represented as the red points. The figure shows the closure of the weighting treatment to within statistical uncertainty in all the points considered.

6.2 Lifetime Reweighting

Signal MC samples used in this analysis have fixed values of the average lifetime τ of the long-lived particle. In order to evaluate the efficiencies for any values of τ, a simple re-weighting method is used. Each event that passes the selection cuts (i.e. event-level cuts and at least one DV passing all vertex selection criteria) is re-weighted by the probability that both true long-lived particles would have been decayed with the given lifetime at the decay positions in the particular event. The weight assigned for a given value of the average lifetime of a MC sample τ_{MC} and given true decay times t_1^{true} and t_2^{true} is,

$$w(t_1^{\text{true}}, t_2^{\text{true}}) = \left(\frac{\tau_{\text{MC}}}{\tau_{\text{target}}}\right)^2 \exp\left(\frac{t_1^{\text{true}}}{\tau_{\text{MC}}} - \frac{t_1^{\text{true}}}{\tau_{\text{target}}}\right) \exp\left(\frac{t_2^{\text{true}}}{\tau_{\text{MC}}} - \frac{t_2^{\text{true}}}{\tau_{\text{target}}}\right), \tag{6.1}$$

in order to reproduce a sample with lifetime of τ_{target}.

Figure 6.1 shows a comparison between the efficiency-vs-lifetime curve from this re-weighting method, for an R-hadron sample with 2 TeV gluino and 100 GeV neutralino at 1 ns, and different samples simulated with different lifetimes: 0.01 ns, 0.04 ns, 0.1 ns, 10 ns, 30 ns and 50 ns. The method shows validity of this reweighting method within the statistical uncertainty.

6.3 Systematic Uncertainties on the Signal Efficiency

Efficiency-vs-lifetime relations can be derived with the lifetime reweighting method for each parameter point. One must take account of additional "systematic" uncertainties on the signal efficiencies. Three dominant sources of systematic uncertainties on tracking/vertexing performance, ISR/FSR modelling or pileup reweighting, are discussed in this section.

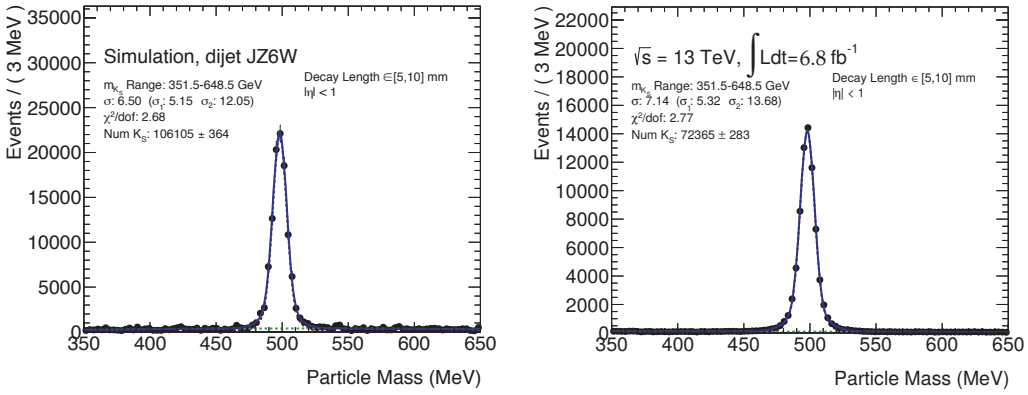

(a) (b)

Figure 6.2: An example of the double Gaussian fit used to count the number of signal K_S^0 on the barrel for the decay length interval 5-10 mm, for MC (a) and data (b). The green line corresponds to the background-function, the red line is the fit for the signal while the blue lines are the combined fit. Using a simultaneous fit, the number of K_S^0 candidates are extracted.

6.3.1 Tracking/Vertexing Performance

To estimate the systematic uncertainty from the track reconstruction efficiency on the vertex reconstruction, the ratio of K_S^0 yields are compared for a few intervals of decay radii. A deviation from unity for this ratio can be used to approximate the uncertainty in the track reconstruction efficiency in MC. From the maximum discrepancy a track-killing factor is derived which is then applied to MC and the vertexing algorithm is re-run, to estimate the effect on the vertex reconstruction efficiency. The efficiency-vs-$c\tau$ and efficiency-vs-R estimates are then made for the signal samples with the track-killing fraction applied.

The data selected for this study has been obtained from the `DRAW_RPVLL` 2016 data sample described in section 5.2.1, in particular runs between `297447` and `303201` corresponding to 6.8 fb^{-1}. The MC samples used are dijet samples produced with Pythia8.

The number of K_S^0 candidates found in each interval of decay length, 5-10 mm, 10-15 mm, 15-25 mm and 25-40 mm, are counted using a fit. The fit function for this counting is a combination of a double Gaussian for the signal and a polynomial function for the background. Figure 6.2 show the fit for MC and data in the barrel region and for the interval 5-10 mm.

Since the K_S^0 production rate is not known in MC and data, the samples are individually normalised to the amount of K_S^0 seen at the smallest decay lengths. The maximum discrepancy is then taken as the maximum deviation of the double ratio $\frac{Data_i/Data_0}{MC_i/MC_0}$. Figure 6.3 shows the final result with the ratio for the barrel region ($|\eta| < 1$) and the endcap region ($|\eta| \geq 1$), the maximum discrepancy is taken to be 10% in the barrel and 20% in the endcap. The inefficiency to reconstruct K_S^0 as a function of the inefficiency in tracking can be calculated as following:

$$(1 - \epsilon_{K_S}) = 2 \cdot (1 - \epsilon_{trk}) - (1 - \epsilon_{trk})^2 \tag{6.2}$$

The track-killing factor is estimated to the first order as half the value of the maximum

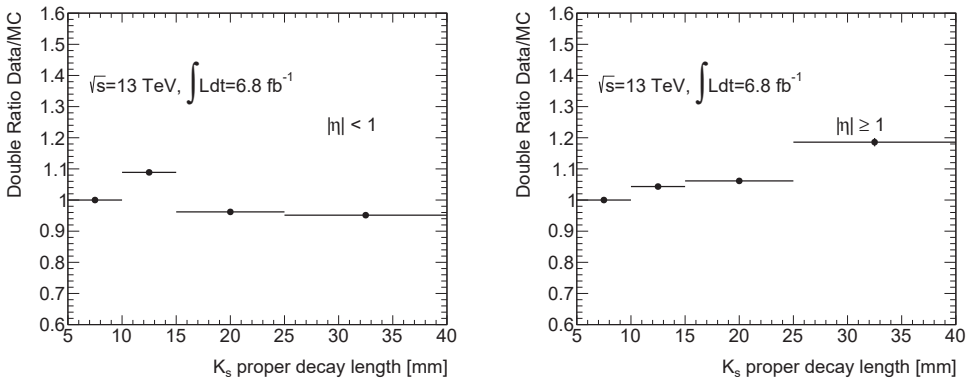

(a) (b)

Figure 6.3: Double ratio of number of K_S^0 found in MC and data individually normalised to the number found at the smallest interval, for the barrel region (left) and endcap (right). The maximum deviation from one is taken as an conservative estimate of the systematic uncertainty from the tracking efficiency.

deviation from one yielding 5% for $|\eta| < 1$ and 10% for $|\eta| \geq 1$. The signal MC samples are then re-reconstructed, using these values to randomly remove a fraction of tracks before the vertexing step. The analysis is repeated on these "Track-Killed" samples, and the difference between the "Nominal" and "Track-Killed" efficiency-vs-lifetime curves is taken as a systematic uncertainty. Figure 6.4 shows the track killing factor effect over the vertex reconstruction efficiency as a function of the radial position of the displaced vertex for a couple of signal samples. The effect of tracking systematic varies between 1-10% depending on different grid points.

6.3.2 ISR and FSR Modelling

Initial State Radiation (ISR) and Final State Radiation (FSR) have a direct effect on the signal efficiency. PYTHIA6 samples are used in this analysis in order to use the specific package for modelling interaction of R-hadron. However, it is known that PYTHIA6 has a problem in terms of modelling of ISR and FSR. As MG5_aMCNLO simulate a more accurate description of radiative effects, our PYTHIA6 samples are re-weighted to reproduce the distribution of $p_{\mathrm{T}}(\tilde{g}\tilde{g})$ from equivalent MG5_aMCNLO samples. The difference between the two generators is then used as a conservative estimate of the uncertainty on the modelling of the radiations. Several MG5_aMCNLO samples are compared to signal PYTHIA samples. To estimate the systematic uncertainties, the vector sum of the p_{T} of the gluino-gluino system in both the PYTHIA and the MG5_aMCNLO samples are compared as can be seen in the left plot of Fig. 6.5 for a gluino mass of 1400 GeV. This shows that PYTHIA predicts less radiation. The right figure shows a weight function extracted by taking the ratio of the left plot (done separately for all mass points). The event weights are then applied to the PYTHIA6 R-hadron signal MC events in the nominal processing. The effect of ISR/FSR systematic varies between different mass points and goes up to 30%. The efficiency for samples with smaller amount of $E_{\mathrm{T}}^{\mathrm{miss}}$ from the neutralino are more sensitive to the uncertainty on the ISR/FSR modelling.

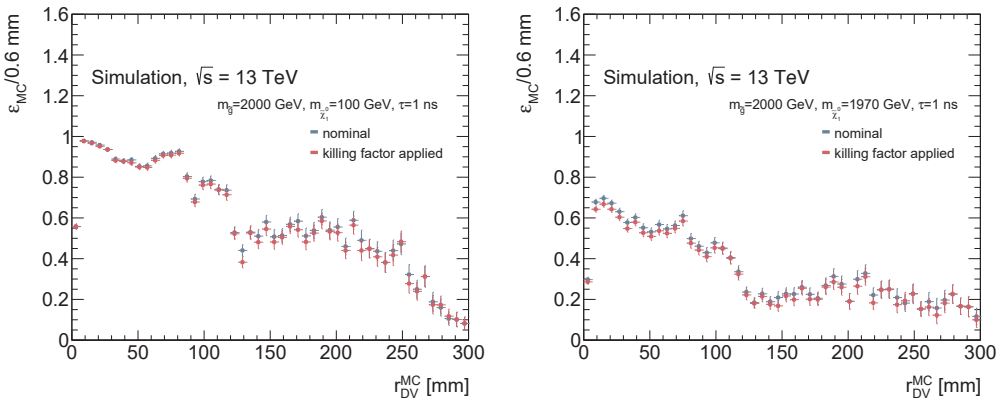

Figure 6.4: Vertex reconstruction efficiency for two MC signal samples, 402735 (left) and 402739 (right). The blue markers shows the efficiency distribution without the track-killing factor and the red markers are with the track-killing factor applied.

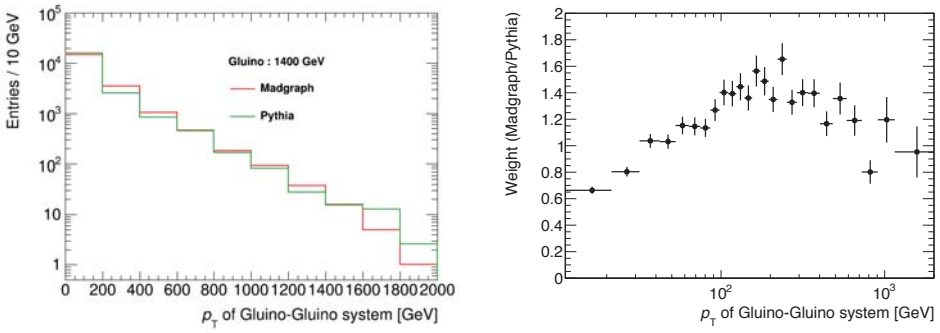

(a) (b)

Figure 6.5: (a) A vector summation of the transverse momentum for the gluino-gluino system with 1400 GeV R-hadron for samples of PYTHIA in green and a MG5_aMCNLO (MadGraph) in red. (b) A weight computed taking the ratio of the both samples.

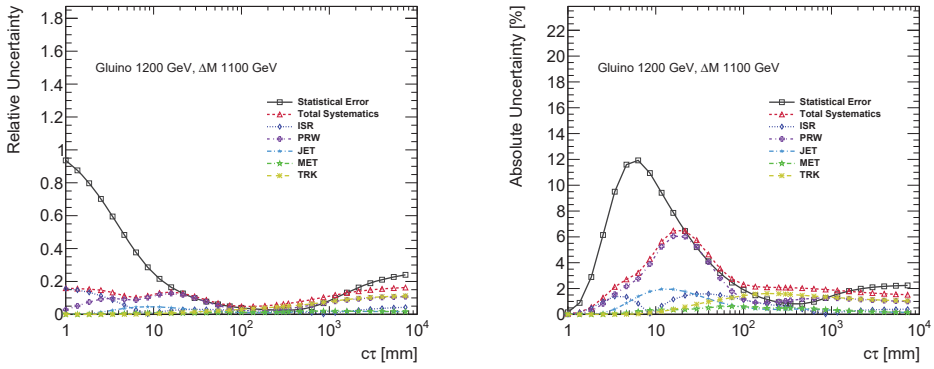

Figure 6.6: Contributions to the uncertainty on efficiency vs lifetime for a sample with 1200 GeV gluino and 100 GeV LSP. The left plots are the relative uncertainties and the right plots are the absolute uncertainties.

6.3.3 Pileup Re-weighting

The standard ATLAS pileup re-weighting tool is used to weight the distribution of μ for MC samples to match that for data. The μ represents the average number of pp interactions per bunch crossing. In this procedure, the event weights are obtained from the distributions of the μ observed in data. It varies this $\pm 1\sigma$ around the mean value, $\langle\mu\rangle$, of the μ-distribution in order to obtain distributions for the up and down variations. The re-weighting procedure is applied using those distributions, taking the yield differences with respect to the nominal μ-distribution as systematic of the pileup re-weighting.

6.3.4 Summary of Uncertainties on the Signal Efficiency

Figure 6.6 shows the different contributions to the uncertainty on the efficiency-vs-$c\tau$. The dominant uncertainty at small lifetimes is statistical, as a result of our re-weighting procedure (only events with DVs decaying at small ct_{true} have significant contributions). Each simulated R-hadron signals sample has only 10k events. The breakdown of the different contributions to the uncertainty is summarised in Tab. 6.7.

Since many of the systematic uncertainties (such as that associated with changing the scale factor for the pileup re-weighting) are evaluated by looking at the difference between the "nominal" efficiency-vs-$c\tau$ and the efficiency-vs-$c\tau$ curve after some change (e.g. ISR weight variation), there is a statistical component to these systematic uncertainties, again, particularly at very small or very large lifetimes where individual events can have large weights.

In addition to the statistical uncertainty which dominates at small lifetimes, the ISR-related uncertainty is also large in some cases, as a larger boost arising from the recoil against an ISR jet can increase the fraction of events passing the jet or $E_{\mathrm{T}}^{\mathrm{miss}}$ cuts. At large lifetimes, the uncertainty associated with the lifetime re-weighting can also be seen in Fig. 6.6.

Figure 6.8 shows the efficiency-vs-proper-decay-length distribution for a certain R-hadron sample. All considered systematic uncertainties are included.

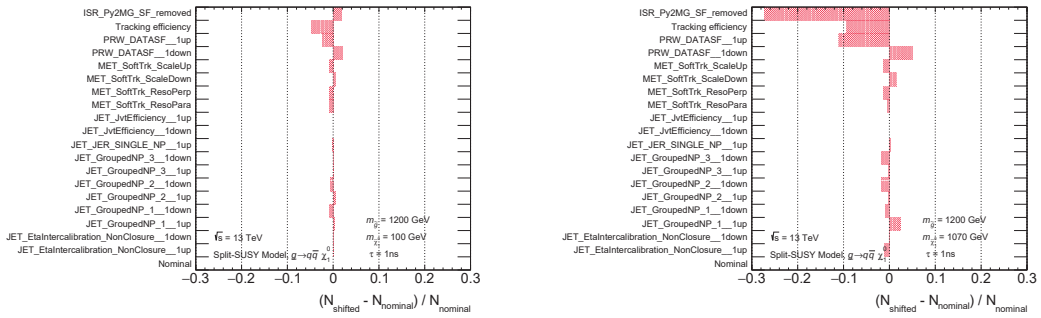

Figure 6.7: Pulls of the number of events passing the whole selections between nominal and shifted 1σ of each systematic source. The left plot is of a signal sample with gluino mass of 1200 GeV, the LSP mass of 100 GeV, R-hadron life time of 1 ns, while the right plot is of that with gluino mass of 1200 GeV, the LSP mass of 1070 GeV, R-hadron life time of 1 ns. Since the efficiency of a compressed scenario is significantly gained by ISR effect, the dominant uncertainty source is ISR weighting from Pythia to MadGraph.

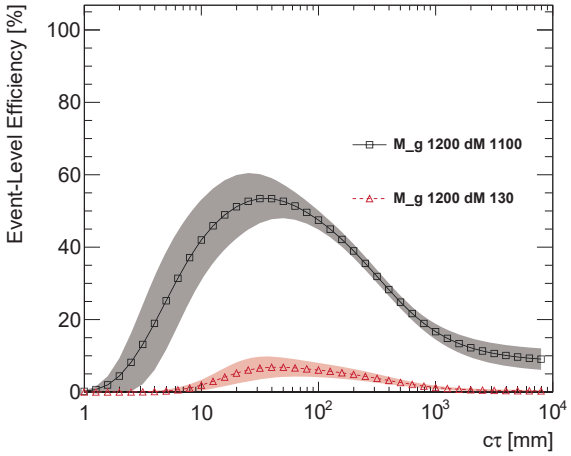

Figure 6.8: Efficiency vs proper decay length for the qq R-hadron samples with 1200 GeV gluino and 100 GeV or 1070 GeV neutralinos. All systematic corrections and uncertainties are included.

6.4 Exclusion Limits

Table 6.1 shows the number of events in data remaining after each of the selection cuts. No events containing a massive displaced vertex with high track multiplicity have been

Table 6.1: Cut flow table for 2016 data.

Event Selection Cuts			
	Number of Events	Relative Efficiency [%]	Overall Efficiency [%]
Initial Events	75439504	100	100
Good Runs List	73374312	97.3	97.3
Event cleaning	73019704	99.5	96.8
Primary vertex	73018496	100.0	96.8
NCB veto	47801448	65.5	63.4
MET Trigger	28580256	59.8	37.9
MET Filter	2855625	10.0	3.8
Offline MET cut	294614	10.3	0.39
Base DV selection	45734	15.5	$6.1{\cdot}10^{-2}$
Full DV selection	0	0.0	0.0
Vertex Selection Cuts			
	Number of DVs	Relative Efficiency [%]	Overall Efficiency [%]
Reco DVs	41243944	100	100
Event cuts	154140	0.37	0.37
Fiducial acceptance	130087	84.4	0.32
DV displacement	129886	99.8	0.31
Fit quality	128491	98.9	0.31
Material veto	53621	41.7	0.13
Disabled module	51876	96.7	0.13
DV nTrk	6	$1.2{\cdot}10^{-2}$	$1.5{\cdot}10^{-5}$
DV mass	0	0.0	0.0

observed in the ATLAS dataset recoded in 2016 at $\sqrt{s} = 13$ TeV corresponding to the integral luminosity of 32.7 fb^{-1}. The estimated number of background DVs is 0.02 ± 0.02 as shown in Section 5.8.1. The results are interpreted in the context of the Split-SUSY models (see Section 2.2.3). Given the values discussed so far, upper limits are set for the production cross section σ_{prod} of a pair of gluinos which form R-hadrons and decay into two quarks each. The mean expected number of events passing the selections N is formulated as:

$$N = L \cdot \sigma_{\text{prod}} \cdot \epsilon(c\tau), \tag{6.3}$$

where , L is the integrated luminosity, ϵ is the event selection acceptance. The integrated luminosity used in this analysis is corresponding to 32.7 fb^{-1}. Its relative uncertainty is 3.4%. It is derived from a preliminary calibration of the luminosity scale using x–y beam-separation scans [121] performed in May 2016.

Figure 6.9 shows upper limits on the cross section for the decay, $\tilde{g} \to q\bar{q}\tilde{\chi}_1^0$, for several $m_{\tilde{g}}$ values as a function of $c\tau$. The left figure has a fixed value for $m_{\tilde{\chi}_1^0} = 100$ GeV while the right figure has a fixed $\Delta m = m_{\tilde{g}} - m_{\tilde{\chi}_1^0} = 100$ GeV. The horizontal grey dashed lines in the plot represent the theoretically given cross section for the gluino pair production, $pp \to \tilde{g}\tilde{g}$, with squarks decoupled. The mass of squarks are assumed to be 10 TeV here. The grey bands represent the uncertainties of the cross sections. Parameter space surrounded by the grey line and the limit curve is excluded at 95% confidence level.

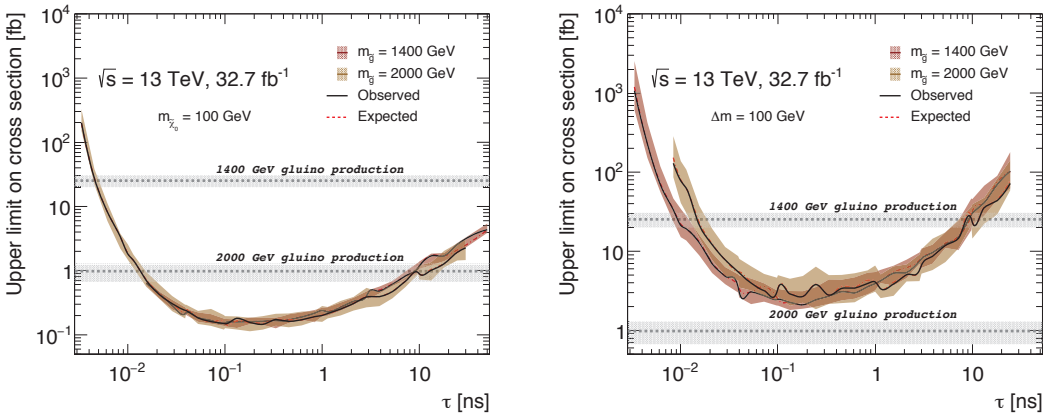

(a) (b)

Figure 6.9: Upper limit on cross-section vs decay length for the samples considered at fixed 100 GeV neutralino mass (a) and at fixed $\Delta m = 100$ GeV (b).

The maximum sensitivity is achieved around $c\tau = \mathcal{O}$(10-100) mm where the Pixel detector is placed. At the lower lifetime, long-lived particles likely to decay at the radius less than 4 mm from primary vertex. Such vertices are not selected by the vertex selection criteria as shown in Section 5.6.2. On the other hand, at the higher lifetime, long-lived particles likely to decay outside of the fiducial volume of $r < 300$ mm and $|z| < 300$ mm (see Section 5.6.1). Even if particles decay within the fiducial volume, the vertices might not be efficiently reconstructed due to relatively smaller tracking efficiency in a region outer than the outermost Pixel layer (Pixel Layer-2) placed around $r \approx 122.5$ mm. For the small Δm case (Fig. 6.9(b)), the $E_{\mathrm{T}}^{\mathrm{miss}}$ activity is also small, so that the event selection efficiency is not as high as large Δm scenario (Fig. 6.9(a)). These facts make the limit curves in Fig. 6.9 as they are.

The 2D exclusion contours in Fig. 6.10 and Fig. 6.11 interpret the results in the $m_{\tilde{g}}$-$c\tau$ and $m_{\tilde{g}}$-$m_{\tilde{\chi}^0}$ planes, respectively. For the large Δm scenario with the fixed neutralino mass of 100 GeV, the exclusion limit reaches $\sim$ 2400 GeV. A significant gain by $\sim$ 800 GeV is achieved with respect to the previous search [32]. In addition, it is the first time to set the exclusion limit for scenarios with smaller Δm between a gluino and the lightest neutralino in the ATLAS experiment. The limit is set around 1600 GeV at the maximum.

Figure 6.11 shows the 2D exclusion contour in a plane of $m_{\tilde{g}}$–$m_{\tilde{\chi}_1^0}$ with $\tau = 1$ ns. One can see that this analysis has sensitivity in a compressed region where $m_{\tilde{g}}$–$m_{\tilde{\chi}_1^0}$ is less than $\mathcal{O}$(100) GeV. It is difficult for typical SUSY search, such as multi-jets+$E_{\mathrm{T}}^{\mathrm{miss}}$ channel, to search this region due to lack of hard objects. It can be said that this analysis is complementary to the other SUSY searches.

Figure 6.12 shows constraints on the gluino mass-vs-lifetime plane for a Split-SUSY model with the gluino R-hadron decaying into light quarks and the lightest neutralino with mass of 100 GeV for several searches. There are the displaced vertices result, stopped gluino result, Pixel dE/dx result and jets+$E_{\mathrm{T}}^{\mathrm{miss}}$ result on the plot. It is shown that the displaced vertices search has better sensitivity than others when the gluino lifetime is approximately between 0.01 ns and 10 ns.

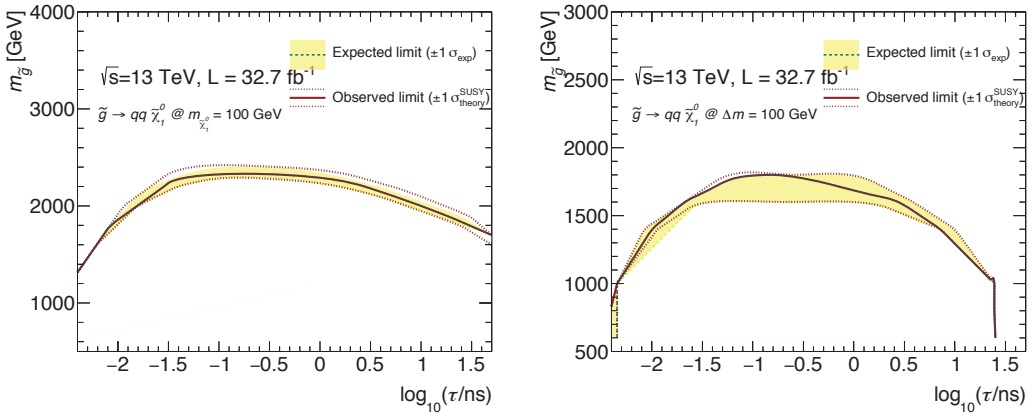

Figure 6.10: Excluded region in the gluino mass-vs-lifetime at fixed neutralino mass 100 GeV (left), and at fixed $\Delta m = 100$ GeV (right).

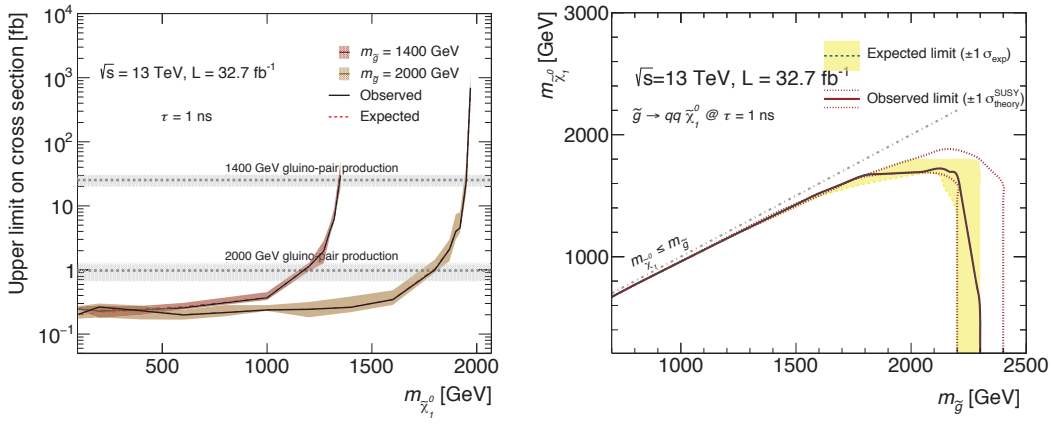

Figure 6.11: (Left) Upper limit on cross-section vs $m_{\tilde{\chi}^0_1}$ for the samples with $m_{\tilde{g}} = 1400$ or 2000 GeV. (Right) Excluded region in the gluino-vs-neutralino mass plane at fixed gluino lifetime $\tau = 1$ ns.

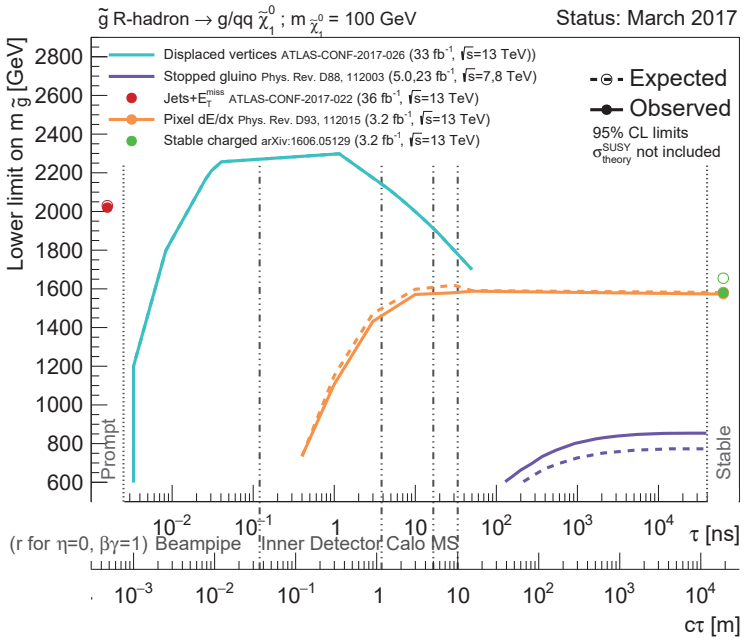

Figure 6.12: Constraints on the gluino mass-vs-lifetime plane for a Split-SUSY model with the gluino R-hadron decaying into light quarks and the lightest neutralino with mass of 100 GeV.

Chapter 7

Conclusion

The Standard Model of particle physics is generally regarded to be an incomplete theory because of several shortcomings such as absence of dark matter, instability of the Higgs potential or the fact that the strong force has not been unified with the electroweak interaction yet. A number of extensions of the Standard Model has been suggested to provide explanations to the unsolved problems. One of the most promising extensions of the Standard Model is the supersymmetry (SUSY). A large number of SUSY searches have been conducted typically using hard objects arising from a primary vertex as probes. However, such searches do not have adequate sensitivity to long-lived particles which decay at a distance from the interaction point.

Given the observed Higgs mass of ~ 125 GeV, the mass of squarks is naively expected to be much heavier than $\mathcal{O}(1)$ TeV that is basically beyond the reach of the LHC. A Split-SUSY model matches this situation and it often predicts a gluino, supersymmetric partner of gluon, to be long-lived. A long-lived gluino has colour charge so that it hadronizes and forms into R-hadron state. If the mass difference between a gluino and the lightest neutralino is as small as $\lesssim 100$ GeV, the gaugino co-annihilation mechanism would work to explain the observed relic density of dark matter as well.

In this dissertation, a search for direct production of long-lived gluino pairs which forms R-hadrons in final states with massive displaced vertices (DVs) with high track-multiplicity and missing transverse momentum was presented. Proton-proton collision data from the 2016 data taking period were analysed, corresponding to an integrated luminosity of 32.7 fb^{-1} collected at $\sqrt{s} = 13$ TeV by the ATLAS detector at the LHC. The following decay modes of the gluino was assumed to have 100% branching ratio:

$$\tilde{g} \to q\bar{q}\tilde{\chi}_1^0 \tag{7.1}$$

This analysis is aimed at scenarios with large mass-splitting between a gluino and neutralino as well as those with a smaller mass difference which have less acceptance because of non-energetic activities of visible particles.

Backgrounds arising from Standard Model particles are completely negligible when DVs are required to be massive and have high track-multiplicity. Some experimentally induced backgrounds, such as vertices from hadronic interaction, merged by vertexing algorithm and randomly crossed by a track, are dominant. The methods to estimate the merged vertices and random crossing tracks are based on those used in the analysis of the LHC run-1 data. A method to estimate the hadronic interaction and a way to validate the estimation of random crossing tracks were newly developed in this analysis. Furthermore, a new filter based on the calorimeter-level $E_{\mathrm{T}}^{\mathrm{miss}}$ was developed in order to improve the sensitivity to small mass difference scenarios.

The event counts observed after all event and vertex selections were found to be zero. This is compatible with the expected number of background events 0.02 ± 0.02. The results were, therefore, interpreted in terms of upper limits for different assumptions of gluino and neutralino masses and R-hadron lifetime. A large portion of parameter space has been excluded at 95% confidence level. The exclusion limit of gluino mass was set up to 2400 GeV. There is a significant gain compared to the previous Run1 limit which were set at 1600 GeV. In addition, a wide range of parameter space with a small mass difference between gluino and neutralino has been excluded up to ~ 1600 GeV. It is the first time for the ATLAS to set a limit on this compressed scenario. Since this search is almost background free, sensitivity to new physics is nearly proportional to statistics. Further improvement of sensitivity is expected as the data taking proceeds.

Appendix A

Hadronic interactions

Section 5.7.1 describes the method used to estimate the number of vertices produced by hadronic interactions which relies on the assumption that the low-mass component of the distribution (given a number of tracks in the vertex) follows an exponential function. This hypothesis is tested in this appendix by using an enriched region of hadronic interaction vertices and studying their mass distributions.

A.1 Hadronic interactions in material-dominated detector regions

An enriched hadronic interaction vertices is obtained by using the "Base" vertex selection but the material veto inverted. Figure A.1 shows the invariant mass distributions of the vertices reconstructed in that region; an exponential function has been fitted around 5 GeV, after the low mass peak. It can be observed that for the low track multiplicity there is a visible deviation from the exponential curves, which dilutes whenever the track multiplicity is increased. That contribution is supposed to come from the random crossing tracks.

The random crossing probability is highly correlated with the track density, i.e. the probability to attach a random track to a vertex increases whenever more tracks are present. Therefore, the random crossing tracks contribution in the tails of the distributions at Fig. A.1 can be checked by splitting the sample in high-track density events, i.e. high number of interactions per bunch crossing (μ); and low-track density events, i.e. low-μ. Figure A.2(a) shows several μ slices of 3-track DV mass distribution which passed the "Base" vertex selection but inverting material veto requirement.

The plot strongly supports that the high-tail mass distribution is produced by random crossing tracks vertices, given that the non-exponential components decrease as μ value decreases. Therefore, this sustains the factorization of the mass spectrum into a low mass peak which falls off exponentially, and a non-exponential tail from random crossing tracks vertices.

Figure A.2(b) shows that the fraction of the number of DVs with mass above 10 GeV for each μ slice in Fig. A.2(a). The x position of each point represents average μ of each slice. Fitting function is simple exponential function $\exp(p_0 + p_1 \cdot \mu)$. The fitting results are $p_0 = -8.95 \pm 0.81$ and $p_1 = 0.13 \pm 0.03$. The y-intercept is 1.3×10^{-4}. This means that, even if contribution from hadronic interaction does not perfectly follow exponential function, its non-exponential component should be $\mathcal{O}(10^{-4})$ of all DVs for 3-track DVs. Such component is consistent with zero in the statistical region of the nominal regions

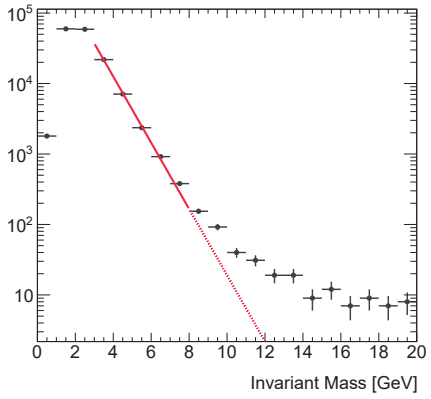

(a) 4-track DVs

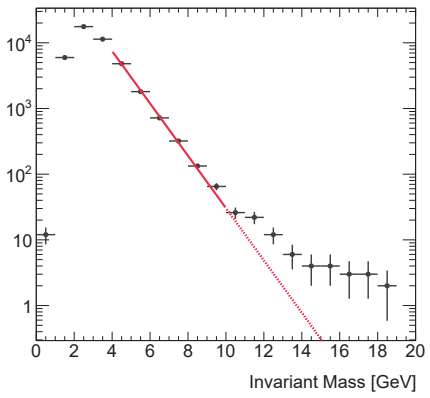

(b) 5-track DVs

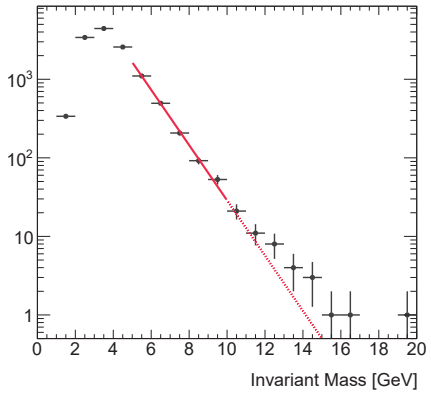

(c) 6-track DVs

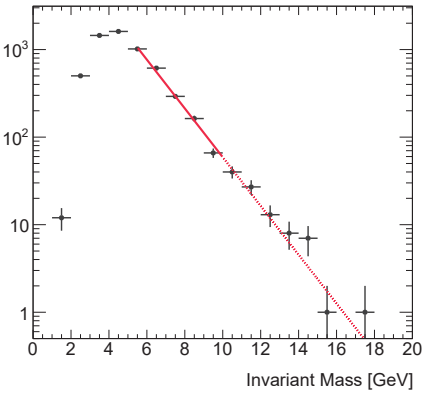

(d) ≥7-track DVs

Figure A.1: The invariant mass distributions of vertices with more than 3 tracks after "BASE" vertex selection but material veto is inverted. Red solid lines are fitted exponential functions and Red dashed lines are extrapolation of them.

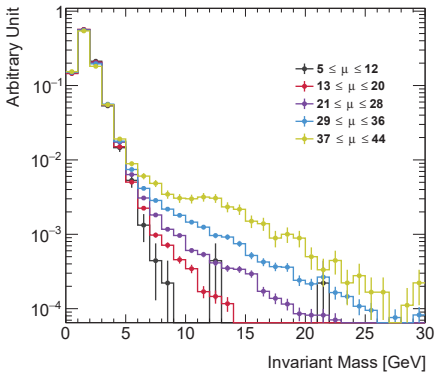

(a)

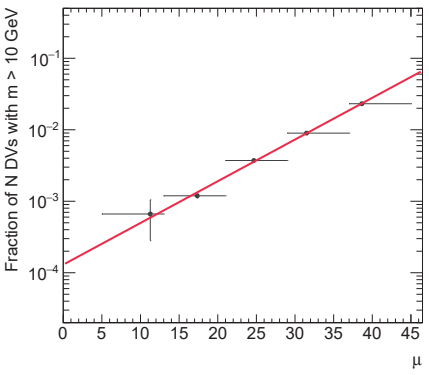

(b)

Figure A.2: (a) The μ slices of 3-track DV mass distribution of SUSY15 data samples in 2016. The DVs passed the base selection but inverting material veto requirement. Non-exponential components in the mass spectra decrease as μ value decreases. (b) Fraction of the number of DVs with mass above 10 GeV for each μ slice. The x position of each points represents average μ of each slice. Fitting function is simple exponential function $\exp(p_0 + p_1 \cdot \mu)$. The fitting results are $p_0 = -8.95 \pm 0.81$ and $p_1 = 0.13 \pm 0.03$.

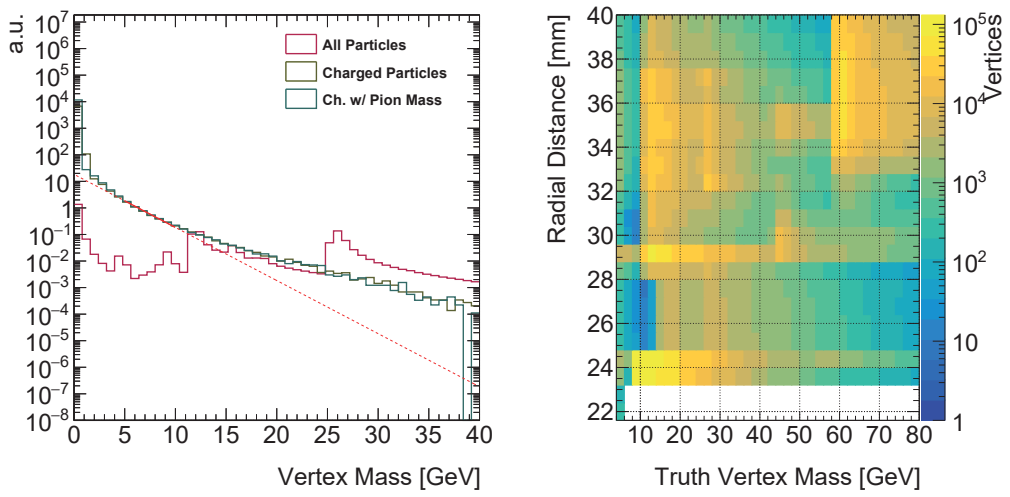

(a) (b)

Figure A.3: The truth vertex masses are shown in (a) for various selections placed on the outgoing particles from GEANT4-simulated interactions. The vertex mass as a function of radial distance from the interaction point is shown in (b) showing the materials that make up the various layers of material close to the interaction point.

(where material veto requirement is not inverted).

A.2 Geant4 studies

A study was performed using PYTHIA8 dijet MC sample. Truth vertices which were created by interactions simulated in GEANT4 were selected. For these interactions, a vertex mass is calculated in several ways.

1. Using all outgoing truth particles from the truth vertex
2. Using only final-state charged particles with p_{T} above 1 GeV
3. Using only final-state charged particles with p_{T} above 1 GeV using an assumption of the charged pion mass to simulate the reco-level vertex reconstruction

A plot of these definitions inclusive in vertex particle multiplicity can be found in Fig. A.3(a), normalised to the integral above 10 GeV. The shape of the fully inclusive distribution is indicative of the complex nature of the GEANT4 simulation attempting to describe the interactions with heavy elements in the detector material. This inclusive distribution as a function of mass and radial distance shows clearly in Figure A.3(b) that there are features as expected. The largely Be-9 beam pipe at 25 mm is clearly visible, as is the C-12 structures in the IBL support and IBL modules. A clear contribution is seen at the IBL radius of Si-28 interactions.

When using only final-state charged particles with p_{T} above 1 GeV with an assumed charged pion mass, reconstructable truth-level vertices can be built. These vertices are then binned in particle multiplicity (using the above definition). The distributions of the masses of these vertices are then fit to an exponential distribution in the region of

5-10 GeV. This fit is then extrapolated into the region above 10 GeV in vertex mass. The disagreement between the integral of the fit function above 10 GeV and that of the truth distribution is seen to be $\sim 300\%$. Distributions and fits can be seen in Fig. A.4.

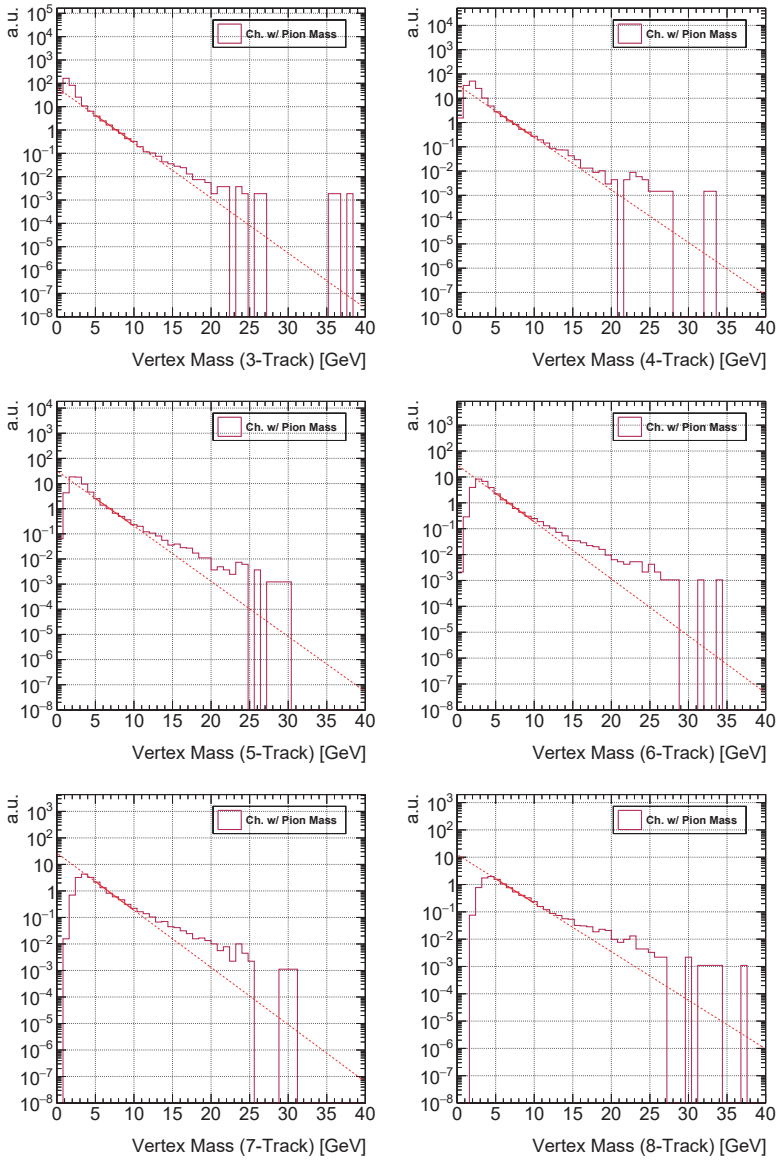

Figure A.4: The distributions of reconstructable mass for truth-level vertices is shown binned in the number of reconstructable charged particles. The region between 5-10 GeV is fit to an exponential for comparison in the region above 10 GeV to the truth distribution.

Bibliography

[1] S. L. Glashow. Partial-symmetries of weak interactions. *Nucl. Phys.*, 22(4):579–588, **1961**.

[2] S. Weinberg. A Model of Leptons. *Phys. Rev. Lett.*, 19(21):1264–1266, **1967**.

[3] A. Salam. Weak and Electromagnetic Interactions. *Conf. Proc.*, C680519:367–377, **1968**.

[4] S. L. Glashow, J. Iliopoulos, L. Maiani. Weak Interactions with Lepton-Hadron Symmetry. *Phys. Rev. D*, 2(7):1285–1292, **1970**.

[5] ATLAS Collaboration. The ATLAS Experiment at the CERN Large Hadron Collider. *JINST*, 3:S08003, **2008**.

[6] L. Evans, P. Bryant. LHC Machine. *JINST*, 3(08):S08001–S08001, **2008**.

[7] ATLAS Collaboration. Observation of a new particle in the search for the Standard Model Higgs boson with the ATLAS detector at the LHC. *Phys. Lett. B*, 716:1, **2012**, 1207.7214.

[8] CMS Collaboration. Observation of a new boson at a mass of 125 GeV with the CMS experiment at the LHC. *Phys. Lett. B*, 716:30, **2012**, 1207.7235.

[9] J. Tauber *et al.* The Scientific programme of Planck. **2006**, arXiv:astro-ph/0604069.

[10] Planck Collaboration. Planck 2015 results - xiii. cosmological parameters. *A&A*, 594:A13, **2016**.

[11] Y. Fukuda et al. Evidence for oscillation of atmospheric neutrinos. *Phys. Rev. Lett.*, 81:1562–1567, **1998**, arXiv:hep-ex/9807003.

[12] H. Miyazawa. Baryon number changing currents*. *PTP*, 36(6):1266, **1966**.

[13] P. Ramond. Dual theory for free fermions. *Phys. Rev. D*, 3:2415–2418, **1971**.

[14] Yu. A. Golfand, E. P. Likhtman. Extension of the Algebra of Poincare Group Generators and Violation of p Invariance. *JETP Lett.*, 13:323–326, **1971**. [Pisma Zh. Eksp. Teor. Fiz.13,452(1971)].

[15] A. Neveu, J. Schwarz. Factorizable dual model of pions. *Nucl. Phys. B*, 31(1):86 – 112, **1971**.

[16] A. Neveu, J. H. Schwarz. Quark model of dual pions. *Phys. Rev. D*, 4:1109–1111, **1971**.

[17] J.-L. Gervais, B. Sakita. Field theory interpretation of supergauges in dual models. *Nucl. Phys. B*, 34(2):632 – 639, **1971**.

[18] D. Volkov, V. Akulov. Is the neutrino a goldstone particle? *Phys. Lett. B*, 46(1):109 – 110, **1973**.

[19] J. Wess, B. Zumino. A lagrangian model invariant under supergauge transformations. *Phys. Lett. B*, 49(1):52 – 54, **1974**.

[20] J. Wess, B. Zumino. Supergauge transformations in four dimensions. *Nucl. Phys. B*, 70(1):39 – 50, **1974**.

[21] Y. Gershtein et al. Working Group Report: New Particles, Forces, and Dimensions. In *Proceedings, Community Summer Study 2013: Snowmass on the Mississippi (CSS2013): Minneapolis, MN, USA, July 29-August 6, 2013*, **2013**, arXiv:1311.0299.

[22] N. Sakai. Naturalnes in supersymmetric guts. *Zeitschrift für Physik C Particles and Fields*, 11(2):153–157, **1981**.

[23] ATLAS and CMS Collaborations. Combined Measurement of the Higgs Boson Mass in *pp* Collisions at $\sqrt{s} = 7$ and 8 TeV with the ATLAS and CMS Experiments. *Phys. Rev. Lett.*, 114:191803, **2015**, 1503.07589.

[24] A. Arvanitaki *et al.* Mini-split. *JHEP*, 2013(2):126, **2013**.

[25] F. Gabbiani *et al.* A Complete analysis of FCNC and CP constraints in general SUSY extensions of the standard model. *Nucl. Phys.*, B477:321–352, **1996**, arXiv:hep-ph/9604387.

[26] T. Moroi, M. Nagai. Probing supersymmetric model with heavy sfermions using leptonic flavor and cp violations. *Phys. Lett. B*, 723(13):107 – 112, **2013**.

[27] M. Liu, P. Nath. Higgs boson mass, proton decay, naturalness, and constraints of the lhc and planck data. *Phys. Rev. D*, 87:095012, **2013**.

[28] M. Kawasaki *et al.* Big-Bang Nucleosynthesis and Gravitino. *Phys. Rev.*, D78:065011, **2008**, arXiv:0804.3745.

[29] J. D. Wells. Pev-scale supersymmetry. *Phys. Rev. D*, 71:015013, **2005**.

[30] D. Hooper. Particle Dark Matter. In *Proceedings of Theoretical Advanced Study Institute in Elementary Particle Physics on The dawn of the LHC era TASI 2008: Boulder, USA, June 2-27, 2008*, pages 709–764, **2010**, arXiv:0901.4090.

[31] M. Fairbairn *et al.* Stable massive particles at colliders. *Phys. Rep.*, 438(1):1–63, **2007**.

[32] ATLAS Collaboration. Search for massive, long-lived particles using multitrack displaced vertices or displaced lepton pairs in *pp* collisions at $\sqrt{s} = 8$ TeV with the ATLAS detector. *Phys. Rev. D*, 92:072004, **2015**, 1504.05162.

[33] ATLAS Collaboration. Insertable b-layer technical design report. (September), **2010**.

[34] A. Purcell. Go on a particle quest at the first CERN webfest. Le premier webfest du CERN se lance la conqute des particules. (BUL-NA-2012-269. 35/2012):10, **2012**.

[35] ATLAS Collaboration. Summary plots from the atlas standard model physics group, 2016.

[36] S. P. Martin. A supersymmetry primer. **1997**, arXiv:hep-ph/9709356.

[37] R. Haag, J. T. opuszaski, M. Sohnius. All possible generators of supersymmetries of the s-matrix. *Nucl. Phys. B*, 88(2):257 – 274, **1975**.

[38] G. R. Farrar, P. Fayet. Phenomenology of the production, decay, and detection of new hadronic states associated with supersymmetry. *Phys. Lett. B*, 76(5):575 – 579, **1978**.

[39] A. Borriello, P. Salucci. The dark matter distribution in disc galaxies. *MNRAS*, 323(2):285, **2001**.

[40] H. Hoekstra, H. Yee, M. D. Gladders. Current status of weak gravitational lensing. *New Astron. Rev.*, 46(12):767 – 781, **2002**. An Alternative to Dark Matter: MOND.

[41] D. Clowe *et al.* A direct empirical proof of the existence of dark matter. *Astrophys. J.*, 648:L109–L113, **2006**, arXiv:astro-ph/0608407.

[42] G. Jungman, M. Kamionkowski, K. Griest. Supersymmetric dark matter. *Phys. Rep.*, 267(5):195 – 373, **1996**.

[43] K. Harigaya, K. Kaneta, S. Matsumoto. Gaugino coannihilations. *Phys. Rev. D*, 89(11):115021, **2014**.

[44] N. Nagata, H. Otono, S. Shirai. Probing binogluino coannihilation at the LHC. **2015**.

[45] C. De Melis. The CERN accelerator complex. Complexe des acclrateurs du CERN. **2016**. General Photo.

[46] S. Baird. Accelerators for pedestrians; rev. version. Technical Report AB-Note-2007-014. CERN-AB-Note-2007-014. PS-OP-Note-95-17-Rev-2. CERN-PS-OP-Note-95-17-Rev-2, CERN, Geneva, **2007**.

[47] ATLAS Collaboration. Luminosity Public Results Run2.

[48] J. Pequenao. Computer generated image of the whole ATLAS detector. **2008**.

[49] ATLAS Collaboration. Studies of the ATLAS Inner Detector material using $\sqrt{s} =$ 13 TeV *pp* collision data. ATL-PHYS-PUB-2015-050, 2015.

[50] J. Pequenao. Computer generated image of the ATLAS inner detector. **2008**.

[51] M. Capeans *et al.* ATLAS Insertable B-Layer Technical Design Report. Technical Report CERN-LHCC-2010-013. ATLAS-TDR-19, **2010**.

[52] ATLAS Collaboration. ATLAS Insertable B-Layer Technical Design Report Addendum. Technical Report CERN-LHCC-2012-009. ATLAS-TDR-19-ADD-1, **2012**. Addendum to CERN-LHCC-2010-013, ATLAS-TDR-019.

[53] V. Zivkovic et al. The FE-I4 pixel readout system-on-chip resubmission for the insertable B-Layer project. *JINST*, 7:C02050, **2012**.

[54] G. Darbo. Experience on 3D Silicon Sensors for ATLAS IBL. Technical Report arXiv:1411.6937. ATL-INDET-PROC-2014-017, CERN, Geneva, **2014**. Comments: 9 pages, 7 figures, conference proceedings for International Workshop on Semiconductor Pixel Detectors for Particles and Imaging (PIXEL2014), will be published on JINST.

[55] I. Perić *et al.* The fei3 readout chip for the atlas pixel detector. *NIM-A*, 565(1):178 – 187, **2006**. Proceedings of the International Workshop on Semiconductor Pixel Detectors for Particles and Imaging, PIXEL 2005.

[56] J. Pequenao. Computer generated images of the Pixel, part of the ATLAS inner detector. **2008**.

[57] H. Abreu. Performance of the electronic readout of the ATLAS liquid argon calorimeters. *JINST*, 5:P09003, **2010**.

[58] J. Saraiva, t. A. T. C. Group. Commissioning of the ATLAS Tile Calorimeter with Single Beam and First Collisions. *Nucl. Phys. B*, 215(1):107–109, **2011**.

[59] A. Collaboration. Readiness of the ATLAS Tile Calorimeter for LHC collisions. *EPJ C*, 70(4):1193–1236, **2010**.

[60] W. J. Stirling. Parton luminosity and cross section plots.

[61] P. Czodrowski. The ATLAS Trigger System: Ready for Run 2. Technical Report ATL-DAQ-PROC-2015-038, CERN, Geneva, **2015**.

[62] T. Cornelissen *et al.* The new atlas track reconstruction (newt). *JPCS*, 119(3):032014, **2008**.

[63] R. E. Kalman. A new approach to linear filtering and prediction problems. *J. Basic Eng.*, 82(1):35–45, **1960**.

[64] D. Wicke. A New algorithm for solving tracking ambiguities. *Proceedings, Physics and Experimentation at a Linear Electron-Positron Collider, 2nd ECFA/DESY Study*, pages 219–228, **1999**.

[65] R. O. Duda, P. E. Hart. Use of the hough transformation to detect lines and curves in pictures. *Commun. ACM*, 15(1):11–15, **1972**.

[66] M. Aaboud et al. A measurement of material in the ATLAS tracker using secondary hadronic interactions in 7 TeV pp collisions. *JINST*, 11(11):P11020, **2016**, arXiv:1609.04305.

[67] G. Piacquadio, K. Prokofiev, A. Wildauer. Primary vertex reconstruction in the ATLAS experiment at LHC. *J. Phys.: Conf. Ser.*, 119:032033, **2008**.

[68] ATLAS Collaboration. Performance of the ATLAS Inner Detector Track and Vertex Reconstruction in High Pile-Up LHC Environment. ATLAS-CONF-2012-042, 2012.

[69] ATLAS Collaboration. Vertex Reconstruction Performance of the ATLAS Detector at$\sqrt{s} = 13$ TeV. ATL-PHYS-PUB-2015-026, 2015.

[70] T. Robertson, J. D. Cryer. An iterative procedure for estimating the mode. *JASA*, 69(348):1012–1016, **1974**.

[71] R. Frhwirth, W. Waltenberger, P. Vanlaer. Adaptive Vertex Fitting. Technical Report CMS-NOTE-2007-008, CERN, Geneva, **2007**.

[72] V. Kostyukhin. VKalVrt - package for vertex reconstruction in ATLAS. Technical Report ATL-PHYS-2003-031, CERN, Geneva, **2003**. revised version number 1 submitted on 2003-09-24 11:10:53.

[73] S. R. Das. On a new approach for finding all the modified cut-sets in an incompatibility graph. *IEEE Transactions on Computers*, C-22(2):187–193, **1973**.

[74] ATLAS Collaboration. Electron and photon energy calibration with the ATLAS detector using LHC Run 1 data. *Eur. Phys. J.*, C74(10):3071, **2014**, arXiv:1407.5063.

[75] ATLAS Collaboration. Electron and photon energy calibration with the ATLAS detector using data collected in 2015 at $\sqrt{s} = 13$ TeV. ATL-PHYS-PUB-2016-015, 2016.

[76] ATLAS Collaboration. Muon reconstruction performance of the ATLAS detector in proton–proton collision data at $\sqrt{s} = 13$ TeV. *Eur. Phys. J. C*, 76:292, **2016**, 1603.05598.

[77] M. Cacciari, G. P. Salam, G. Soyez. The Anti-k(t) jet clustering algorithm. *JHEP*, 04:063, **2008**, arXiv:0802.1189.

[78] W. Lampl et al. Calorimeter Clustering Algorithms: Description and Performance. ATL-LARG-PUB-2008-002, 2008.

[79] ATLAS Collaboration. Jet Calibration and Systematic Uncertainties for Jets Reconstructed in the ATLAS Detector at $\sqrt{s} = 13$ TeV. ATL-PHYS-PUB-2015-015, 2015.

[80] ATLAS Collaboration. Electron performance measurements with the atlas detector using the 2010 lhc proton-proton collision data. *Eur. Phys. J. C*, 72(arXiv:1110.3174. CERN-PH-EP-2011-117):1909. 45 p, **2011**. Comments: 33 pages plus author list (45 pages total), 24 figures, 12 tables, submitted to Eur. Phys. J. C.

[81] ATLAS Collaboration. Search for displaced vertices arising from decays of new heavy particles in 7 TeV *pp* collisions at ATLAS. *Phys. Lett. B*, 707:478, **2012**, 1109.2242.

[82] H. K. Dreiner. An Introduction to explicit R-parity violation. **1997**, arXiv:hep-ph/9707435. [Adv. Ser. Direct. High Energy Phys.21,565(2010)].

[83] ATLAS Collaboration. Search for long-lived, heavy particles in final states with a muon and multi-track displaced vertex in proton–proton collisions at $\sqrt{s} = 7$ TeV with the ATLAS detector. *Phys. Lett. B*, 719:280, **2013**, 1210.7451.

[84] ATLAS Collaboration. Search for long-lived, heavy particles in final states with a muon and a multi-track displaced vertex in proton–proton collisions at $\sqrt{s} = 8$ TeV with the ATLAS detector. ATLAS-CONF-2013-092, 2013.

[85] N. E. Pettersson. *Search for long-lived supersymmetry particles by signature of a high track-multiplicity displaced vertex using the LHC-ATLAS Experiment.* PhD thesis, Tokyo Inst. Tech., **2015**.

[86] P. Meade, M. Reece, D. Shih. Long-Lived Neutralino NLSPs. *JHEP*, 1010, **2010**, arXiv:1006.4575.

[87] T. Sjostrand, S. Mrenna, P. Z. Skands. PYTHIA 6.4 Physics and Manual. *JHEP*, 05:026, **2006**, arXiv:hep-ph/0603175.

[88] ATLAS Collaboration. Further ATLAS tunes of Pythia 6 and Pythia 8. ATL-PHYS-PUB-2011-014, 2011.

[89] J. Pumplin *et al.* New generation of parton distributions with uncertainties from global QCD analysis. *JHEP*, 07:012, **2002**, arXiv:hep-ph/0201195.

[90] A. C. Kraan. Interactions of heavy stable hadronising particles. *EPJ C*, 37(1):91–104, **2004**.

[91] M. Kramer *et al.* Supersymmetry production cross sections in pp collisions at $\sqrt{s} = 7$ TeV. **2012**, arXiv:1206.2892.

[92] W. Beenakker *et al.* Squark and gluino production at hadron colliders. *Nucl. Phys. B*, 492(1):51 – 103, **1997**.

[93] A. Kulesza, L. Motyka. Threshold resummation for squark-antisquark and gluino-pair production at the lhc. *Phys. Rev. Lett.*, 102:111802, **2009**.

[94] A. Kulesza, L. Motyka. Soft gluon resummation for the production of gluino-gluino and squark-antisquark pairs at the lhc. *Phys. Rev. D*, 80:095004, **2009**.

[95] W. Beenakker *et al.* Soft-gluon resummation for squark and gluino hadroproduction. *JHEP*, 12:041, **2009**, arXiv:0909.4418.

[96] P. M. Nadolsky *et al.* Implications of CTEQ global analysis for collider observables. *Phys. Rev.*, D78:013004, **2008**, arXiv:0802.0007.

[97] A. D. Martin *et al.* Parton distributions for the LHC. *Eur. Phys. J.*, C63:189–285, **2009**, arXiv:0901.0002.

[98] ATLAS Collaboration. The atlas simulation infrastructure. *EPJ C*, 70(3):823–874, **2010**.

[99] S. Agostinelli *et al.* Geant4a simulation toolkit. *Nuclear Instruments and Methods in Physics Research Section A: Accelerators, Spectrometers, Detectors and Associated Equipment*, 506(3):250 – 303, **2003**.

[100] J. Allison *et al.* Geant4 developments and applications. *IEEE Transactions on Nuclear Science*, 53(1):270–278, **Feb 2006**.

[101] J. Allison *et al.* Recent developments in geant4. *Nuclear Instruments and Methods in Physics Research Section A: Accelerators, Spectrometers, Detectors and Associated Equipment*, 835:186 – 225, **2016**.

[102] R. Mackeprang, A. Rizzi. Interactions of coloured heavy stable particles in matter. *EPJ C*, 50(2):353–362, **2007**.

[103] J. Alwall *et al.* The automated computation of tree-level and next-to-leading order differential cross sections, and their matching to parton shower simulations. *JHEP*, 2014(7):79, **2014**.

[104] T. Sjöstrand, S. Mrenna, P. Skands. A brief introduction to pythia 8.1. *Comp. Phys. Comm.*, 178(11):852 – 867, **2008**.

[105] ATLAS Collaboration. ATLAS Pythia 8 tunes to 7 TeV data. ATL-PHYS-PUB-2014-021, 2014.

[106] R. D. Ball *et al.* Parton distributions with lhc data. *Nucl. Phys. B*, 867(2):244 – 289, **2013**.

[107] D. Casadei et al. The implementation of the ATLAS missing Et triggers for the initial LHC operation. **2011**.

[108] A. Strubig. The ATLAS transverse momentum trigger evolution at the LHC towards Run II. Technical Report ATL-DAQ-PROC-2015-031, CERN, Geneva, **2015**.

[109] P. J. Laycock *et al.* Derived Physics Data Production in ATLAS: Experience with Run 1 and Looking Ahead. *J. Phys. Conf. Ser.*, 513:032052, **2014**.

[110] T. Golling *et al.* The ATLAS Data Quality Defect Database System. *Eur. Phys. J.*, C72:1960, **2012**, arXiv:1110.6119.

[111] ATLAS Collaboration. Characterisation and mitigation of beam-induced backgrounds observed in the ATLAS detector during the 2011 proton-proton run. *JINST*, 8:P07004, **2013**, arXiv:1303.0223.

[112] ATLAS Collaboration. Non Collision Background Public Results.

[113] ATLAS Collaboration. Electron efficiency measurements with the ATLAS detector using the 2015 LHC proton–proton collision data. ATLAS-CONF-2016-024, 2016.

[114] ATLAS Collaboration. Photon identification in 2015 ATLAS data. ATL-PHYS-PUB-2016-014, 2016.

[115] ATLAS Collaboration. Muon reconstruction performance of the ATLAS detector in protonproton collision data at $\sqrt{s}$ =13 TeV. *Eur. Phys. J.*, C76(5):292, **2016**, arXiv:1603.05598.

[116] L. Moneta *et al.* The RooStats project. In *Proceedings of the 13th International Workshop on Advanced Computing and Analysis Techniques in Physics Research. February 22-27, 2010, Jaipur, India.*, page 57, **2010**, arXiv:1009.1003.

[117] G. Schott. RooStats for Searches. In *Proceedings, PHYSTAT 2011 Workshop on Statistical Issues Related to Discovery Claims in Search Experiments and Unfolding, CERN,Geneva, Switzerland 17-20 January 2011*, pages 199–208, Geneva, **2011**. CERN, arXiv:1203.1547.

[118] D. Boutigny et al. BaBar technical design report. In *BaBar Technical Design Report EPAC Meeting Stanford, California, March 17-18, 1995*, **1995**.

[119] N. Metropolis *et al.* Equation of state calculations by fast computing machines. *JCP*, 21(6):1087–1092, **1953**, http://dx.doi.org/10.1063/1.1699114.

[120] W. K. Hastings. Monte carlo sampling methods using markov chains and their applications. *Biometrika*, 57(1):97–109, **1970**.

[121] M. Aaboud et al. Luminosity determination in pp collisions at $\sqrt{s} = 8$ TeV using the ATLAS detector at the LHC. *Eur. Phys. J.*, C76(12):653, **2016**, arXiv:1608.03953.

List of Figures

List of Tables